NAVAL POSTGRADUATE SCHOOL

MONTEREY, CALIFORNIA

THESIS

STUDY OF THE POWER REQUIRED FOR FLIGHT OF THE AQUA-QUAD (SOLAR-POWERED QUAD-ROTOR UNMANNED AERIAL SYSTEM)

by

Sean Yang

September 2020

Thesis Advisor:	Kevin D. Jones
Co-Advisor:	Vladimir N. Dobrokhodov

Approved for public release. Distribution is unlimited.

THIS PAGE INTENTIONALLY LEFT BLANK

REPORT DOCUMENTATION PAGE				*Form Approved OMB No. 0704-0188*

1. AGENCY USE ONLY ***(Leave blank)***	**2. REPORT DATE** September 2020	**3. REPORT TYPE AND DATES COVERED** Master's thesis

4. TITLE AND SUBTITLE STUDY OF THE POWER REQUIRED FOR FLIGHT OF THE AQUA-QUAD (SOLAR-POWERED QUAD-ROTOR UNMANNED AERIAL SYSTEM)	**5. FUNDING NUMBERS**
6. AUTHOR(S) Sean Yang	
7. PERFORMING ORGANIZATION NAME(S) AND ADDRESS(ES) Naval Postgraduate School Monterey, CA 93943-5000	**8. PERFORMING ORGANIZATION REPORT NUMBER**
9. SPONSORING / MONITORING AGENCY NAME(S) AND ADDRESS(ES) N/A	**10. SPONSORING / MONITORING AGENCY REPORT NUMBER**
11. SUPPLEMENTARY NOTES The views expressed in this thesis are those of the author and do not reflect the official policy or position of the Department of Defense or the U.S. Government.	
12a. DISTRIBUTION / AVAILABILITY STATEMENT Approved for public release. Distribution is unlimited.	**12b. DISTRIBUTION CODE** A

13. ABSTRACT (maximum 200 words)

This thesis describes a study of the in-flight energy consumption of the Aqua-Quad—a Naval Postgraduate School–developed small Unmanned Aerial System (UAS). The Aqua-Quad concept pairs small drones and solar power in an innovative quadrotor system that can be launched from water or land for persistent and autonomous Intelligence, Surveillance, and Reconnaissance (ISR) operations.

The primary in-flight energy consumption of the Aqua-Quad stems from the thrust required to balance weight and drag. Analytically, this study used actuator disk theory to derive the power requirements based on the thrust and airspeeds during cruise and other phases of flight. To complete the power model, sub-models of the Aqua-Quad aerodynamics, particularly the lift induced by the solar arrays, were also developed. Experimental flights and Computational Fluid Dynamic analysis were conducted to validate these models.

The models developed in this thesis can be used to predict the power required for different Aqua-Quad flight speeds and weights, allowing the maximum flight range and endurance to be determined. An accurate power model also allows for a high-fidelity energy balance model to aid in mission planning and design optimization. Moreover, these models can be generalized for other small quadrotor UAS, which are expanding into the industrial, commercial, and military sectors for novel applications.

14. SUBJECT TERMS unmanned aerial system, aerodynamics, solar-powered, autonomous, hybrid air vehicle, VTOL, swarm	**15. NUMBER OF PAGES** 129
	16. PRICE CODE

17. SECURITY CLASSIFICATION OF REPORT	**18. SECURITY CLASSIFICATION OF THIS PAGE**	**19. SECURITY CLASSIFICATION OF ABSTRACT**	**20. LIMITATION OF ABSTRACT**
Unclassified	Unclassified	Unclassified	UU

NSN 7540-01-280-5500 Standard Form 298 (Rev. 2-89) Prescribed by ANSI Std. 239-18

THIS PAGE INTENTIONALLY LEFT BLANK

Approved for public release. Distribution is unlimited.

STUDY OF THE POWER REQUIRED FOR FLIGHT OF THE AQUA-QUAD (SOLAR-POWERED QUAD-ROTOR UNMANNED AERIAL SYSTEM)

Sean Yang
Lieutenant Colonel, Republic of Singapore Air Force
AE, United States Air Force Academy, 2005

Submitted in partial fulfillment of the
requirements for the degree of

**MASTER OF SCIENCE IN ENGINEERING SCIENCE
(MECHANICAL ENGINEERING)**

from the

**NAVAL POSTGRADUATE SCHOOL
September 2020**

Approved by: Kevin D. Jones
Advisor

Vladimir N. Dobrokhodov
Co-Advisor

Garth V. Hobson
Chair, Department of Mechanical and Aerospace Engineering

THIS PAGE INTENTIONALLY LEFT BLANK

ABSTRACT

This thesis describes a study of the in-flight energy consumption of the Aqua-Quad—a Naval Postgraduate School–developed small Unmanned Aerial System (UAS). The Aqua-Quad concept pairs small drones and solar power in an innovative quadrotor system that can be launched from water or land for persistent and autonomous Intelligence, Surveillance, and Reconnaissance (ISR) operations.

The primary in-flight energy consumption of the Aqua-Quad stems from the thrust required to balance weight and drag. Analytically, this study used actuator disk theory to derive the power requirements based on the thrust and airspeeds during cruise and other phases of flight. To complete the power model, sub-models of the Aqua-Quad aerodynamics, particularly the lift induced by the solar arrays, were also developed. Experimental flights and Computational Fluid Dynamic analysis were conducted to validate these models.

The models developed in this thesis can be used to predict the power required for different Aqua-Quad flight speeds and weights, allowing the maximum flight range and endurance to be determined. An accurate power model also allows for a high-fidelity energy balance model to aid in mission planning and design optimization. Moreover, these models can be generalized for other small quadrotor UAS, which are expanding into the industrial, commercial, and military sectors for novel applications.

THIS PAGE INTENTIONALLY LEFT BLANK

TABLE OF CONTENTS

LIST OF FIGURES

LIST OF TABLES

THIS PAGE INTENTIONALLY LEFT BLANK

LIST OF ACRONYMS AND ABBREVIATIONS

AGL	Above Ground Level
AOA	Angle of Attack
BLOS	Beyond Line of Sight
BMS	Battery Management System
CAD	Computer-Aided Design
C_D	Drag Coefficient
C_L	Lift Coefficient
CAVR	Center for Autonomous Vehicle Research
CFD	Computational Fluid Dynamics
cm	Centimeter
COTS	Commercial-Off-The-Shelf
DOD	Department of Defense
deg	Degree
ESC	Electronic Speed Controls
η	Efficiency Factor
g	Gram
GLONASS	Global Navigation Satellite System
GPS	Global Positioning System
in	Inch
ISR	Intelligence Surveillance and Reconnaissance
kg	Kilogram
LiIon	Lithium Ion
LiPo	Lithium-Polymer
LiS	Lithium-Sulphur
km	Kilometer
km/h	Kilometer per hour
kWh	Kilo Watt-Hour
m	Meter
mm	Millimeter
mph	Mile per hour

mps	Meters per second
NACA	National Advisory Committee for Aeronautics
NPS	Naval Postgraduate School
PID	Proportional–Integral–Derivative
PV	Photovoltaics
RPM	Revolutions Per Minute
SST	Shear Stress Transport
sUAS	Small Unmanned Aerial System
UAS	Unmanned Aerial System
UAV	Unmanned Aerial Vehicle
VRS	Vortex Ring State
VTOL	Vertical Takeoff and Landing
W	Watts

ACKNOWLEDGMENTS

I would like to thank my thesis advisors, Dr. Kevin Jones and Dr. Vladimir Dobrokhodov, for teaching and guiding me along this journey.

More broadly, I would like to thank the faculty and staff of the Mechanical and Aerospace Engineering department for helping me build the foundational skills and knowledge applied in this thesis.

Last and importantly, I thank my family for accompanying me and brightening my days.

THIS PAGE INTENTIONALLY LEFT BLANK

I. INTRODUCTION

The Aqua-Quad, shown in Figure 1 and Figure 2, is a solar-powered quadrotor that exploits the synergy between unmanned systems and renewable energy [1]. This innovative energy-autonomous vehicle concept circumvents the logistical challenge of refueling and recharging the vast numbers of systems needed for persistent swarm operations. One critical proof of concept for the Aqua-Quad is an energy balance study to determine the achievable solar power generation versus the power required for mission flight. While small quadrotors are increasingly popular air vehicles, existing literature lacks comprehensive models to fully describe their flight power requirements. By leveraging on prototype test flights and computer simulation, this report presents models for the quadrotor power requirements for various phases of flight: hovering, climb, descent, and cruise.

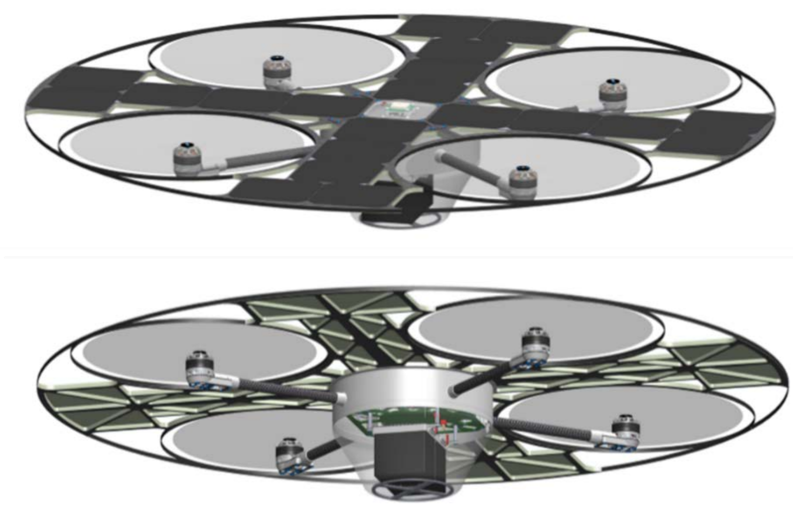

Figure 1. Aqua-Quad Quadrotor, Top and Bottom Views. Source: [1].

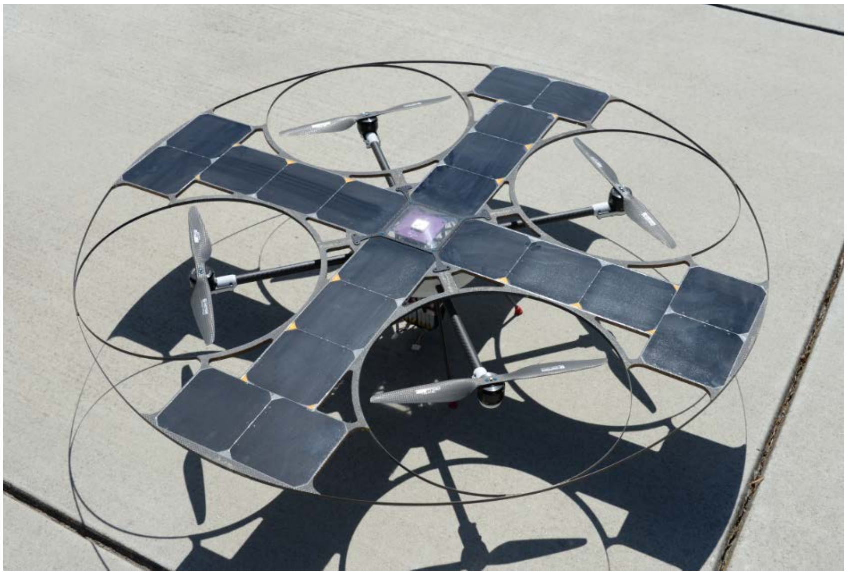

Figure 2. Aqua-Quad Quadrotor Prototype

A. GROWTH IN SMALL UNMANNED AERIAL SYSTEMS

Unmanned Aerial Systems (UAS), also commonly known as drones, range from large expensive Unmanned Aerial Vehicles (UAV), such as the U.S. Global Hawk, to toy nano-drones that can fit in the palm of your hand. While UAS are not new, the digital technology breakthroughs of the Smartphone era have triggered a new wave of smaller and more affordable vehicles, marked by the breakthrough of DJI drones in commercial markets. Since the early 2000s, drawing from the explosive growth in popularity of digital mobile devices, there have been significant improvements in a number of key enabling technologies such as (1) batteries and electric motors; (2) microprocessors and algorithms; (3) wireless communications; and (4) miniaturized sensors such as small digital cameras. As a result, the small UAS (sUAS) class has developed rapidly and can be cheaply acquired today. The sUAS class is expected to further develop with improvements in wireless communications systems (e.g., 5G), autonomous technologies (e.g., machine vision and AI), and batteries. With increasing capabilities, there is strong interest with commercial and industrial sectors in exploiting sUAS for business applications. One leading example is Amazon's Prime Air system that will use a Vertical Takeoff and Landing (VTOL) sUAS, shown in Figure 3, to fly up to 15 miles while carrying packages up to five pounds in weight [2].

Figure 3. Amazon’s Prime Air Drone. Source: [3].

Militaries have also been actively experimenting with sUAS. As shown in Figure 4, the U.S. Department of Defense (DOD) categorizes the sUAS as a Group 1 UAS and has outlined long-term sUAS development. Military applications include intelligence, surveillance, and reconnaissance missions, especially for persistent wide-area applications. Swarms of small UAS can offer greater survivability in contested environments compared to the current model of highly capable platforms that are large, few, and expensive. Moreover, the greater numbers allow one or a few members to be lost without completely compromising the overall strength of the swarm. The Aqua-Quad leverages on sUAS developments, carving out a niche as an energy-autonomous vehicle that permits long endurance missions with minimal supporting infrastructure.

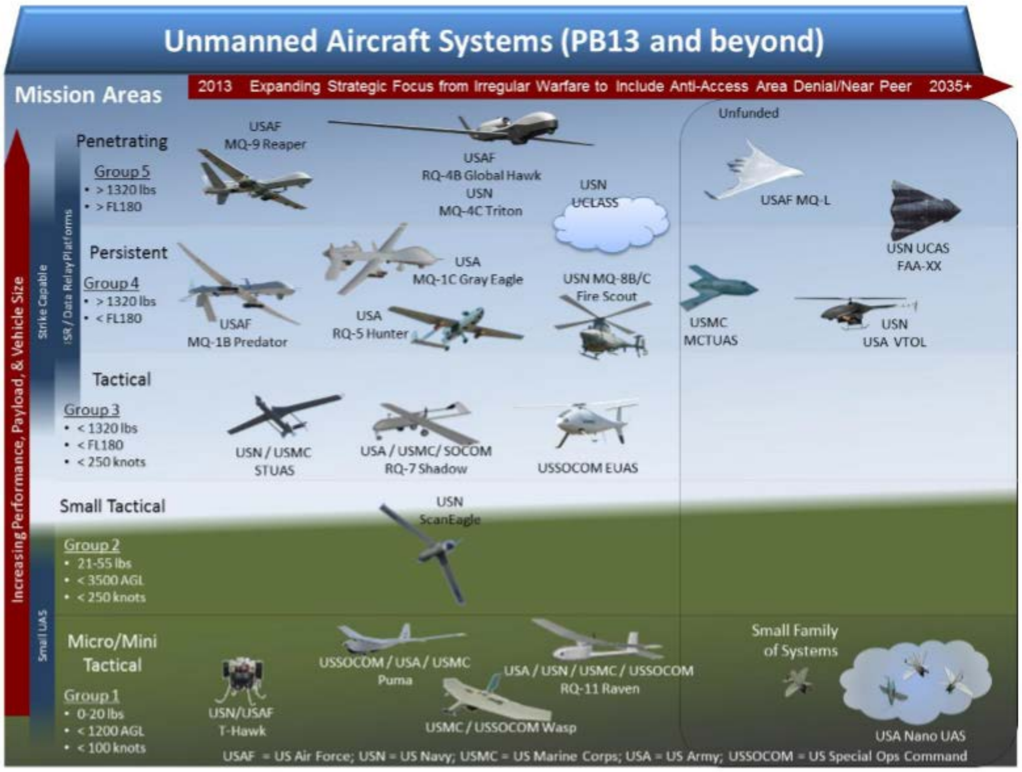

Figure 4. Growth in Unmanned Aerial Systems. Source: [4].

B. GROWTH IN BATTERY AND SOLAR TECHNOLOGY

The energy-autonomous concept of the Aqua-Quad depends heavily on battery and solar cell improvements made over the past 20 years. During this period, battery performance has improved greatly with the rapid growth in personal mobile devices and rise of the renewable energy sector. While consumer demand has driven the explosion in mobile digital devices, investment in the renewable energy sector has largely grown due to global concerns over climate change and sustainable energy sources. Besides supporting battery development, this renewable energy thrust has also led to improvements in solar power technology.

Lithium Polymer (LiPo) batteries are a significant improvement over traditional types of batteries. Nature News reports that “Modern Li-ion batteries hold more than twice as much energy by weight as the first commercial versions sold by Sony in 1991—and are ten times cheaper” [5]. The trends in the improvement of Li-ion batteries can also be seen in Figure 5. Today, besides being used in many consumer electronic devices, LiPo are the primary battery choice to power sUAS due to their balance of "high specific power, moderate specific energy, low cost, scalability, and high cycle life" [6]. For the future, LiPo batteries can be expected to incrementally improve but there is ongoing research and development in other battery technologies such as Lithium-Sulphur (LiS) batteries. Success in increasing the specific energy or power density of batteries would further enhance the performance and advantages of sUAS and the Aqua-Quad.

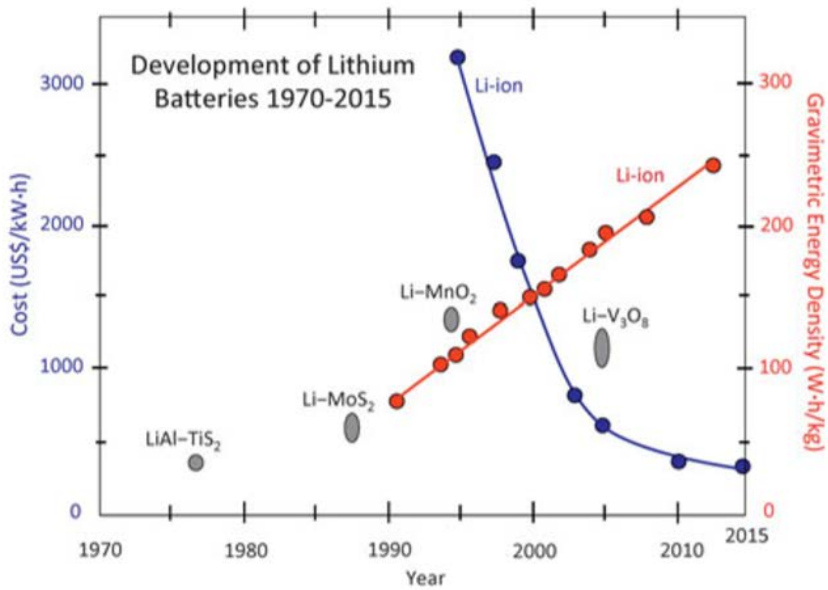

Figure 5. Lithium Ion Battery Improvements. Source: [7].

Solar power technology is driven by the appeal that the sun can provide up to 1 kW of power per square meter [8]. Hence, this would enable solar-powered vehicles to forgo the lengthy logistical chains required for refueling. The technological challenge has been to maximize the efficiency in converting this solar energy to usable electrical energy. Over the past 20 years, solar power technology has improved steadily in terms of cost and efficiency, becoming an increasingly viable energy source. In particular, referencing Figure 6, photovoltaic (PV) solar cell efficiency has improved from the 1970s to 2020s, with efficiencies reaching up to 47.1% for high-end solar cells [9]. For crystalline silicon cells, the dominant type, efficiencies have increased from 12 to 16% in the 1980s to 21 to 27%

in the 2020s [9]. In addition, PV solar cells have become more cost efficient. Referencing Figure 7, from the 1970s to the 2010s, the price of PV has fallen from over \$70/watt to \$1/watt. Besides PV cells, there are also alternative solar power systems being developed, such as printed solar cells, that may further reduce costs and enhance efficiencies [10].

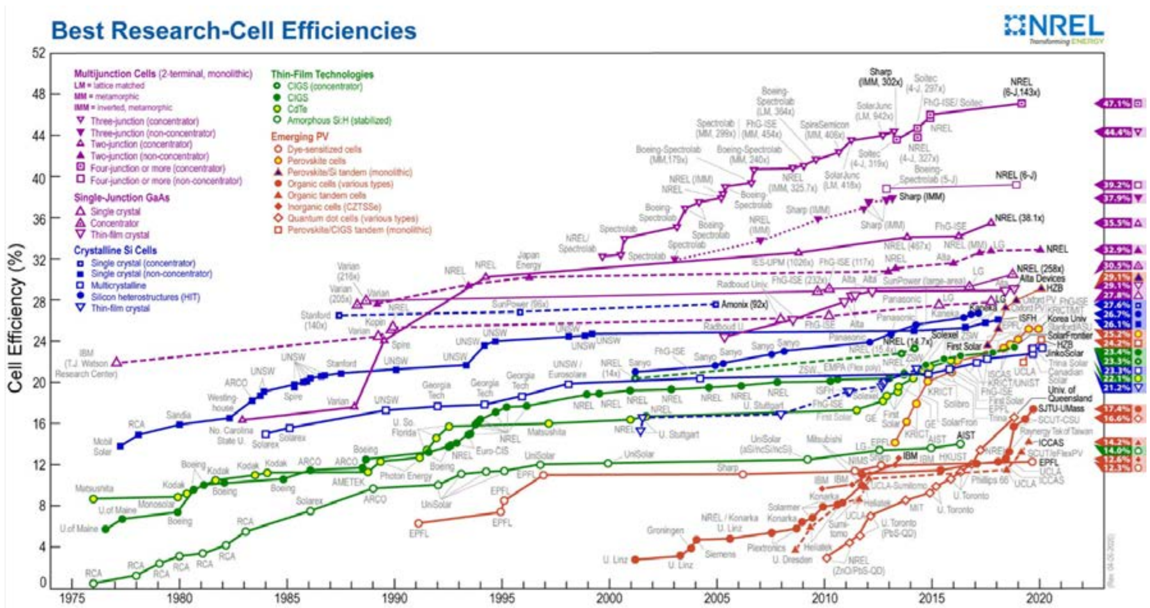

Figure 6. Improvements in Solar Cell Efficiency. Source: [9].

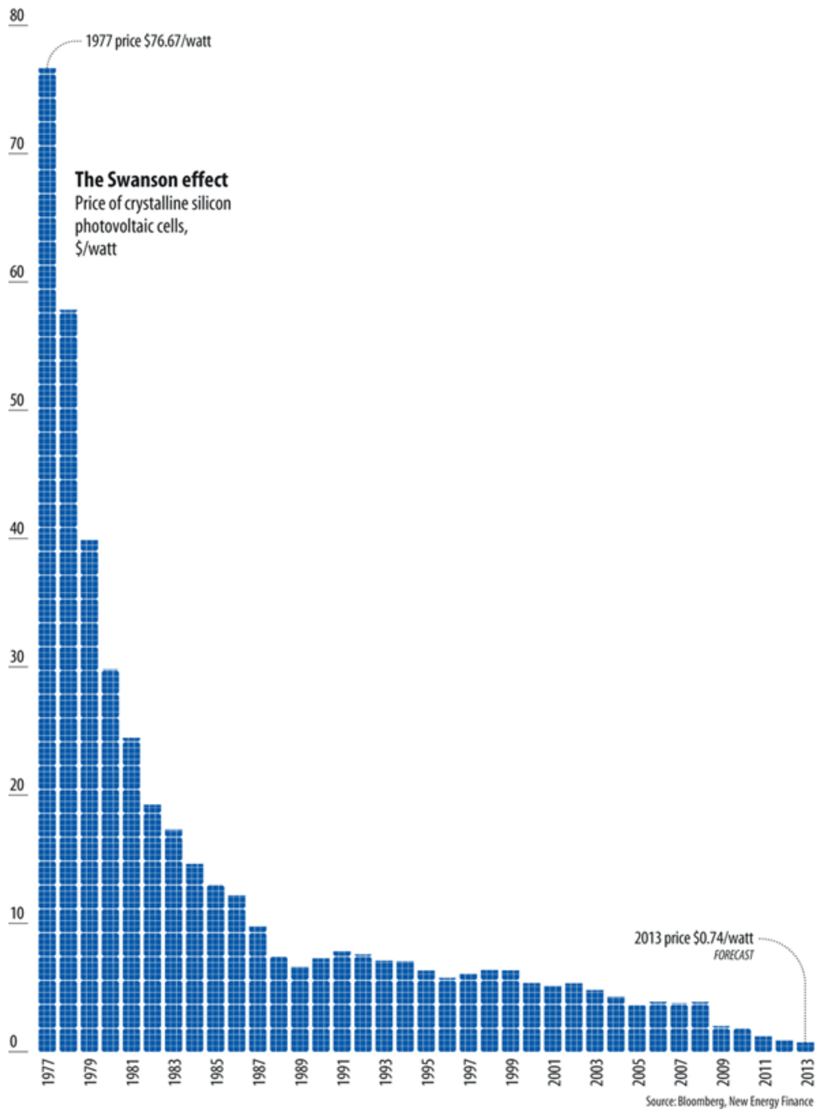

Figure 7. Drop in Price of Photovoltaic Cells. Source: [11].

C. LITERATURE ON QUADROTOR POWER

Quadrotors are still a relatively new phenomenon. It was only in the 2000s that improvements in microprocessors and microdevices enabled reliable and cost-effective flight controls for these vehicles. While small quadrotors have since broken into commercial markets, their use is largely limited to the hobbyist community. As a result, the literature on the power required for small quadrotor flight is not as established as it is for traditional fixed-wing aircraft and large helicopters. In addition, the current lack of large-scale industrial and business applications discourages the study of the power required for small quadrotor flight.

The business use cases for small quadrotor UAS remain constrained due to their limited range and endurance. While battery technology is one of the obvious constraints, operating range has been equally constrained by the technical and safety challenges of Beyond Line of Sight (BLOS) operations. A breakthrough in sUAS BLOS operations will depend on cost-effective Command and Control (C2) systems that can conduct complex and meaningful operations, while flying safely without collisions. The recent focus of sUAS development has been to surmount these technical challenges rather than optimize sUAS power management. Nevertheless, as technical improvements expand the quadrotor mission scope, there is growing interest in improving the power usage.

While interest in sUAS has led to several recent studies on quadrotor power, the existing body of work does not have a common model that can be easily applied across various quadrotors and to the Aqua-Quad. While most papers commonly start with the Rankine-Froude actuator disk theory, they develop differently to address the various phases of flight. Some papers, especially hobbyist articles, rapidly leave the theory behind to focus on empirical comparisons of Commercial-Off-The-Shelf (COTS) technology. In addition, many papers only use the actuator disk theory to determine hovering power requirements and then apply arbitrary scaling factors to determine the power requirements of other phases. Still other papers simply ignore phases of flight such as climbing and, especially, descending.

While textbooks on helicopter theory provide good theoretical analysis of power performance, they rely on assumptions for large traditional helicopters, which do not fully translate to small quadrotors. One major difference is that for control, traditional helicopters rely on large variable-pitch main rotors and tail rotors, while quadrotors rely on varying the rotation speeds of counter-rotating fixed-pitch propellers. These differences in operation result in many different aerodynamic features. For instance, the large variable-pitch main rotors allow for “auto-rotation”—a steep helicopter descent profile where the propeller acts as a windmill that extracts power from the airflow. The descent speed required to enter this state for small quadrotors with their small high-RPM rotors is excessive. In addition, the fixed-pitch quadrotor propellers behave differently in the windmill brake state. Equally significant, the quadrotor control efforts to maintain stability and a level attitude lead to increased power demands in descent.

The existing literature also lacks simple power models of small quadrotor UAS for cruise or horizontal flight. Many papers either go straight to empirical analysis or arbitrary scaled hovering power to account for cruise power demands. In addition, while some papers acknowledge a transition to 2-D airflow to analyze actuator disk theory, they do not elaborate on the dynamic between horizontal speed and drone pitch angles that influence the 2-D airflow. One final and glaring limitation of existing literature with regards to the Aqua-Quad is the absence of any model to describe the aerodynamics of a solar array or a wing fitted to a quadrotor.

In conclusion, the Aqua-Quad concept is an innovative addition to today's range of small unmanned air vehicles. To fully validate the concept of an energy-autonomous vehicle, an accurate energy-balance model needs to be developed. On the one hand, the ability to adequately generate and store solar energy needs to be researched. On the other hand, the power required to satisfy the mission flight profile also needs to be determined. Unfortunately, existing literature does not offer sufficient data to develop such an accurate energy-balance model; therefore, this thesis attempts to fill in the blanks through theoretical analysis, flight testing and Computational Fluid Dynamics (CFD).

THIS PAGE INTENTIONALLY LEFT BLANK

II. AQUA-QUAD CONCEPT AND DESIGN

The Aqua-Quad is envisioned to conduct extended-duration 24/7 Intelligence Surveillance and Reconnaissance (ISR) missions in land or maritime environments. When required, the Aqua-Quad can get airborne via its VTOL ability to communicate or to relocate rapidly to a new deployment site. The Aqua-Quad concept maximizes its potential by operating in a swarm of similar vehicles with homogenous or heterogeneous sensor payloads to cover large areas of interest. By offering longer endurance, lower signatures, simplified logistics, on-demand communication, and higher mobility, they can also provide higher operational effectiveness and efficiency than current systems, such as large UAVs or air-deployed sonobuoys.

A. OPERATIONAL CONCEPT AND MISSION PROFILE

The full vision is to employ a swarm of Aqua-Quads to carry out autonomous persistent wide-area sensing missions for the military, scientific, and private communities. Today, these ISR missions usually rely on large platforms equipped with capable but large sensor payloads. These platforms and their sub-systems tend to be costly and often need significant additions to enhance survivability in combat environments. To reverse the unsustainable trend of larger, more-complicated, costlier platforms, swarm robotics offers a solution to “disaggregate” operational capability among smaller simpler autonomous platforms. Individually, these autonomous vehicles are expendable and thus allow the overall system capability to degrade gracefully—whereby small losses do not lead to a drastic loss of capability.

The Aqua-Quad is an example of the swarm robot concept, focusing on surveillance operations in the maritime environment. For instance, equipped with an acoustic sensor, the Aqua-Quad can detect submarines for Anti-Submarine Warfare. Multiple platforms can accurately track submarines by triangulation or sharing time-delay-on-arrival (TDOA) information. By utilizing their air mobility, the fleet can adjust for ocean currents to keep on station, track moving targets, or relocate to new areas of operation. In this way, a fleet of vehicles can cover large areas for long periods of time. Moreover, through mesh networks and other modern networking technologies, a “flock” of Aqua-Quads could use collaborative behaviors for improved employment.

Besides using acoustic sensors to track submarines, the Aqua-Quad could carry other payloads such as electro-optics or electronic surveillance to conduct ISR for other target classes. For instance, mine detection systems could be used to detect mines at sea or on land. The Aqua-Quad could also be employed for non-military roles such as tracking marine wildlife, monitoring ocean currents for oceanography, or detecting pollution for disaster response. Besides these kinds of surveillance missions, a persistent autonomous network of Aqua-Quads could serve as communication nodes for tactical C2.

The Aqua-Quad was chosen to be a VTOL UAS to enable frequent and rapid repositioning. While fixed-wing aircraft require a runway or other specialized launch and recovery equipment, VTOL aircraft can take-off and land on a wider range of operating environments with greater autonomy. While VTOL aircraft tend to suffer trade-offs in range and mechanical complexity, this take-off and landing capability is a critical feature of their operating concept. In addition, the choice of a small quadrotor offsets the mechanical complexity associated with traditional VTOL platforms. Flight control for modern quadrotors is achieved by varying the Revolutions Per Minute (RPM) of each of the four counter-rotating fixed-pitch propellers. This simple system with few moving parts reduces costs and is suited for long-duration operations in austere environments.

For a nominal mission profile, the Aqua-Quad would deploy to an initial operating location. Once landed on station, it would either carry out its mission or stand by for future missions, while being charged by its solar power system. When required, it would take off and fly to a new deployment location. Based on the power model developed in this paper, the airspeed for best range is 7 m/s (25 km/h) at a power consumption rate of 670 W. This profile would give a range of over 6 km based on using a 178 Wh battery power source, as depicted in the envisioned flight profile in Figure 8.

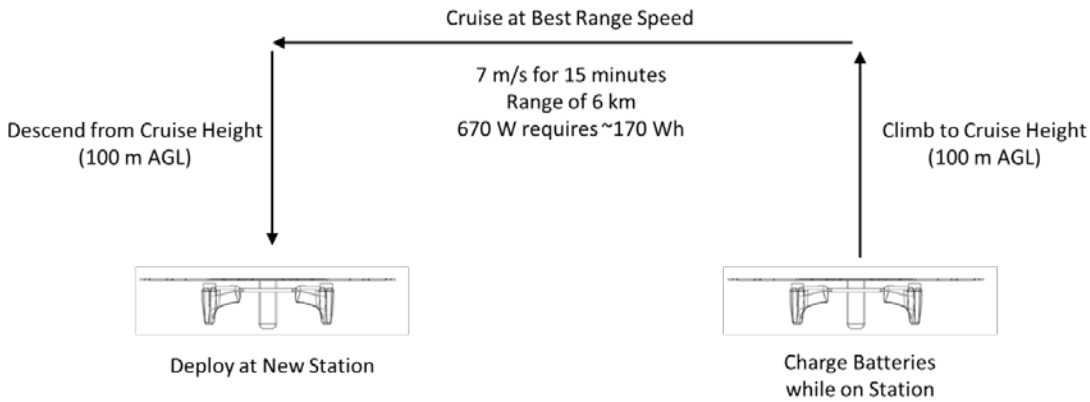

Figure 8. Aqua-Quad Flight Profile

B. FULL-SCALE PROTOTYPE DESCRIPTION

The Naval Postgraduate School (NPS) Aqua-Quad is an autonomous multi-rotor VTOL aircraft. It is designed with environmentally hardened electronics and a solar power system to operate in aquatic environments for periods of days and weeks. The current design mission is to carry an acoustic sensor to detect and track aquatic targets. The conceptual design is illustrated in Figure 9. A modular sensor payload, however, is envisaged to support a variety of ISR missions. The baseline prototype was designed at NPS over the past few years as detailed in [1].

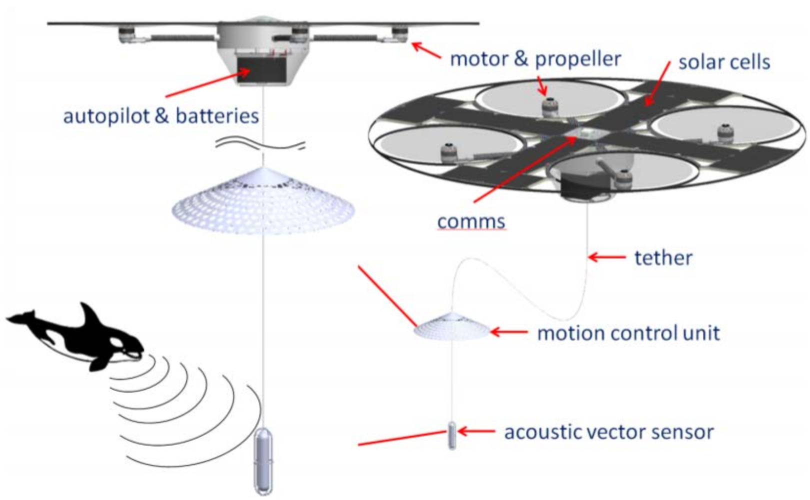

Figure 9. Aqua-Quad Conceptual Design. Source: [1].

1. Weight and Size

The mass of the prototype without any mission payload is about 3 kg. The design mission payload—an acoustic sensor—is estimated to be 300 to 500 g in mass. As a result, the maximum mass is about 3.6 kg, near the ideal hovering mass based on 60% of the maximum thrust available, giving the prototype sufficient overhead for maneuvering thrust.

2. Structure

The prototype uses a mixture of parts that include 3-D printed and COTS parts. The 3-D printed parts are made of plastic. The key considerations were weight, water permeability, and cost.

3. Battery

The prototype relies on COTS LiPo cells that can operate at drain rates of 3C with specific energies of ~170 Wh/kg. The prototype uses a 1 kg battery with 178 Wh capacity.

4. Propellers and Electric Motors

The Aqua-Quad prototype is designed to use propellers with a diameter of 356 or 381 mm (14 or 15 in). The motors considered to power the propellers were COTS, specifically the T-Motor 3510–13 700 Kv, the T-Motor U3 700 Kv, the KDE 3510XF 475 Kv, and the KDE 3510XF 715 Kv. The motors with higher Kv (the velocity rating of the motors and not kilovolts) are more compatible with the smaller 14-in propeller and would require a 3S battery. The 475 Kv motor is more compatible with the larger 15-in propeller and would require a 4S battery. The latter configuration is expected to perform more efficiently due to the larger disk area. Alternatively, the combination of the U3 motor and 14-in propeller is much lighter.

5. Flight Systems

The flight avionics of the prototype include the autopilot, Electronic Speed Controls (ESC), communications datalink, and payload computer. The autopilot is the open-source PixRacer and the ESCs are the Kiss 25A singles. Communication links are via a 3DR telemetry radio for short-range communications to GCS, a Spektrum-compatible satellite receiver for manual flight and a generic USB WiFi radio. Self-position is provided by a mRobotics GPS/compass module that is Global Positioning System (GPS) and Global Navigation Satellite System (GLONASS) compatible.

6. Mission Payload

The design mission of the Aqua-Quad prototype is to detect underwater targets with a towed acoustic sensor. While work on possible solutions is ongoing, the project experimented with the Acusonde Sensor as it fit the envisaged size and weight [12].

C. SCALE MODEL DESCRIPTION

To evaluate the aerodynamic characteristics of the Aqua-Quad, a smaller half-scale model was built to conduct extensive flight testing. A mock solar array was built that could be detached from the scale model. The scale model weighs 0.448 kg without a battery and without the mock solar array. With a LiPo battery, the prototype weighs 0.604 kg. The scale model uses Bolt 2207L 1660 KV motors paired with 7 in Gemfan propellers. For avionics, standard COTS parts were used for the GPS, ECS, and radio control.

THIS PAGE INTENTIONALLY LEFT BLANK

III. POWER FOR HOVERING FLIGHT

In this chapter, actuator disk theory is developed to determine the power requirements for the Aqua-Quad in hovering flight. While the primary Aqua-Quad operational concept does not involve long periods of hovering flight, analyzing this phase of flight lays a foundation for analyzing the other phases of flight. This chapter introduces the fundamental control volume analysis approach, which will then be applied to vertical flight and level cruise flight in subsequent chapters. In addition, this chapter introduces the efficiency losses of actual motors and propellers. This chapter lastly covers flight tests conducted to provide the empirical benchmarks.

A. THEORY

The Rankine-Froude actuator disk or momentum theory was developed over a hundred years ago to determine the power requirements for thrust-producing propellers. The theory assumes incompressible flow and approximates the propeller as an infinitely thin disk. The theory uses a control volume encompassing the airflow stream-tube that begins upstream at freestream pressure, passes through the actuator disk, and ends downstream back at freestream pressure. The control volume of interest is illustrated in Figure 10 with key parameters of pressure and velocity identified at the upstream Point 1, downstream Point 2, and at the disk.

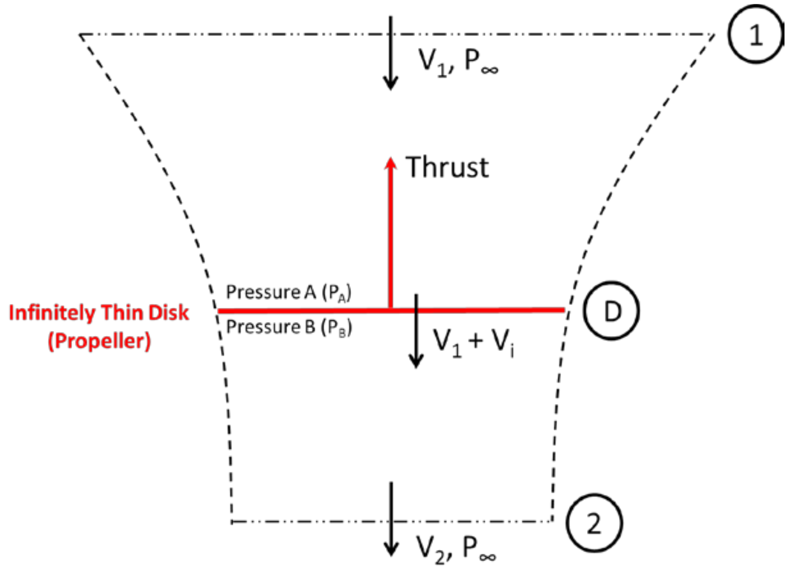

Figure 10. Control Volume for Actuator Disk Theory

Applying conservation of mass, the mass flow into the stream-tube at Point 1 is equal to the mass flow leaving the stream-tube at Point 2. In addition, this mass flow is also constant across the propeller or disk and can be written in terms of air density (ρ) and disk area (A_D). In other words:

$$\dot{m}_1 = \dot{m}_2 = \dot{m}_D = \rho AV \quad (1)$$

Applying the conservation of momentum for 1-D flow, the propeller thrust (T) increases the momentum of the airflow in the vertical direction in terms of the velocity of the airflow entering and exiting the stream-tube (v_1 and v_2, respectively).

$$T = \dot{m}\Delta v = \dot{m}(v_2 - v_1) \quad (2)$$

Thrust is also equivalent to the change in pressure (P_A to P_B) across the disk area (A_D) as follows:

$$T = (P_B - P_A)A_D \quad (3)$$

The pressure change across the disk can be rewritten in terms of the stream-tube velocities and freestream pressure (P_∞) by applying Bernoulli's equation to the streamlines from Point 1 to the disk and from the disk to Point 2, where ρ is the density of the airflow. Of note, the propeller accelerates the airflow from the initial freestream velocity (v_1) by an additional induced velocity (v_i) across the disk.

$$From\ Pt\ 1\ to\ disk: P_\infty + \frac{1}{2}\rho v_1^2 = P_A + \frac{1}{2}\rho(v_1 + v_i)^2 \tag{4}$$

$$From\ disk\ to\ Pt\ 2: P_B + \frac{1}{2}\rho(v_1 + v_i)^2 = P_\infty + \frac{1}{2}\rho v_2^2 \tag{5}$$

Subtracting Equation (4) from Equation (5), we obtain the desired pressure change (P_B - P_A):

$$(P_B - P_A) = \frac{1}{2}\rho\left(v_2^2 - v_1^2\right) \tag{6}$$

Introducing Equation (6) into Equation (3), we can rewrite thrust as follows:

$$T = \frac{1}{2}\rho\left(v_2^2 - v_1^2\right)A_D \tag{7}$$

By equating the forms of thrust in Equations (2) and (7), introducing mass flow as defined at the disk, and cancelling terms, it is possible to establish relationships between the three stream-tube velocities of interest (i.e. v_1, v_2, and v_i).

$$\begin{aligned}
&\dot{m}(v_2 - v_1) = \frac{1}{2}\rho\left(v_2^2 - v_1^2\right)A_D \\
&\rightarrow \rho A_D(v_1 + v_i)(v_2 - v_1) = \frac{1}{2}\rho\left(v_2^2 - v_1^2\right)A_D \\
&\rightarrow (v_1 + v_i)(v_2 - v_1) = \frac{1}{2}(v_2 - v_1)(v_2 + v_1) \\
&\rightarrow v_1 + v_i = \frac{1}{2}(v_2 + v_1) \\
&\rightarrow v_2 = v_1 + 2v_i
\end{aligned} \tag{8}$$

Equation (8) can then be substituted into the thrust Equation (7) to solve for the induced velocity solely in terms of the freestream velocity (v_1) and thrust (T)—key parameters in the desired power and thrust models.

$$
\begin{aligned}
& T = \frac{1}{2}\rho\left(v_2^2 - v_1^2\right)A_D \\
& \rightarrow T = \frac{1}{2}\rho A_D\left((v_1+2v_i)^2 - v_1^2\right) = \frac{1}{2}\rho A_D\left(v_1^2 + 4v_1v_i + 4v_i^2 - v_1^2\right) = 2\rho A_D(v_1v_i + v_i^2) \\
& \rightarrow v_i^2 + v_1v_i - \frac{T}{2\rho A_D} = 0 \\
& \rightarrow v_i = \frac{-v_1 \pm \sqrt{v_1^2 - 4(-\frac{T}{2\rho A_D})}}{2} = -\frac{v_1}{2} \pm \sqrt{\frac{v_1^2}{4} + \frac{T}{2\rho A_D}}
\end{aligned}
\tag{9}
$$

At this point, conservation of energy is applied to the control volume and the amount of energy introduced by the propeller must equal the increase of kinetic energy of the airflow in the stream-tube. With the introduction of the thrust equation stated in Equation (7), the power requirement can be established in terms of freestream velocity (v_1), induced velocity (v_i), and thrust (T).

$$
\begin{aligned}
& Power = \Delta KE = \frac{1}{2}\dot{m}\Delta V^2 \\
& \rightarrow Power = \frac{1}{2}\rho A_D(v_1 + v_i)(v_2^2 - v_1^2) \\
& \rightarrow Power = T \times (v_1 + v_i)
\end{aligned}
\tag{10}
$$

For hovering flight, the freestream velocity (v_1) is zero. Consequently, the formulas for induced velocity and power for hovering flight can be simplified to the following forms.

$$
\begin{aligned}
& v_i = \sqrt{\frac{T}{2\rho A_D}} \\
& Power = T \times v_i = T \times \sqrt{\frac{T}{2\rho A_D}} = \sqrt{\frac{T^3}{2\rho A_D}}
\end{aligned}
\tag{11}
$$

For hovering flight, the required thrust is to balance the weight of the vehicle. As such, the power requirements for hovering flight for a range of mass can be plotted using Equation (11) as illustrated in Figure 11. Given an Aqua-Quad design mass of 3.5 kg and four propellers of 0.356 m (14-in) diameter, the predicted power requirement for hovering flight is ~200 W.

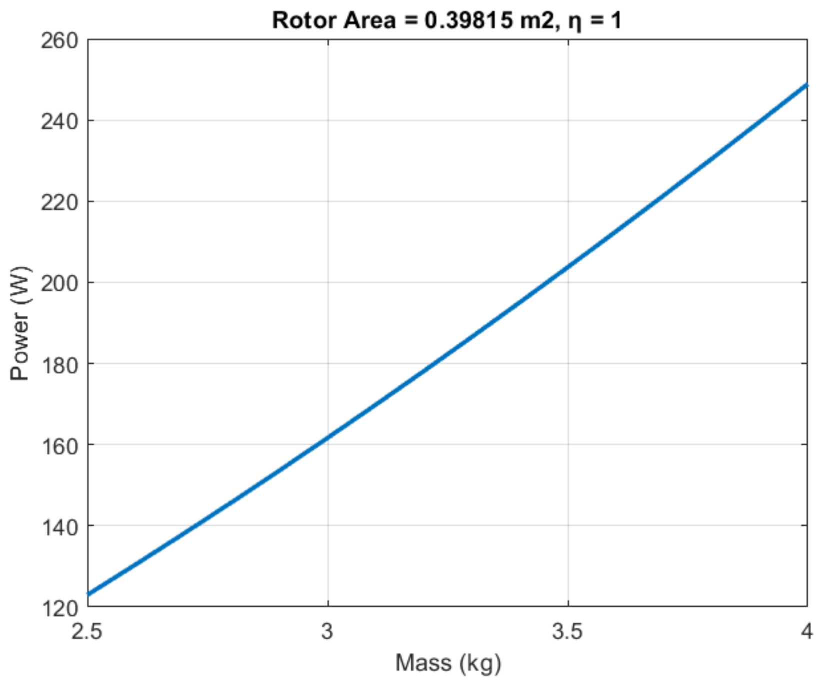

Figure 11. Example of Hovering Power Profile with an Efficiency Factor (η) of 1.0

B. EFFICIENCY FACTOR CORRECTION

The power requirements based on Equation (11) and shown in Figure 11 are ideal and do not factor for the actual power losses experienced by small quadrotors, which usually operate at around 40% of momentum theory [1]. Aqua-Quad flight experiments indicate an overall efficiency that generally agrees with the estimate of 40% for the small quadrotor class. Notably, it was found that quadrotor power efficiency varies between the different phases of flight which require different amounts of control effort to maintain flight stability. The energy flow for the Aqua-Quad or the conversion of energy from the battery to useful propulsion is shown in Figure 12. The efficiency values for each component are based on comparisons with existing literature and the two main categories of losses are electrical and mechanical.

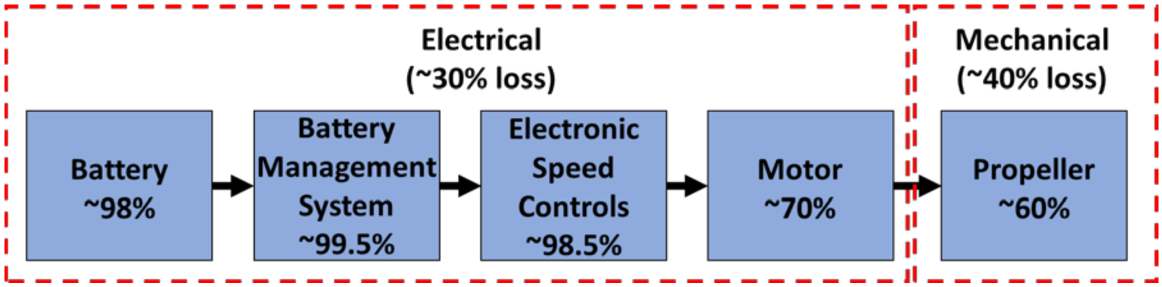

Figure 12. Aqua-Quad Energy Flow and Losses

Like most small quadrotors, the Aqua-Quad uses brushless electric motors to power its rotors. While electric motors are very efficient compared to internal combustion engines, energy conversion from the stored energy in the battery is still not perfect. First, there are power losses that occur with the associated electrical systems, such as the Battery Management System (BMS) and the ESC. Combined with losses in battery discharge and transmission, an estimated 5% of energy is lost even before reaching the electric motors. The electric motors themselves suffer losses through the electrical resistance of wiring, the hysteresis loss during rapid magnetization and demagnetization, and the friction of ball bearings and other moving parts. As a result, electric motor efficiency averages between 70% and 90% [13]. The COTS motors used for the Aqua-Quad are estimated to operate at the lower end of this range—70%.

The other major category of power loss is mechanical power which relates to the efficiency in generating thrust from the propeller rotation. Johnson [14] states that average helicopter propellers lose 22% to 35% of mechanical power to aerodynamic phenomena, such as propeller profile drag, nonuniform inflow, swirl in the wake, and tip losses. Figure 13 lists these power loss components and their nominal values. Compared to the ideal power predicted by momentum theory, termed "ideal induced power" by Johnson [14], real rotors have an efficiency ranging from 65% to 78%. However, Johnson's estimates are based on traditional helicopter propellers which have relatively low disk loading and RPM, resulting in higher efficiency. The small fixed-pitch propellers used for quadrotors are less efficient. Combined with the efficiency of the electrical systems, the overall efficiency is approximately 40%, matching the average efficiency calculated from experiments.

Power component	At peak efficiency	Off peak
Ideal induced power	74% to 78%	65%
Profile power	10% to 19%	25%
Nonuniform inflow	5% to 7%	6%
Swirl in the wake	less than 1%	less than 1%
Tip losses	2% to 4%	3%

Figure 13. Propeller Power Components. Source: [14].

Hovering power experiments have been conducted on quadrotors like the scale-model Aqua-Quad, sharing similar weights, electric motors, and propellers (BOLT WORX 2207L 1660 Kv electric motors and Gemfan Flash 7042 7-in propellers). These experiments determined an efficiency of approximately 40%. Moreover, the efficiency varied with the thrust required as the propellers have fixed pitch blades. Due to the fixed pitch angles, peak propeller efficiency only occurs at a particular “advance ratio” associated with the ideal relative airflow impacting upon the blades. The advance ratio is the ratio of the velocity of the air flow and the rotor tip speed, which is in turn a function of propeller RPM and rotor diameter. Figure 14 illustrates how propeller efficiency typically varies with the advance ratio and blade pitch angle. The increase in advance ratio essentially translates to greater axial air flow and blade pitch angle would have to increase to maintain the same relative airflow angle.

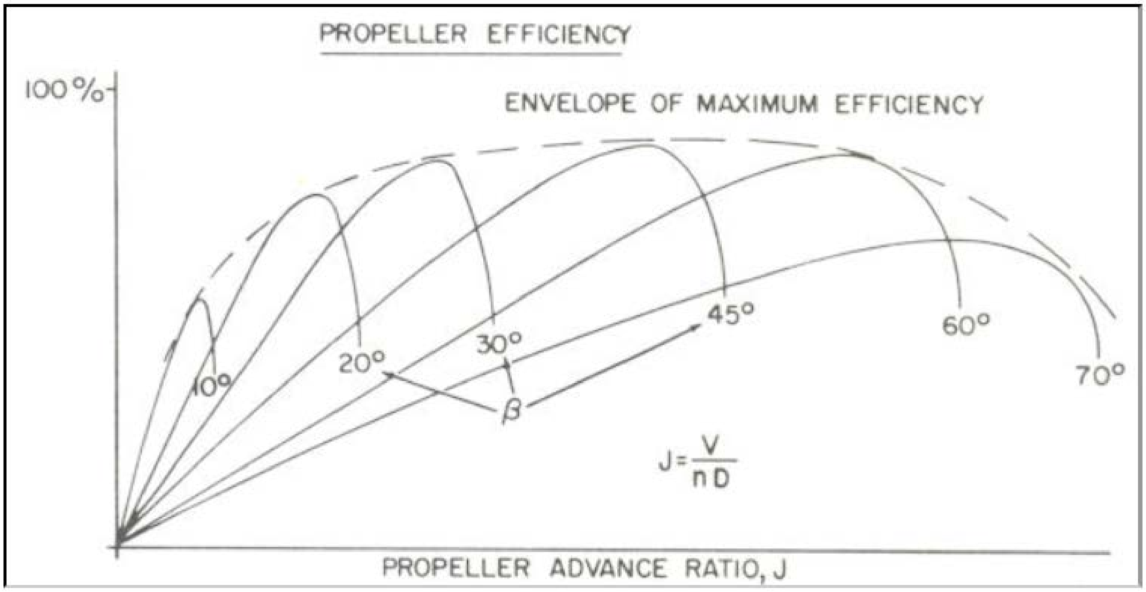

Figure 14. Advance Ratio, Blade Angles, and Propeller Efficiency. Source: [15].

To vary thrust output for flight control, the propellers increase or decrease their RPM. As a result, the changes in thrust output cause changes in the advance ratio and hence the efficiency. Experimental data based on a half-scale model of the Aqua-Quad was used to develop a curve fit for efficiency as a function of disk loading ($\frac{Thrust}{Rotor\ Area}$). Figure 15 shows the resulting power requirements for a constant efficiency of 40% and for efficiency as a function of disk loading. The efficiency increases from 30% to 45% as the disk loading and RPM increases. The efficiency curve is based on the choice of propellers and motors, in addition to the disk loading.

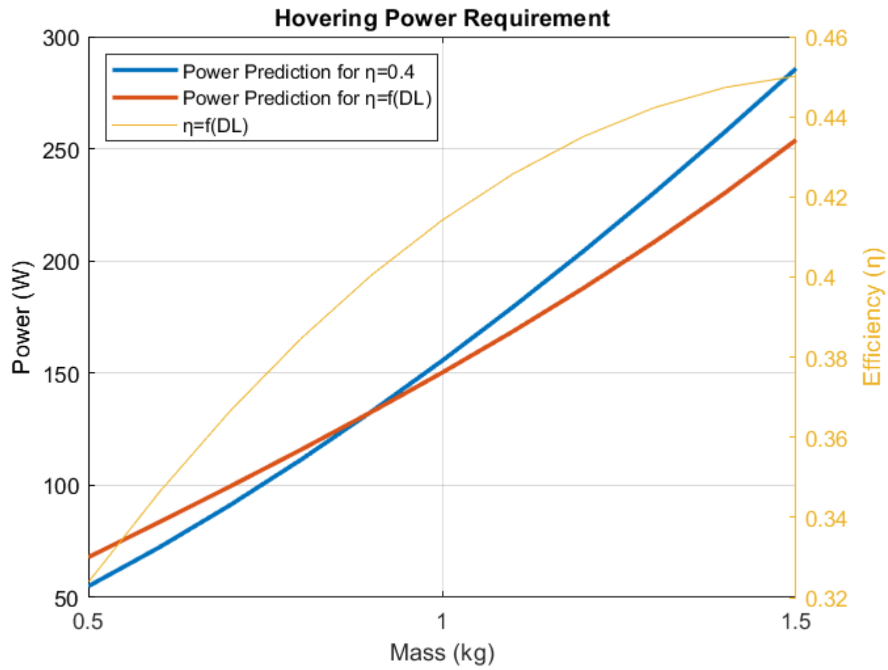

Figure 15. Hovering Power Profiles Corrected for Efficiency

C. FLIGHT TESTS

Flight tests were conducted on the scale model Aqua-Quad to determine the hovering power required. The model was loaded with different amounts of lead weights to obtain the hovering power at different drone weights. The drone was manually controlled to maintain altitude while the autopilot maintained a level drone attitude. Each profile was flown for about 60 seconds to provide sufficient data for analysis. Voltage and current were recorded by the drone telemetry and used to derive the instantaneous power. The mean and standard deviation of the power data were calculated and plotted in Figure 16. The predicted power curve based on an efficiency factor of 0.4 is also plotted in the figure for comparison. The fit of the experimental data to the predicted power curve validates the fundamental physics of the momentum-theory power model.

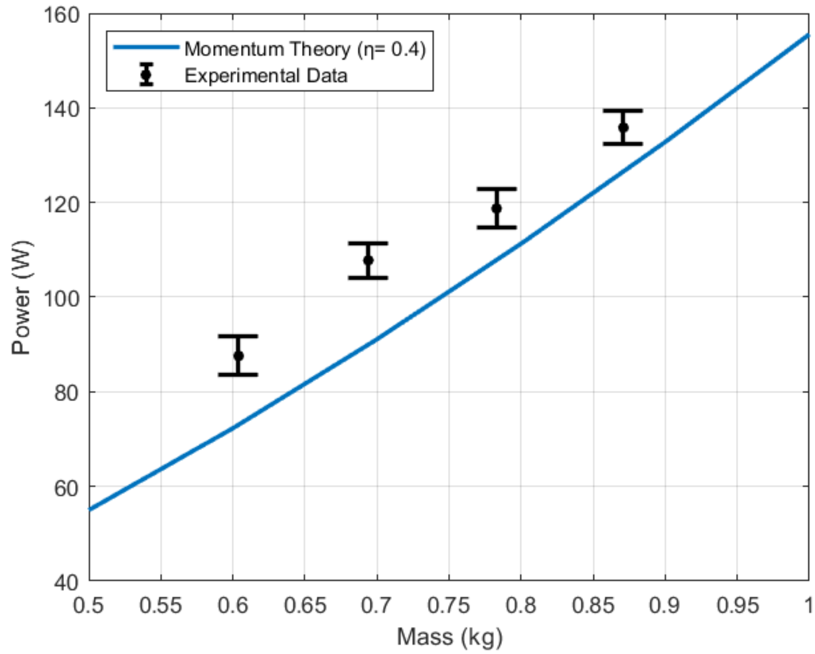

Figure 16. Hovering Power for Scale Model Aqua-Quad

Hovering flight tests were also conducted on the full-size Aqua-Quad prototype. The experimental results and the predicted power curves based on efficiency factors of 0.4 and 0.5 are plotted in Figure 17. For the design mass of 3.5 kg, the power required for hovering given an efficiency factor of 0.4 is 510 W while the power required given an efficiency factor of 0.5 is lower at 410 W. The hovering power curve based on an efficiency factor of 0.5 agrees better with the experimental data. The propellers and motors of the full-scale Aqua-Quad appear to deliver higher energy efficiency.

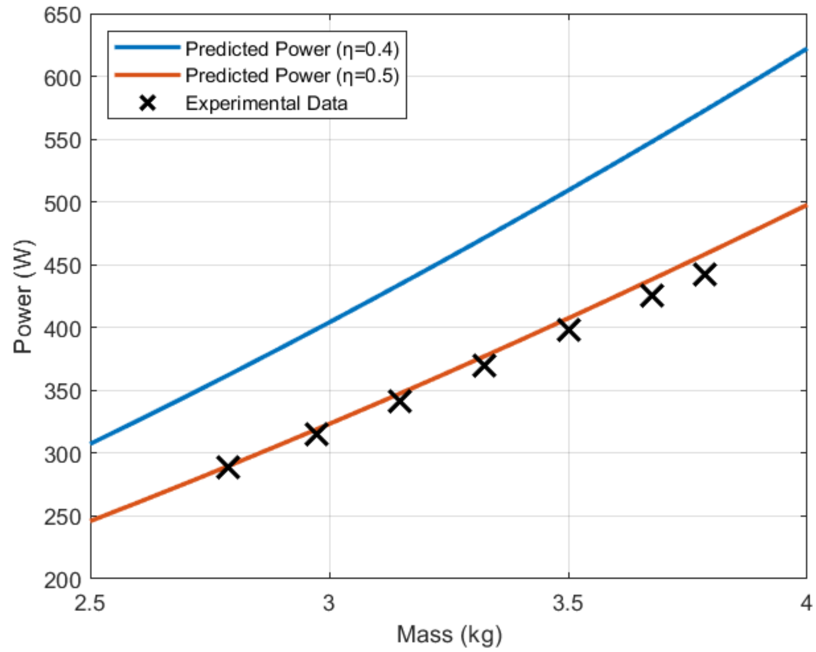

Figure 17. Hovering Power for Full-Sized Aqua-Quad Prototype

THIS PAGE INTENTIONALLY LEFT BLANK

IV. POWER FOR CLIMBING FLIGHT

The Aqua-Quad mission profile requires climbing flight either to reach a cruising altitude to avoid obstacles and terrain, or to reach a height for improved line-of-sight communication. For maritime operations over relatively obstacle-free areas, cruise flight at 100 meters (300 feet) altitude can be expected. In this chapter, the actuator disk theory developed in Chapter III is applied to determine the power requirements for the Aqua-Quad during climbing flight. The major development from Chapter III on hovering flight power is accounting for the drag that develops as the Aqua-Quad climbs vertically, which results in increased thrust and power requirements. In this chapter, the drag characteristics are modeled by theory, experiment, and CFD.

A. THEORY

The actuator disk theory developed in Chapter III was based on a control volume of the airflow through a propeller. For climbing flight, the airflow velocity or freestream velocity (v_1) entering the control volume is the same as the climb speed (v_c) as illustrated in Figure 18. Substituting v_c for v_1 into Equation (9) and rejecting the negative solution, which does not fit the flow model, we obtain the induced velocity (v_i) for climbing flight as:

$$v_i = -\frac{v_C}{2} + \sqrt{\frac{v_C^2}{4} + \frac{T}{2\rho A_D}} \qquad (12)$$

The substitution of induced velocity into Equation (10) gives the power required for climbing flight in terms of v_c and thrust (T). Compared to the hovering case, additional power is required to climb even without factoring for the increased thrust required to offset drag in vertical motion.

$$Power = T \times (v_c + v_i) = T \times (\frac{v_C}{2} + \sqrt{\frac{v_C^2}{4} + \frac{T}{2\rho A_D}}) \qquad (13)$$

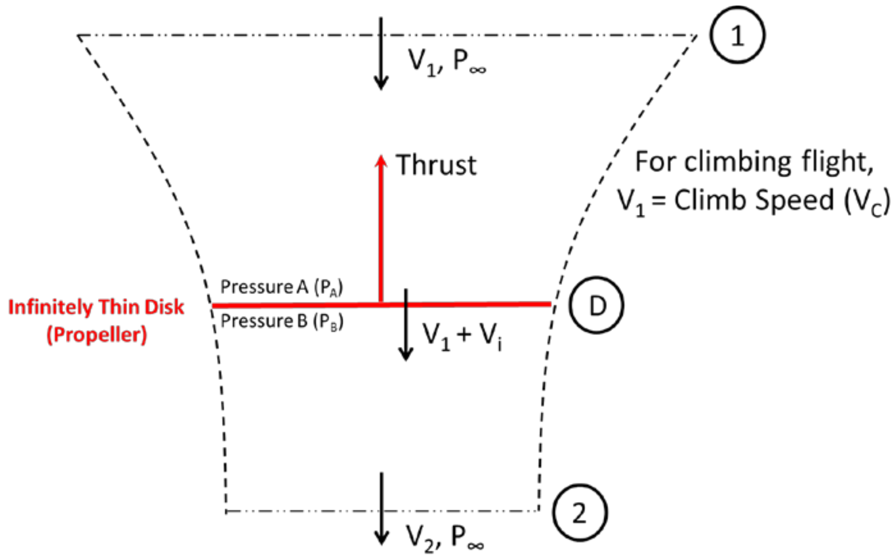

Figure 18. Control Volume for Actuator Disk Theory (Climbing Flight)

B. BASIC DRAG MODEL FOR CLIMB

Additional power is required in climbing flight to overcome the aerodynamic drag encountered. The drag force can be modeled using the standard drag equation where ρ is air density, V is freestream velocity, S is reference area, and C_D is drag coefficient.

$$Drag = \frac{1}{2}\rho V^2 C_D S \tag{14}$$

In this form, the drag characteristics of the Aqua-Quad are reduced to C_D and S. For this study, the reference area S is taken to be the Aqua-Quad surface area that encompasses the solar array but omits the area of the four propeller rotor disks.

Figure 19 illustrates the addition of drag to the power equation, Equation (13). This example is based on a scale Aqua-Quad model used for flight testing with a mass of 1 kg and a reference area of 0.078 m^2. A nominal C_D of 1.28 was used, approximating the drag of the Aqua-Quad with the drag of a flat plate [16]. Other nominal parameters for the calculation are a standard day air density of 1.225 kg/m^3 and a constant efficiency factor of 0.4. For a climb rate of 5 m/s, 1.5 N of drag is generated, resulting in thrust increasing by 15% from 9.81 N to 11.3 N, and power increasing by 22% to 277 W. Drag increases with the square of climb velocity, leading to an exponential increase in climb power. The optimal climb speed to minimize the overall power usage would be at the minimum value of power over velocity, which would be 7 m/s for this case. This value will change for different weights and drag coefficients.

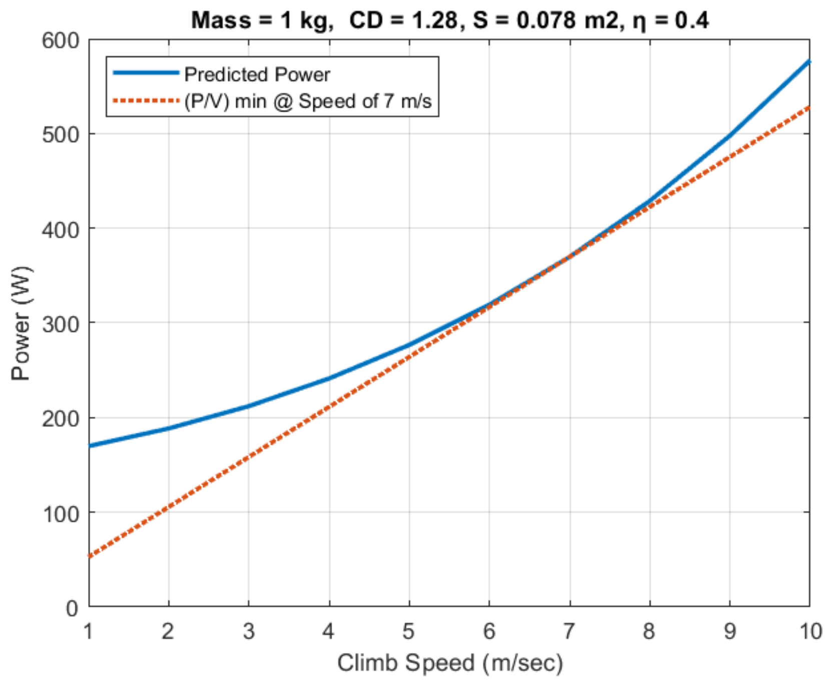

Figure 19. Climb Power for Scale Model of Aqua-Quad

The drag characteristics of the Aqua-Quad are complex. The large solar array and associated support structures act as a blunt body, particularly for vertical climb, resulting in heavy turbulence and separated flow. In addition, the interaction between the airframe and the airflow induced by the propellers is dynamic. The focus of this study's flight tests and CFD is to provide an estimate of the C_D of the Aqua-Quad.

C. FLIGHT TESTS

To better determine the drag of the Aqua-Quad, flight tests were conducted using a scale model as shown in Figure 20. The detailed flight test setup can be found in Appendix A, but in summary, the drone was flown with and without a mock solar array across a range of speeds. By latching on lead weights to the scale model, we could examine a range of drone weights. Besides empirically validating the theoretical models, the flight testing also provides insights on the impact of environmental factors on flight controls and power requirements. Control and stability of quadrotors is achieved primarily through adjusting the thrust and torque of individual motors. The flight tests show that these control efforts lead to additional power expenditures.

Figure 20. Flight Testing of Scale Model Aqua-Quad

The control efforts for steady and stable climb were observed during the flight tests. While the drones were programmed to climb at set speeds, the actual speeds varied possibly due to instrumentation errors or environmental factors, such as wind gusts and updrafts. Figure 21 is the plot of the vertical speeds measured by the on-board barometer and GPS during a test profile that included a climb at 3 m/s to 100 meters, followed by a descent. The weighted average of the filtered vertical speed measurements is fed to the autopilot as the input for control. Based on this input, the autopilot adjusts the throttle settings to achieve the desired climb rate and maintain stable flight. The theoretical climb power model developed earlier does not apply well during the unsteady phases of flight such as rapid accelerations or decelerations.

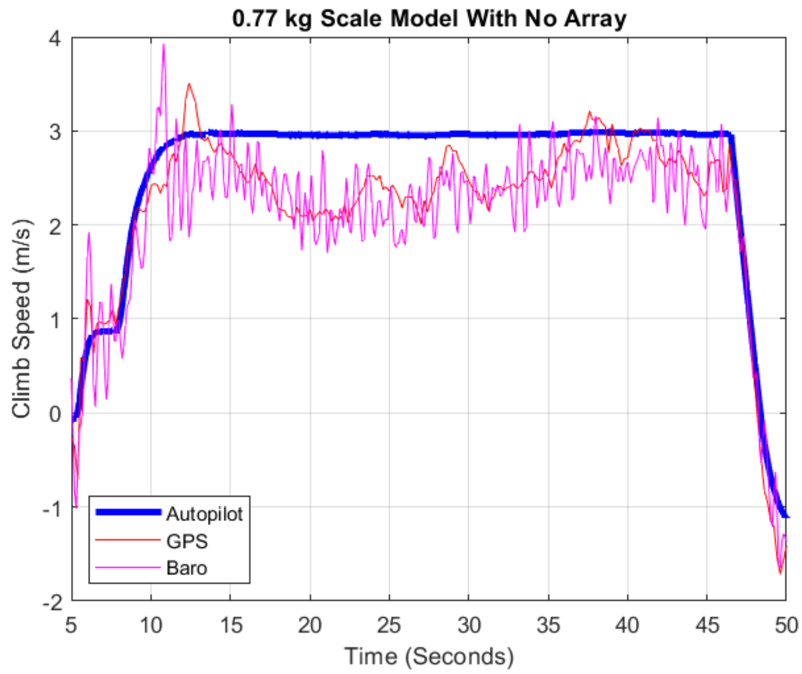

Figure 21. Speed Fluctuations for Commanded Constant-Speed Climb

Even during the stable climb phases, the autopilot and motors need to respond dynamically to maintain aerodynamic stability. The response of the quadrotor autopilot and motors during climb is reflected by the throttle command data—a composite of the individual throttle commands sent to each of the four motors. A time plot of typical throttle command behavior during a constant-speed climb is shown in Figure 22. The figure also shows the associated climb speeds and altitudes of the test profile climb from ground level to 100 meters height at a 5 m/s climb speed. Initially, there were some spikes in throttle command as the drone accelerated to the commanded climb speed. Given lags in motor response and sensor measurements, the steady climb speed of 5 m/s was only reached after about 10 seconds. Once the desired climb speed is reached, the motors are commanded to speed up or down to adjust thrust levels to maintain the climb speed and attitude stability. Overall, the throttle setting for this climb profile remained relatively consistent about a mean value. At the desired height of 100 m, the drone was programmed to descend back down to ground level.

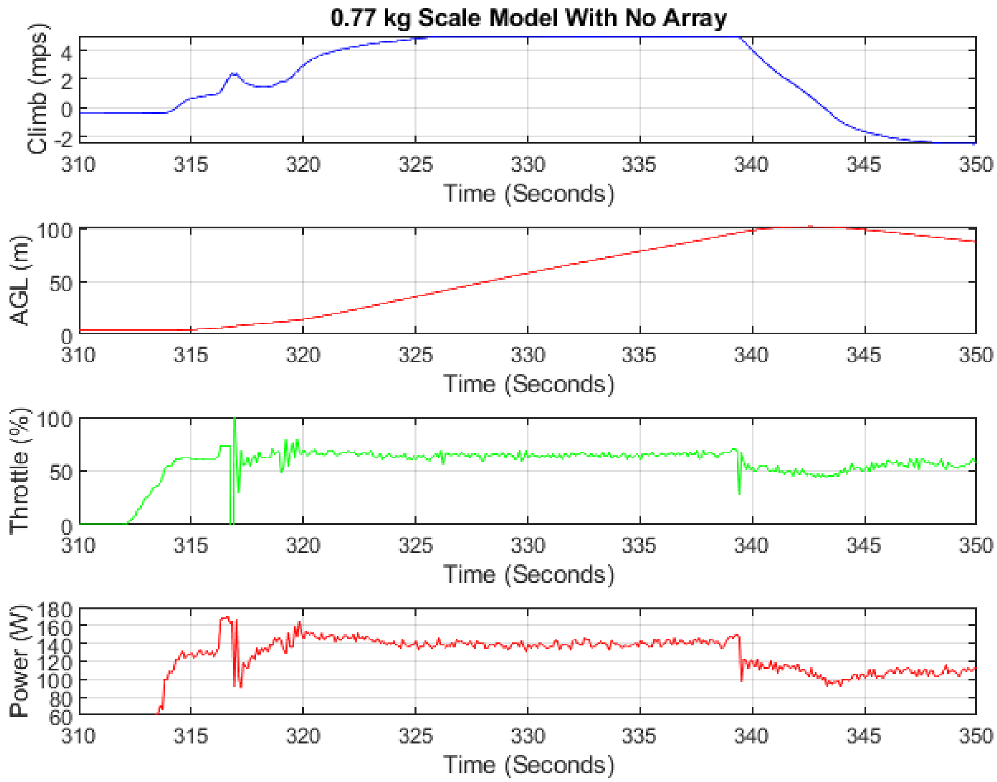

Figure 22. Throttle and Power Response for Constant Speed Climb

The throttle commands are directly related to the power drawn from the battery. The last plot in Figure 22 is a time plot of the power discharged from the battery, calculated from the instantaneous voltage and current measured by the onboard battery system. After initial spikes as the drone accelerated to climb, the power stabilized around a mean power commensurate with the commanded climb speed. This power level was maintained until the desired height was reached and the drone was commanded to descend. While the flight test data has noticeable scatter due to real-world environmental factors, overall, the value of the average power during steady climb validates the theoretical climb model. Figure 23 compares experimental data against the predicted power for the 0.6 kg scale model in a "clean" configuration with no added weights and no mock solar array. With the assumption that the drag in the "clean" configuration is zero and an efficiency factor of 0.4, the theoretical model provides a good representation of actual performance.

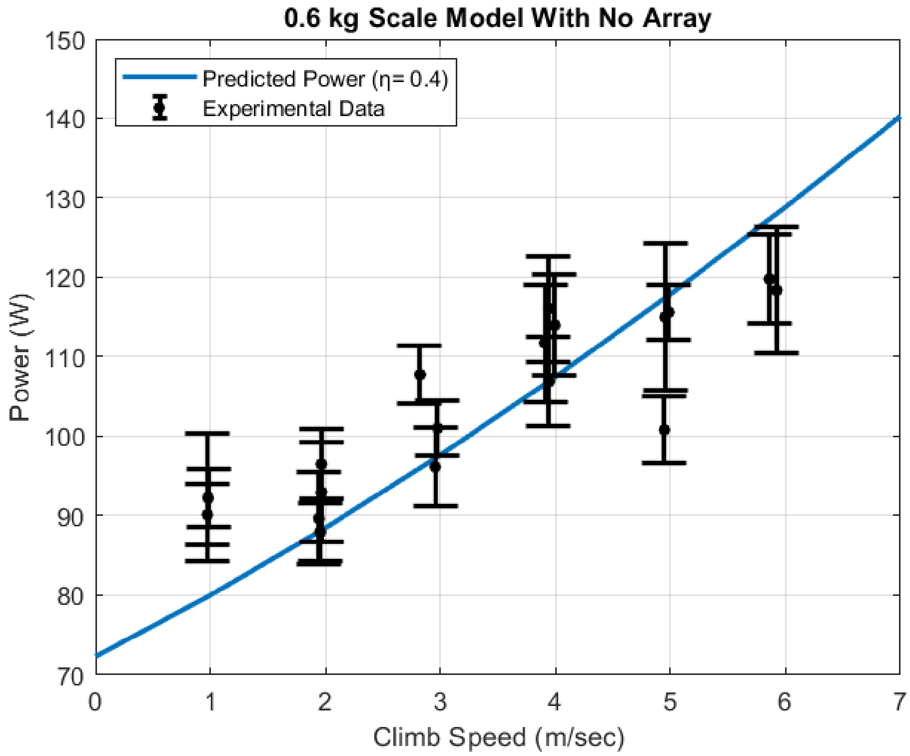

Figure 23. Climb Power Comparison for 0.6 kg Scale Model Aqua-Quad

Figure 24 shows a comparison of the climb power model against the experimental data for a 0.8 kg scale model fitted with the mock solar array. The climb power model in this case accounts for drag and thus increases more exponentially with climb speed. The climb power model was generated for a range of C_D, including zero. Without the drag assumption, the model would significantly underpredict the power requirements. For instance, at 5 m/s climb speed, the no-drag model underpredicts the test data by about 50%. This shows that the drag impact is significant on the power requirements and needs to be taken into account. For an efficiency factor of 0.4, the climb power model matches the experimental data well when using a C_D estimate between 1.5 and 2.4.

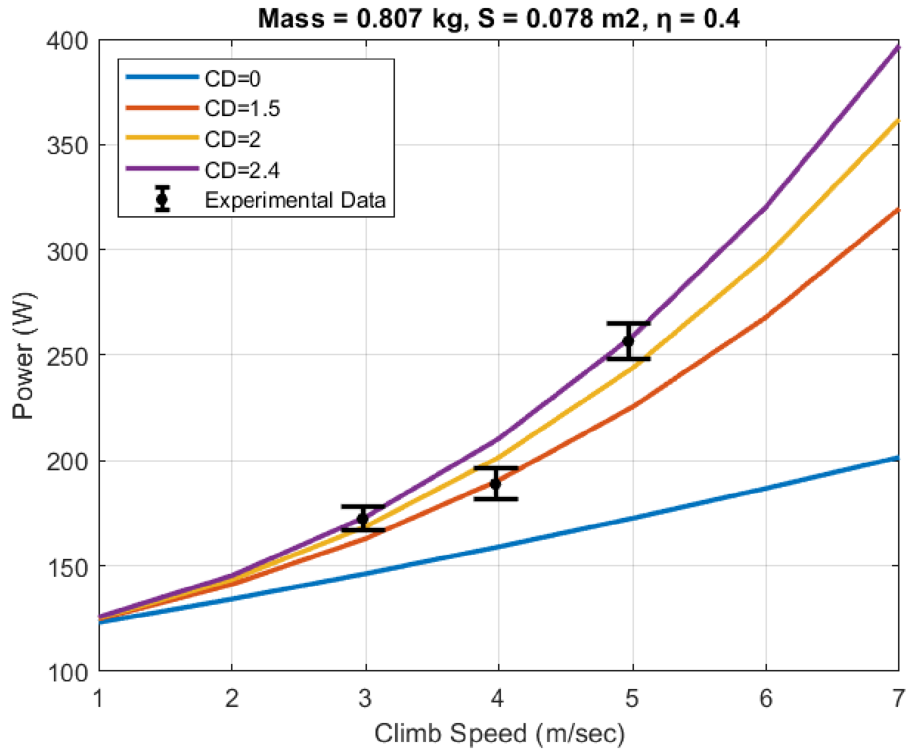

Figure 24. Climb Power Models for Different Drag Coefficients

D. CFD

In addition to flight testing, CFD was conducted to provide a separate independent assessment of the Aqua-Quad drag characteristics. Three phases of CFD were conducted. The first phase was benchmarking the capability of the CFD software ANSYS CFX to model blunt body drag. The second phase involved determining the drag of a simplified Aqua-Quad model, focusing on the solar array, which was assumed to generate most of the drag during vertical flight. The third phase involved drag analysis of a more-detailed Aqua-Quad model, with the addition of motor support arms and the avionics housing, but without the propellers.

1. Blunt Body CFD

It was assessed that the Aqua-Quad quadrotor would behave like a blunt body in flight and the benchmarking exercise thus focused on basic blunt bodies such as disks and cubes. Additionally, a “ring” body, as illustrated in Figure 25, was of particular interest as it was somewhat representative of the Aqua-Quad aircraft structure where airflow passes through the rotors. The derived drag coefficients of these basic body shapes were then compared against empirical data to benchmark the accuracy of ANSYS CFX in analyzing the Aqua-Quad drag.

The blunt bodies were created in SolidWorks and then imported to ANSYS CFX where meshing was conducted. The meshes, ranging in size from 3 million to 8 million nodes, were created with high node density around the shapes and numerous inflation layers along the shape surfaces. Both laminar and turbulent flow models were simulated. On the one hand, the flow speeds were probably slow enough for laminar flow along the surfaces. On the other hand, the wakes behind the blunt bodies would be highly turbulent.

While the laminar models provided similar drag coefficients, the solutions were less stable, fluctuating a few percentage points even after many thousands of iterations. Examination of the velocity and pressure fields for these laminar cases also revealed many unusual features without known physical counterparts. Given the significant flow separation, turbulence modeling was required to stabilize the bulk wake formations. Consequently, the turbulent solutions converged more rapidly to derive C_D values within 11% of empirical data as shown in Table 1. Moreover, examination of the simulated velocity fields and streamlines, such as that shown in Figure 25, did not reveal any unusual phenomena. There was not much of a difference between the K-epsilon (k-ε) and Shear Stress Transport (SST) turbulence models. Overall, it was assessed that ANSYS CFX would provide a reasonable estimation of the drag and lift properties of the Aqua-Quad.

Table 1. Comparison of Drag Coefficients between CFD and Experiments. Adapted from [17] and [18].

Blunt Body Type	***Disk***	***Cube***	***Ring***
Empirical Drag Coefficient	1.17	1.07	1.18
CFD Drag Coefficient (% of Empirical)	1.21 (103%)	1.00 (93%)	1.31 (111%)

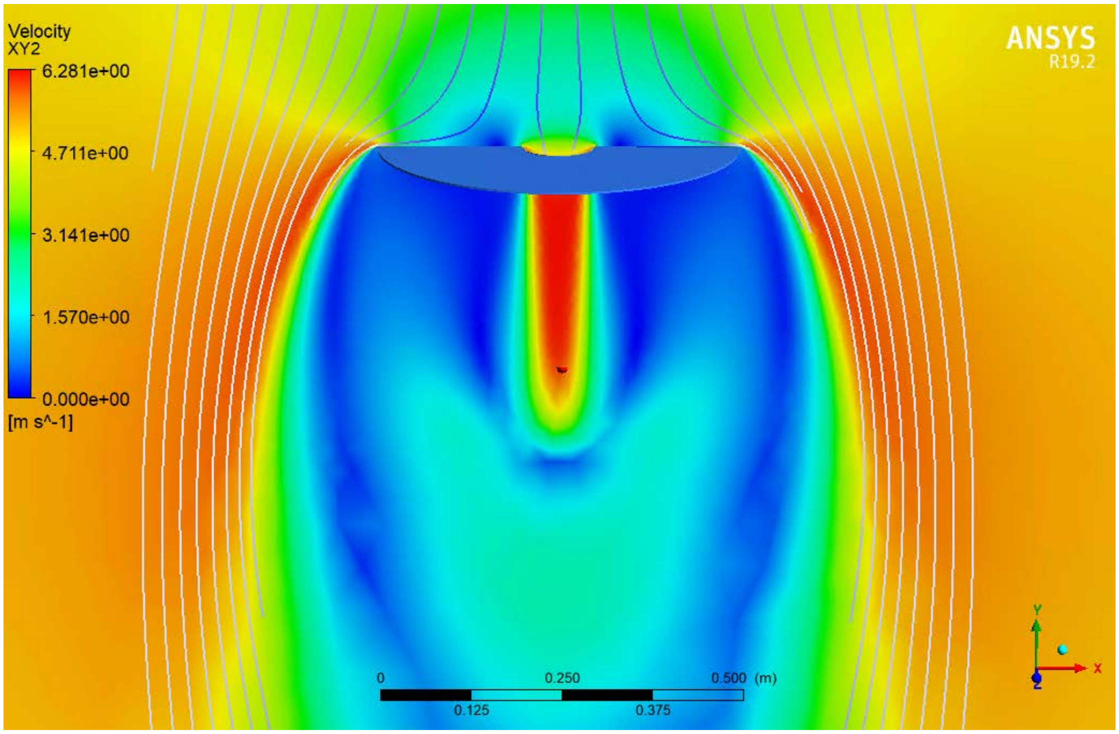

Figure 25. CFD-simulated Velocity Flow Field around a Ring

2. Simplified Aqua-Quad CFD

In the second CFD phase, SolidWorks was used to develop Computer-Aided Design (CAD) models of the solar array, including blade guards, as shown in Figure 26. To reduce computational demands, the CFD modeling was done on the symmetrical half-body. Computational meshes were generated with detailed inflation layers around the body to accurately model boundary layers for skin friction drag estimation and the development of flow separation around the corners. The inflation layer sizing was driven by the goal of keeping the resultant "y+" values below 1.0 while avoiding an excessively large mesh. It was decided to use 30 inflation layers, with a first layer thickness of 1 e-5 m—resulting in a total mesh size of 2 million nodes. The overall fluid domain was also sized at 10 m x 10 m x 5 m, or about 10 times the model size. An illustration of the mesh developed is shown in Figure 27. The upper image shows the entire half-body while the lower image shows the inflation layers along the surfaces at the edge of the array.

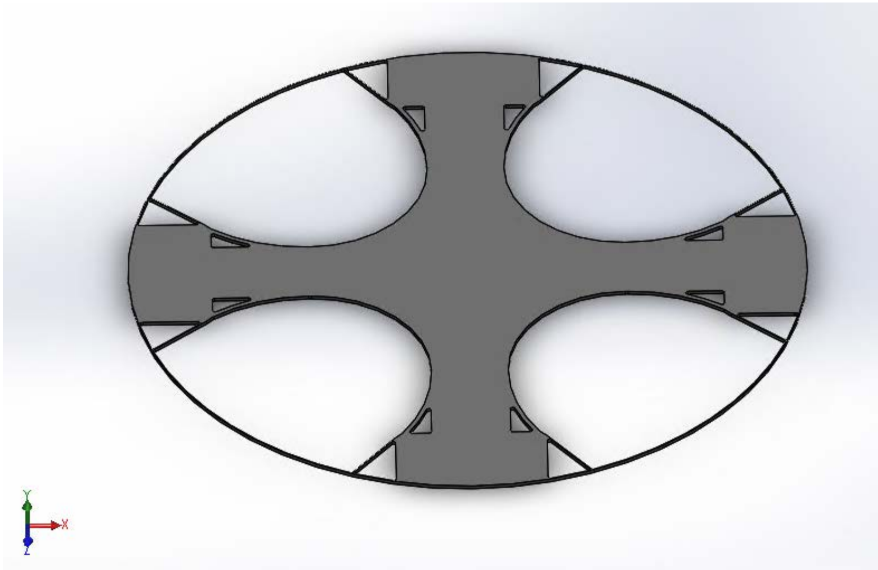

Figure 26. CAD Model of Aqua-Quad Solar Array

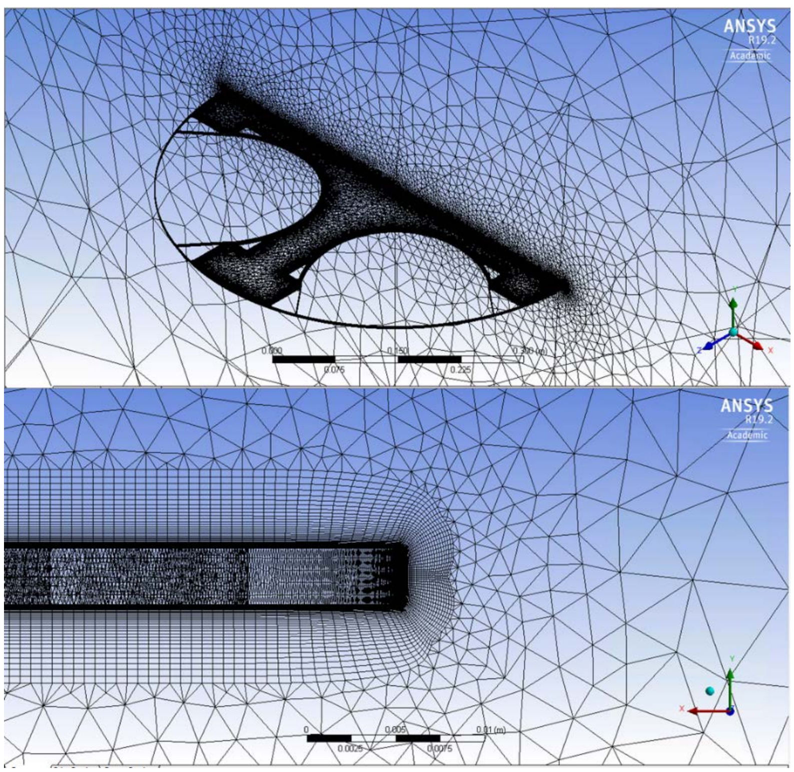

Figure 27. Mesh Generated in ANSYS CFX for Aqua-Quad Solar Array

CFD simulation was conducted on the model created using ANSYS CFX. The simulations were iterated starting with local timesteps and then progressing to physical timesteps until the residuals stabilized. An example of the CFD-simulated pressure distribution around the model in a vertical climb is shown in Figure 28. In the images, red indicates regions of higher pressure and blue indicates regions of lower pressure. In vertical flight, high pressure builds up on the upper surfaces, relative to low pressure on the downstream side of the solar array. In the lower image, the pressure distribution on a horizontal plane 2.5 cm below the solar array is shown. In vertical flight, the solar array acted primarily as a blunt body, resulting in a significant pressure difference across the faces of the solar array and a downstream flow that was highly separated and turbulent. Accordingly, the solutions were unsteady and oscillatory. The simulations were run with appropriately sized physical timesteps until the oscillations were minor with respect to the overall magnitudes.

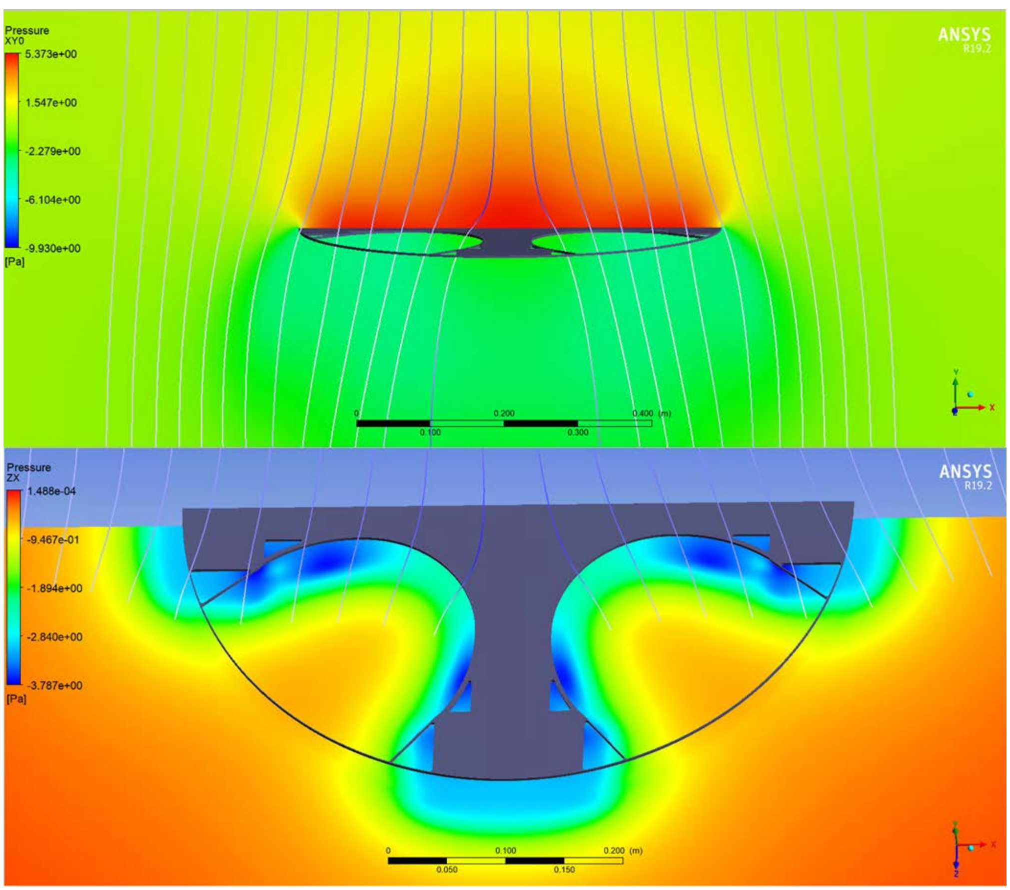

Figure 28. CFD-simulated Pressure Distribution around the Solar Array in Vertical Flight

Overall, the CD of the solar array was estimated to be 1.7. The simulations were conducted using a k-ε turbulence model and for fluid flows of 3 and 5 m/s, which matched two of the field-test conditions. There was no significant difference in the drag coefficient values for the two different Reynolds numbers conditions. The k-ε turbulence model was used as it was computationally cheaper than the SST model. There was a slight difference in the drag results using the different turbulence models, but it was not assessed to be significant given the crude assumptions in the CFD modeling.

3. Detailed Aqua-Quad CFD

CFD was also conducted on a more detailed Aqua-Quad model as illustrated in Figure 29. In addition to the solar array, this model incorporated the main avionics hub and supporting structures, such as the pylons and mounts required to hold the motors and propellers. The propellers themselves, however, were not modeled. In addition, the CFD did not model the flow fields induced by the propellers. Nonetheless, the exercise still provided estimates of drag that approximately matched the estimates from the flight testing.

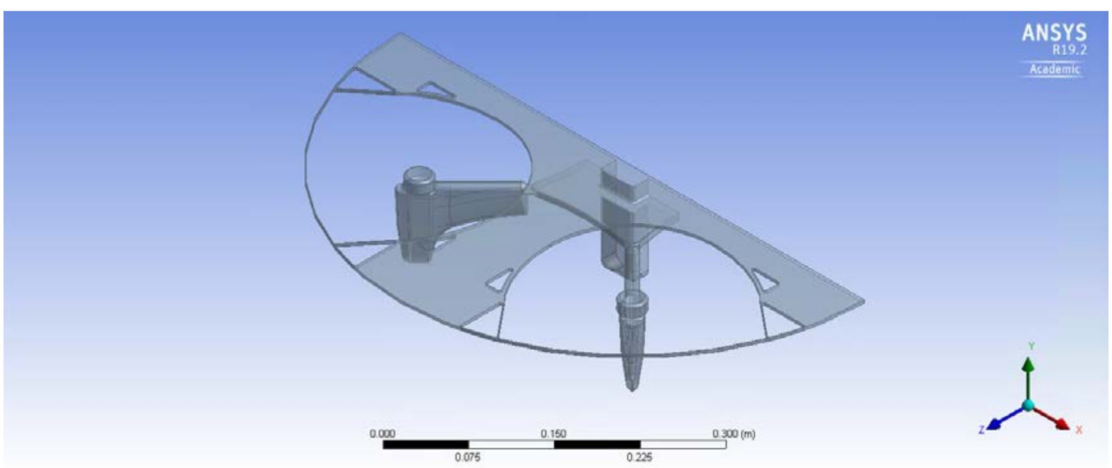

Figure 29. Detailed CAD Model of Aqua-Quad

With the additional body features, the mesh for the detailed Aqua-Quad model was larger, with 13 million nodes. The same inflation layer parameters from the simplified CFD model were used. To control the growth in mesh size, an inner fluid domain was created around the model to restrict the density of cells to the near field. The detailed CFD simulations were more unstable due to the increased separated and turbulent flow arising from additional body features. The oscillatory behavior of the CFD simulations would often grow unbounded if an improper timestep was used. To improve simulation stability, the SST turbulence model with Gamma-Theta transition was used in place of the k-ε model. With careful control of the timestep, reasonably stable solutions were thus obtained for drag. Overall, the detailed model's C_D was 1.8, an increase of 6% from the simplified model's C_D of 1.7.

An example of the CFD-simulated pressure distribution around the detailed Aqua-Quad model in a vertical climb is shown in Figure 30. Red indicates regions of higher pressure and blue indicates regions of lower pressure. In vertical flight, high pressure builds up on the upper surfaces, while low pressure builds on the downstream side of the model where there is separated flow. In the lower image, the pressure distribution on a horizontal plane 5.0 cm below the solar array is shown. These results reflect the significant pressure drag experienced in vertical flight.

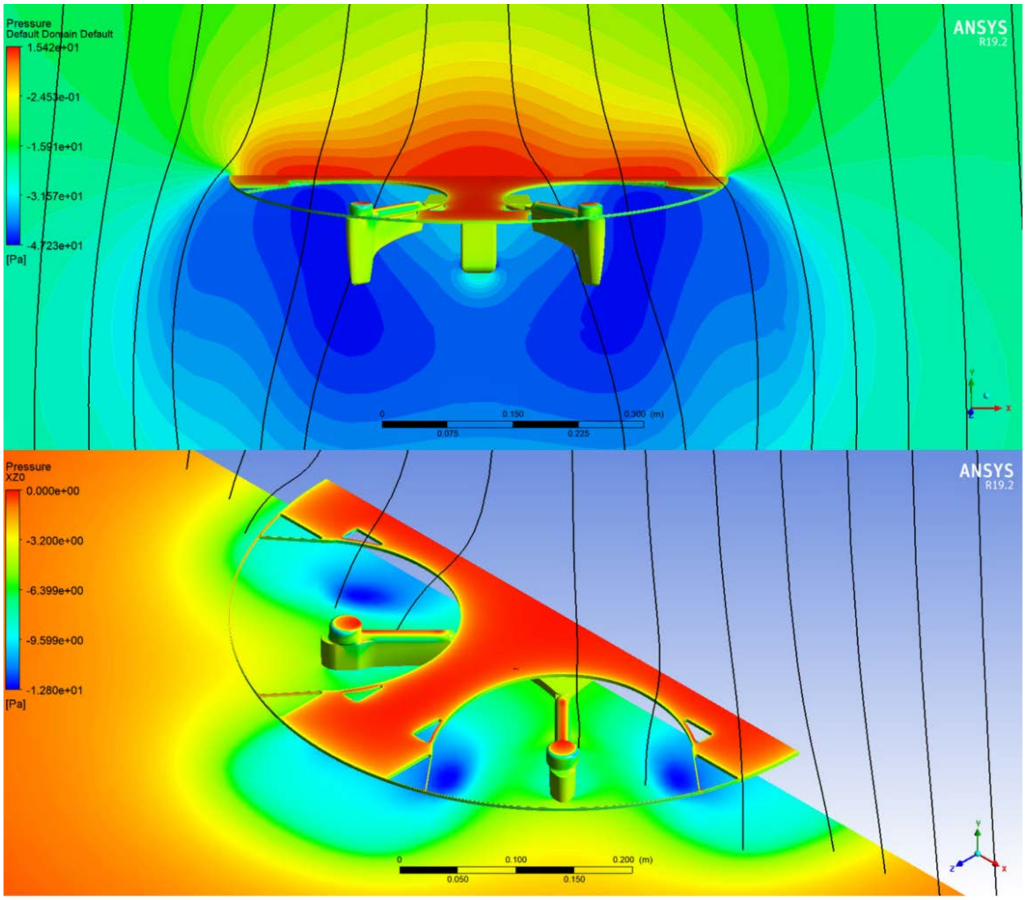

Figure 30. CFD-simulated Pressure Distribution around the Detailed Aqua-Quad Model in Vertical Flight

The drag increase from the simple to detailed model can be attributed in part to the increased skin friction drag of the additional geometric features such as the motor arms. For a nominal case of 5 m/s vertical climb, the CFD-calculated tangential forces in the vertical direction acting on the entire body increased from 0.003N to 0.015N by 400%. The rest of the drag increase is due to the pressure drag acting on the additional geometric features, which increased from 1.947N to 2.053N by 5%. Overall, the increase in drag between the two models was minor because in vertical flight, the primary source of drag is the pressure drag caused by the solar array, which also ends up shielding most of the additional features of the detailed model. In addition, the motor arms and pylons are relatively streamlined in vertical flow. While the lack of a model for the propellers constrains the CFD fidelity, the C_D estimate of 1.8 agrees with the C_D estimate based on field tests of 1.5 to 2.4. Overall, a conservative C_D value of 2.0 is proposed to characterize the drag of the Aqua-Quad in vertical flight.

E. PREDICTION FOR FULL-SCALE AQUA-QUAD

The climb power model developed can be applied to the full-scale Aqua-Quad by scaling for weight and size. The drag coefficient of 2.0 determined for the scale model should apply to the full-scale model given that the two drones differ in size only by a factor of two, resulting in similar Reynolds numbers. The drag force in climb thus only scales based on the increased surface area of the full-scale solar array which is 0.3125 m^2 versus the scale model's 0.078 m^2. Based on a design mass of 3.5 kg and assuming an efficiency of 0.4, the climb power curve for the full-scale model is plotted in Figure 31. Based on this climb power curve, the most efficient climb speed of 5 m/s occurs when $\frac{Power}{Speed}$ is a minimum. This climb speed requires 1060 W of power and a 20-second climb to a nominal cruise altitude of 100 m AGL will consume 6 Wh.

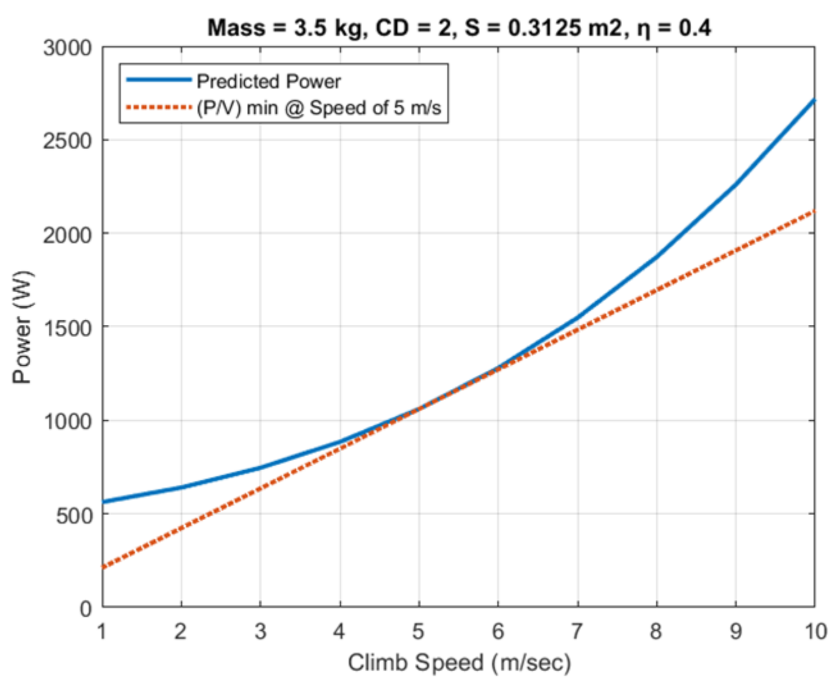

Figure 31. Climb Power Required for Full-scale Aqua-Quad

V. POWER FOR DESCENDING FLIGHT

While descending flight is the last segment of the Aqua-Quad flight profile, its power requirements are described here, following Chapter IV on climbing power, due to similarities in the analysis. For traditional helicopter analysis, momentum theory can be applied to descending flight only when the rate of descent is high enough to develop a well-defined slipstream above the propeller. As the Aqua-Quad has large flat surfaces, the high speed of this windmill brake state would cause excessive aerodynamic forces and possible loss of stability and control. Moreover, small quadrotors like the Aqua-Quad use fixed-pitch propeller blades that do not properly windmill in descending flight in the same way as the large variable-pitch rotors used by traditional helicopters. Consequently, momentum theory is developed in this chapter mainly for completeness and to set physical bounds for the relatively complex behavior of descending flight.

The Aqua-Quad is expected to descend at a gradual speed much less than the windmill brake state. This descent regime, between the hovering state and the windmill brake state, is described by the literature on helicopter theory as Vortex Ring State (VRS) and turbulent wake state [19], [20]. In these conditions, there is unsteady air recirculation through the propeller. Figure 32 illustrates these conditions, alongside the windmill brake state and the normal working state for hovering and climbing flight. Johnson [19] explains:

> At small rates of descent, recirculation near the disk and unsteady, turbulent flow above the disk begin to develop. The flow in the vicinity of the disk is still reasonably well represented by the momentum theory model, however. Because the change in flow state for small rates of climb or descent is gradual, the momentum theory solution remains valid for some way into the vortex ring state. Eventually … the flow even near the rotor disk becomes highly unsteady and turbulent. The rotor in this state experiences a high vibration level, and aircraft motion can develop that is difficult to control. In particular, in the vortex ring state the power required is not very sensitive to vertical velocity, and hence controlling the descent rate is difficult in this region.

As there lacks a simple theory to describe these turbulent states, empirical models from the literature were examined and compared with flight test data to characterize a descent power model for the Aqua-Quad. Overall, it was found that the control efforts to maintain quadrotor stability in descent were significant, reducing the overall power efficiency. In addition, the solar array introduced additional aerodynamic forces that required further control efforts. Rather than "braking" the descent and reducing power demands, the solar array increased power requirements.

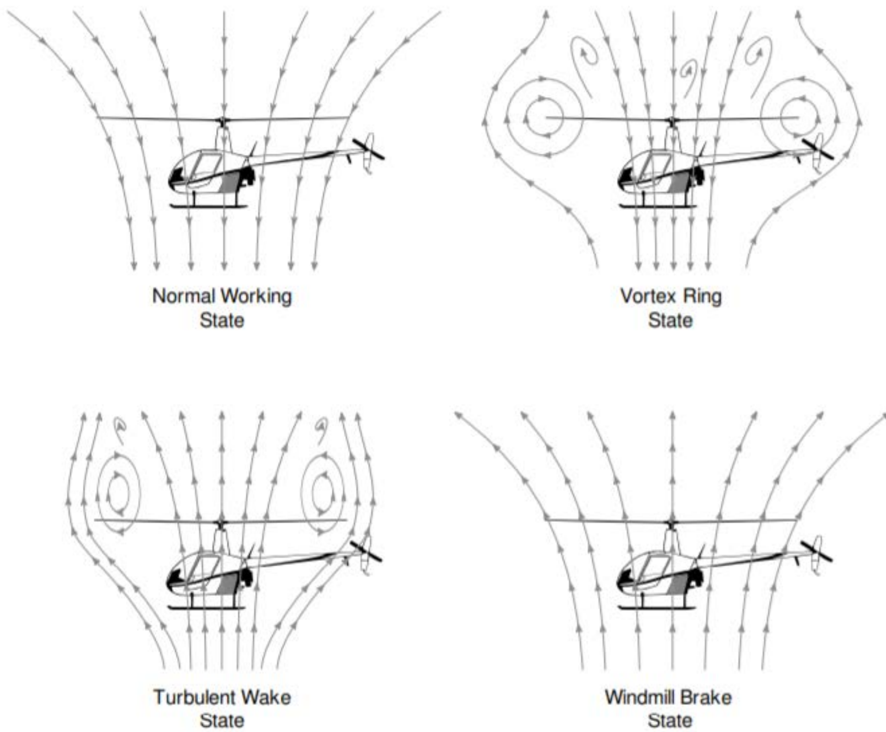

Figure 32. Illustration of Four Primary Operation States for a Helicopter Propeller. Source: [21].

A. THEORY

The application of momentum theory for descending flight maintains the same control volume used in the earlier chapters on hovering and climbing flight. For descending flight, however, the airflow now enters the control volume from below and exits from above. In addition, the propeller slows the airflow down in effect, adding an induced velocity (v_i) that is opposite to the direction of the airflow. These changes are illustrated in Figure 33.

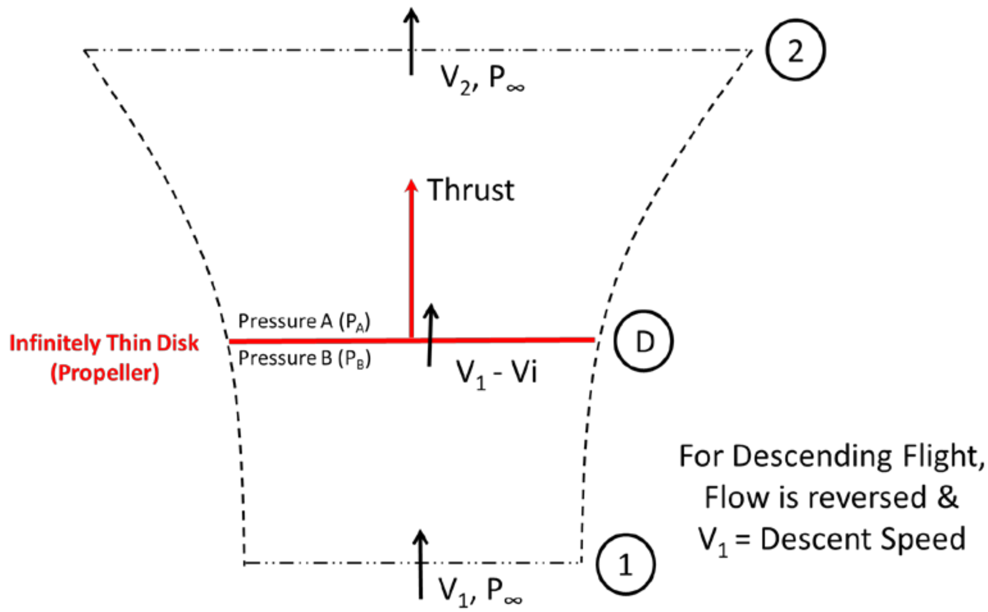

Figure 33. Control Volume for Actuator Disk Theory (Descending Flight)

With the direction changes in velocities, the earlier equations for mass flow, pressures, and thrust are rewritten as follows:

$$\dot{m}_D = \rho A V = \rho A_D (v_1 - v_i) \tag{15}$$

$$T = \dot{m}\Delta v = \dot{m}(v_1 - v_2) = \rho A_D (v_1 - v_i)(v_1 - v_2) \tag{16}$$

$$\begin{aligned} &\text{From Pt 1 to disk}: P_\infty + \frac{1}{2}\rho v_1^2 = P_B + \frac{1}{2}\rho (v_1 - v_i)^2 \\ &\text{From disk to Pt 2}: P_A + \frac{1}{2}\rho (v_1 - v_i)^2 = P_\infty + \frac{1}{2}\rho v_2^2 \\ &(P_B - P_A) = \frac{1}{2}\rho\left(v_1^2 - v_2^2\right) \end{aligned} \tag{17}$$

$$T = (P_B - P_A) A_D = \frac{1}{2}\rho\left(v_1^2 - v_2^2\right) A_D \tag{18}$$

By equating the two different thrust equations, Equations (16) and (18), the change in flow direction establishes a new relationship for the exit velocity (v_2) at the top of the control volume and the induced velocity (v_i) produced by the propeller.

$$
\begin{aligned}
&\rho A_D(v_1 - v_i)(v_1 - v_2) = \frac{1}{2}\rho\left(v_1^2 - v_2^2\right)A_D \\
&\rightarrow (v_1 - v_i)(v_1 - v_2) = \frac{1}{2}(v_1 - v_2)(v_1 + v_2) \\
&\rightarrow (v_1 - v_i) = \frac{1}{2}(v_1 + v_2) \\
&\rightarrow v_2 = v_1 - 2v_i
\end{aligned}
\tag{19}
$$

$$
\begin{aligned}
&T = \frac{1}{2}\rho\left(v_1^2 - v_2^2\right)A_D \\
&\rightarrow T = \frac{1}{2}\rho A_D\left(v_1^2 - v_2^2 - (v_1 - 2v_i)^2\right) \\
&\rightarrow T = 2\rho A_D(v_1 v_i - v_i^2) \\
&\rightarrow v_i^2 - v_1 v_i + \frac{T}{2\rho A_D} = 0 \\
&\rightarrow v_i = \frac{v_1}{2} \pm \sqrt{\frac{v_1^2}{4} - \frac{T}{2\rho A_D}} \rightarrow \frac{v_1}{2} - \sqrt{\frac{v_1^2}{4} - \frac{T}{2\rho A_D}}
\end{aligned}
\tag{20}
$$

In the descending flight model, the flow of air in the control volume is upwards, with positive values for v_1, v_2, and v_i. Referring to Equation (19), we note that a positive solution for v_2 is only possible with a negative quadratic root. Additionally, there is no solution for $\frac{v_1^2}{4} - \frac{T}{2\rho A_D} < 0$. Alternatively, this translates to the observation that the momentum theory for descending flight is only applicable for $v_1 > \sqrt{\frac{2T}{\rho A_D}}$, a value twice the induced velocity for hovering flight or v_h, see Equation (11) in Chapter III. Descent between hovering and twice the value of v_h is associated with the VRS and Turbulent Wake states where the control volume for momentum theory "breaks down" and cannot be properly established. As the descent rate increases past twice v_h, the windmill brake state arises where momentum theory can be applied [19]. In this case, the propellers are extracting power from the airflow, at a rate calculated as follows using the conservation of energy and the relationships developed earlier.

$$
\begin{aligned}
&Power = \Delta KE = \frac{1}{2}\dot{m}\Delta V^2 \\
&\rightarrow Power = \frac{1}{2}\rho A_D (v_1 - v_i)(v_1^2 - v_2^2) \\
&\rightarrow Power = T \times (v_1 - v_i)
\end{aligned}
\tag{21}
$$

$$
\begin{aligned}
&Power = T \times (v_1 - v_i) = T \times (v_1 - (\frac{v_1}{2} - \sqrt{\frac{v_1^2}{4} - \frac{T}{2\rho A_D}})) \\
&Power = T(\frac{v_1}{2} + \sqrt{\frac{v_1^2}{4} - \frac{T}{2\rho A_D}})
\end{aligned}
\tag{22}
$$

Figure 34 shows a power curve based on Equation (22), using parameters associated with the scale model Aqua-Quad. As explained earlier, current multi-copter designs are unable to exploit this wind-milling state, which is presented here mainly to complete the understanding of momentum theory.

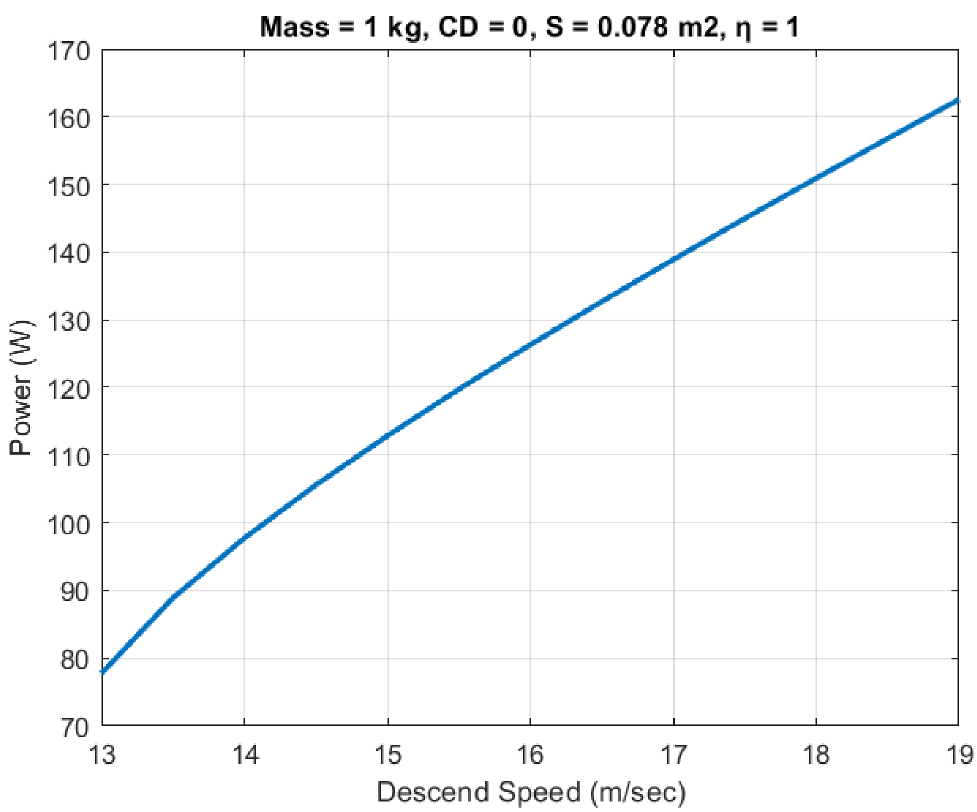

Figure 34. Power *Extracted* by the Propeller in Windmill Brake State

B. POWER ESTIMATES IN VORTEX RING STATE

The Aqua-Quad is expected to descend in a transitional regime between the "normal working state" at hover and the VRS where the induced propeller wake begins to recirculate back into the propeller inflow. There are no simple analytical models to describe the turbulent and unsteady nature of this descent regime. Instead, the available literature uses empirical data to characterize the propeller characteristics in this condition. Leishman [20] offers the following approximation based on National Advisory Committee for Aeronautics (NACA) experimental data for the velocity induced (v_i) on the airflow during VRS, normalized by the velocity induced during hovering flight (v_h) and as a function of vertical speed (v_1).

$$\frac{v_i}{v_h} = k - 1.125\left(\frac{v_1}{v_h}\right) - 1.372\left(\frac{v_1}{v_h}\right)^2 - 1.718\left(\frac{v_1}{v_h}\right)^3 - 0.655\left(\frac{v_1}{v_h}\right)^4 \tag{23}$$

$$\textit{where } k \textit{ is the induced power factor } (=1 \textit{ for ideal})$$

The empirical relationship between induced velocity and vertical speed as stated in Equation (23) is plotted in Figure 35. The figure also shows the induced velocity for the normal working state and the windmill brake state. For climbing flight, v_1 is positive while for descending flight, v_1 is negative.

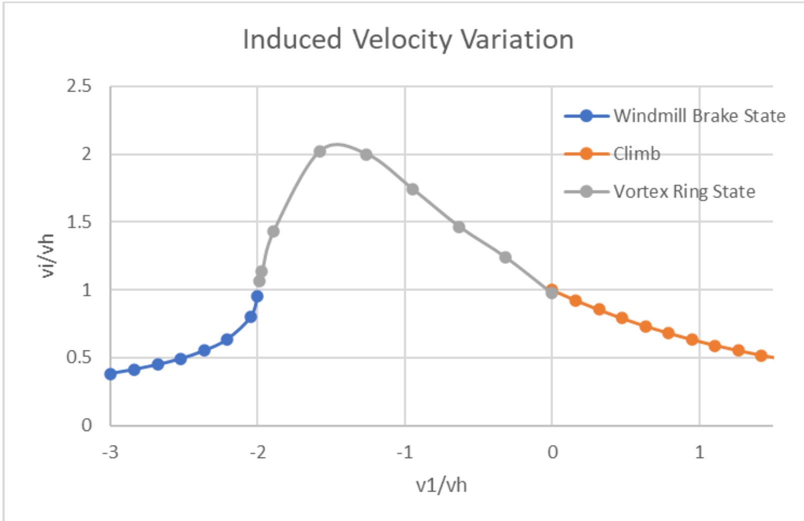

Induced Velocity (v_i) for Different Vertical Speeds - Normalized against the Induced Velocity for Hovering Flight (v_h)

Figure 35. Actuator Disk Induced Velocity

Based on the predicted induced velocity, the power required to descend during VRS can be calculated as follows and as shown in Figure 36 along with the power requirements for normal working state and windmill brake state.

$$Power = Thrust \times (v_1 + v_i) \tag{24}$$

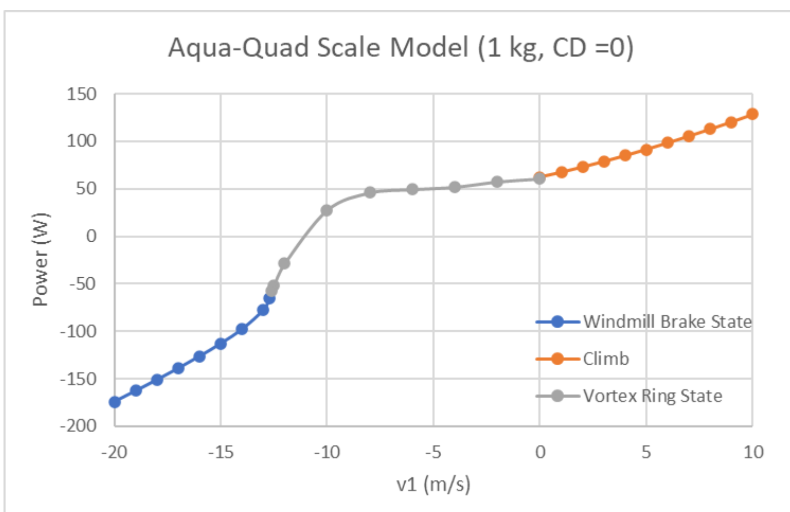

Figure 36. Example of Power Required in Vortex Ring State, Windmill Brake State, and Climb

For a gradual descent close to the hovering state, the expected power required is close to the hovering flight power. As descent speed increases beyond approximately $\frac{v_1}{v_h} = -1.5$, the power expected would drop as the windmill brake state is approached. For the thrust and rotor size of the scale model Aqua-Quad, this would occur at a descent rate of approximately 10 m/s. At this speed, there would be significant drag and aerodynamic forces due to the large solar array. Lastly, the fixed-pitch propellers of the Aqua-Quad would not fully windmill, unlike a traditional helicopter. Consequently, the Aqua-Quad descends at a gradual descent just below hover, and the power required would be expected to be close to hover power. Flight tests, however, indicate that the control efforts during descent lead to power requirements greater than these predictions.

C. FLIGHT TESTS

Flight tests conducted on the scale model Aqua-Quadprovided data on the descent power for a range of descent speeds. The flight tests were conducted in the same fashion as the flight tests for climb power. Figure 37 illustrates the trends observed by showing the average power for descent speeds of approximately 1 to 3 m/s based on one weight configuration. Climb data for the same drone configuration is also plotted in the figure. The predicted power for climb and descent were generated assuming an overall system efficiency of 40%. While the climb model fits the experimental data reasonably well, the descent model significantly underpredicts the actual power. This could be a result of a decrease in efficiency due to additional control efforts required to maintain attitude stability as the quadrotor descends into its own propeller wake.

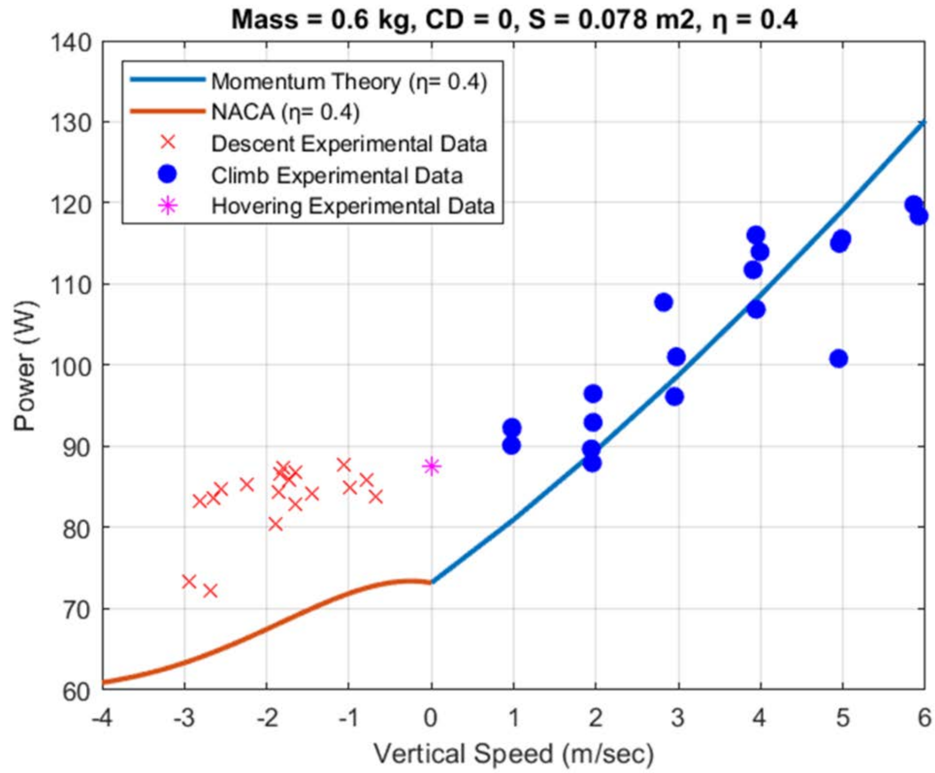

Figure 37. Theoretical Power Models for Descent Compared against Experimental Data

Flight test data indicates that the descent is more unstable compared to the climbing state. This could be attributed to the recirculation of airflow into the propellers as the quadrotor descends into its turbulent wake, thus causing unsteady fluctuations in the thrust output of the rotors. To maintain attitude stability, the quadrotor autopilot must issue compensatory commands to each motor. The transient nature of this control effort incurs a significant efficiency penalty. Figure 38 shows an example of the overall throttle response behavior during climb and descent. The overall throttle response is a telemetry data field that represents the averaged throttle levels of the four motors. The flight profile described in the figure involves the drone being commanded to climb at 5 m/s to 100 meters above ground level and then commanded to descend at 2 m/s. Comparing the steady climb and descent segments, the throttle fluctuations are greater during descent than during climb.

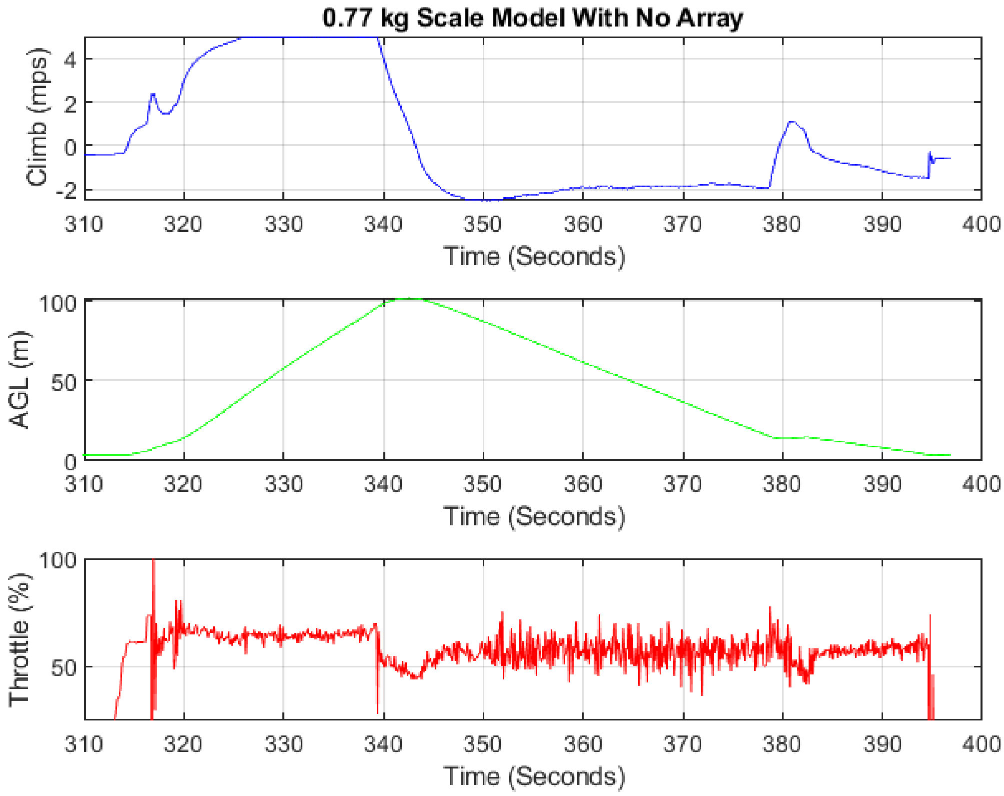

Figure 38. Throttle Response during Climb and Descent

The unsteady nature of quadrotor descent was observed in almost all the descent profiles tested. Figure 39 shows the mean and standard deviation values of commanded throttle at different vertical speeds. The average scatter or standard deviation of the throttle is 213% larger for descent than for climb, meaning that the quadrotor autopilot is making more drastic throttle changes during descent. Correspondingly, the descent power also had slightly higher scatter compared to climb power as shown in Figure 40. The average scatter for climb power was 5.5 W versus 7.7 W for descent power. Overall, the UAS autopilot also had more difficulty maintaining the desired constant speed profiles in descent as shown in Figure 41. The scatter of descent speeds is more than 600% greater than for climb speeds, reflecting the impact of the unsteady nature of quadrotor descent on the performance of maintaining the commanded vertical velocity.

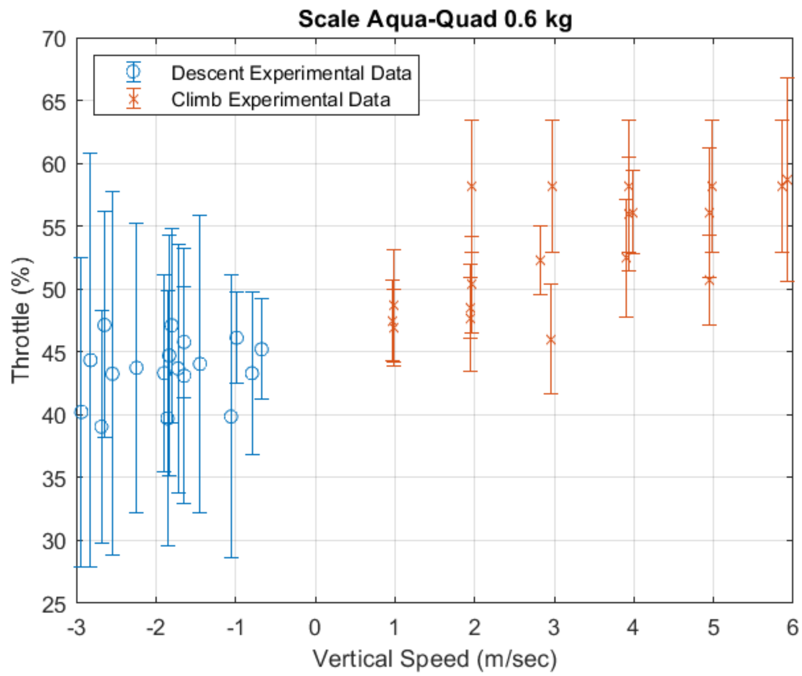

Figure 39. Throttle Mean and Standard Deviation for Various Vertical Speeds

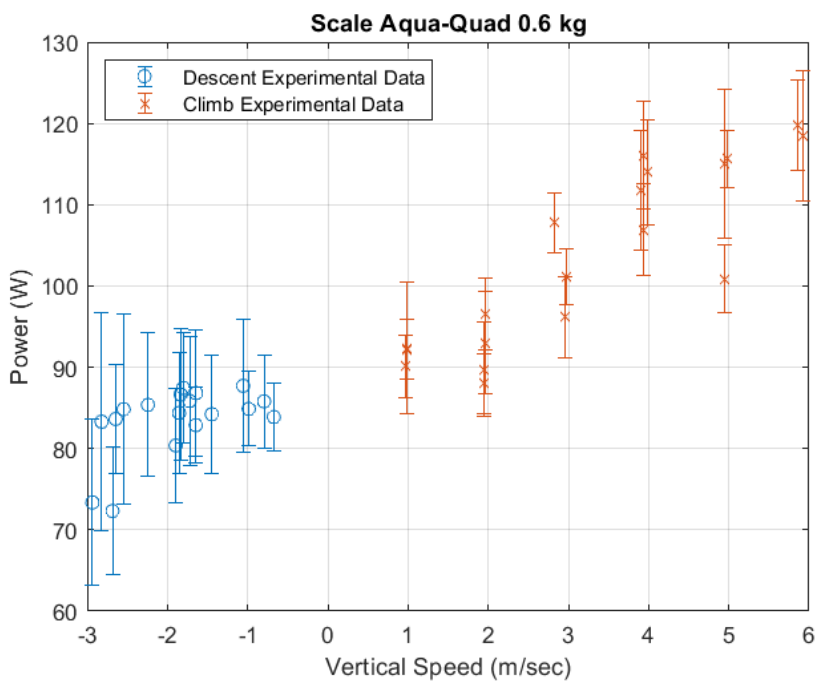

Figure 40. Power Mean and Standard Deviation during Commanded Constant Vertical Speeds

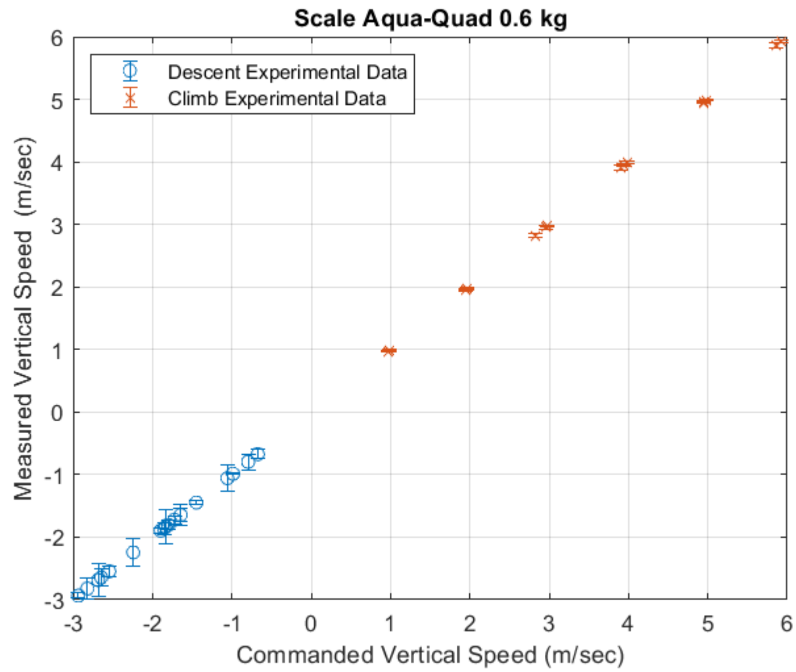

Figure 41. Speed Mean and Standard Deviation during Commanded Constant Vertical Speeds

The predicted power for descent must consider the increased control efforts. There is a significant efficiency drop as the quadrotor control system seeks to maintain stability while it descends through its turbulent wake. Unsteady recirculation through the propellers randomly affects thrust output and the motors need to adjust rapidly to compensate for thrust imbalances between the four propellers. The increases in RPM need to overcome inertia and the overall motor operation is more inefficient compared to near-constant RPM operations. As shown in Figure 42, while an efficiency factor of 0.4 was appropriate in climb, the efficiency factor appears to drop to under 0.35 during descent. Consequently, a more efficient descent profile would include forward movement to move the rotors out of the recirculation cells—a profile often employed by helicopters.

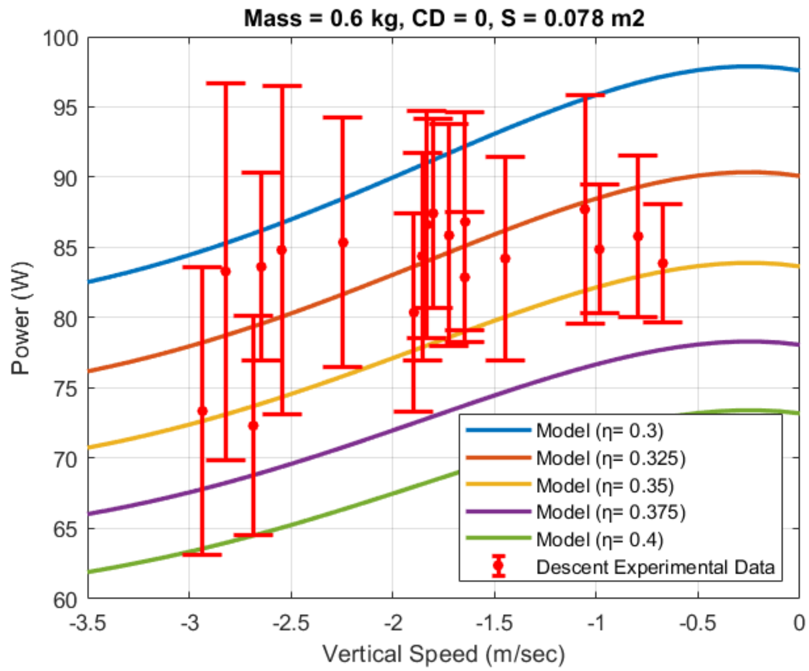

Figure 42. Estimating Efficiency during Quadrotor Descent

While drag would intuitively reduce the thrust required in descent, the test data indicates that the solar array may have a destabilizing effect, requiring additional control efforts that offset the “braking” effect. For analysis, it was assumed the drag in descent would be similar to the drag in climb, estimated to have a C_D ranging from 1.5 to 2.4. In theory, the climb drag should be a close match to the descent drag as both are driven by the blunt body drag of the symmetric solar array. Assuming 35% efficiency, power curves based on drag coefficients ranging from 0 to 2.4 were plotted together with experimental data as shown in Figure 43. The figure shows that the power curves with drag applied slightly underpredict the measured power. On the other hand, the power curve with no drag (C_D =0) slightly overpredicts the measured power. While the experimental scatter is high, the test data suggests that the solar array may have a destabilizing effect that degrades power efficiency in descent.

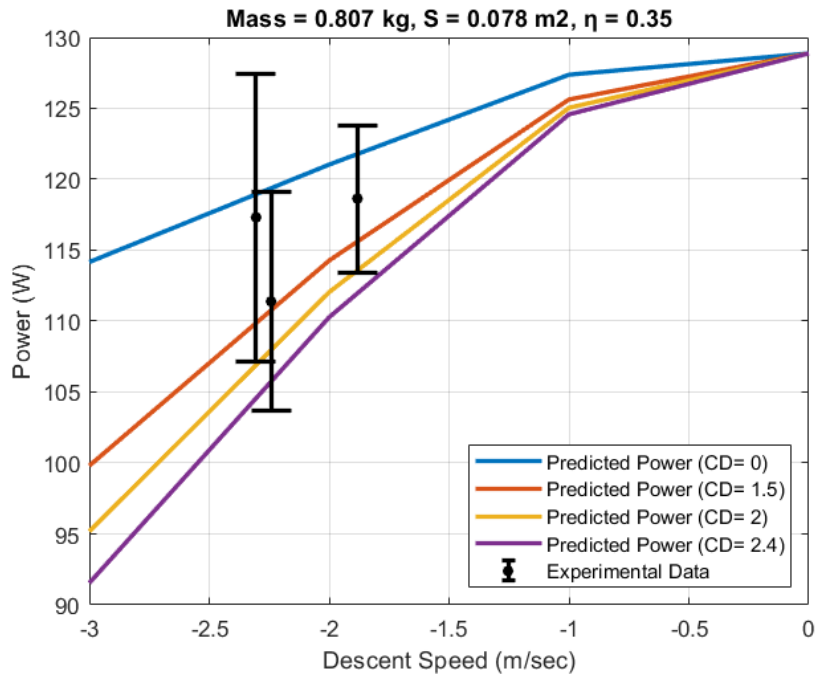

Figure 43. Theoretical Power Descent Model for Different Drag Coefficients Compared against Experimental Data

D. PREDICTION FOR FULL-SCALE AQUA-QUAD

As with the case for climbing flight, the power model for descending flight can be applied to the full-scale Aqua-Quad by scaling for weight and size. The descent power curve shown in Figure 44 was generated based on a drag coefficient of 2.0, assuming similar aerodynamic characteristics between the scale model and the full-scale model. The power curve in the figure was also generated based on an efficiency of 35%, lower than the 40% determined for the climbing case due to the expected control losses when descending into the turbulent wake. Given stability concerns and the need to transition to touchdown at a gentle rate, a slow descent rate of 2 to 3 m/s can be expected. For a descent speed of 2 m/s, the predicted power required is 510 W. Descending from a nominal cruise altitude of 100 m AGL, this descent profile would take up to 50 seconds and consume up to 7 Wh of battery charge. In practice, performance could be improved by flying an angled descent with horizontal velocity that moves the drone out of its turbulent wake. This would reduce the recirculation effect on the propellers and improve the overall efficiency.

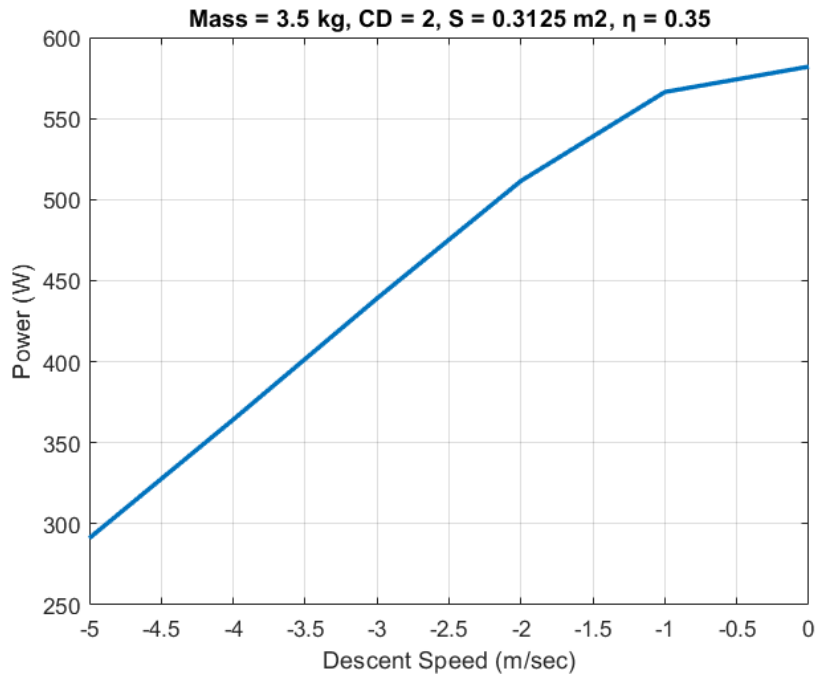

Figure 44. Descent Power Required for Full-scale Aqua-Quad

THIS PAGE INTENTIONALLY LEFT BLANK

VI. POWER FOR CRUISE FLIGHT

The main power draw for the Aqua-Quad mission will be during cruise flight as the Aqua-Quad repositions. As detailed in this chapter, the cruise power requirements can be determined from the actuator disk theory introduced in earlier chapters, by modifying the airflow stream-tube model from 1-D to 2-D. A new sub-model is also needed to predict the thrust and the angle of attack (AOA or α) of the airflow entering the actuator disk for a given cruise speed. The three parameters of cruise speed, thrust, and AOA are coupled by the balance of forces illustrated in Figure 45, namely thrust, weight, lift, and drag. This chapter will thus also cover the resolution of these forces through theory, flight testing and CFD.

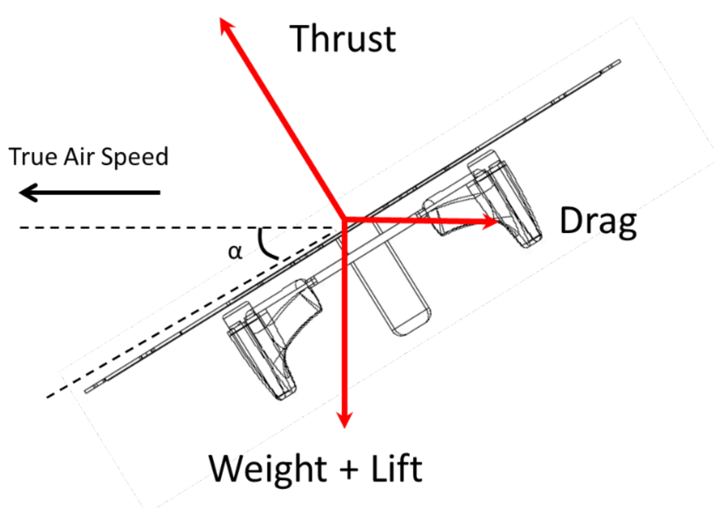

Figure 45. Force Balance of the Aqua-Quad in Cruise

A. THEORY

The application of momentum theory for horizontal flight adopts a 2-D airflow model. This 2-D model essentially adds a horizontal component to the 1-D model used for vertical flight, as examined in earlier chapters. The control volume associated with the 2-D airflow model is shown in Figure 46. Airflow enters the 2-D control volume with a freestream velocity (V). The actuator disk then adds an induced velocity (v_i) to the airflow in the direction normal to the disk. The airflow finally leaves the control volume back at freestream pressure but with an added wake speed (W) in the direction normal to the disk. Of note, the AOA or angle of the freestream flow relative to the propeller is assumed to approximate the pitch attitude angle of the quadrotor.

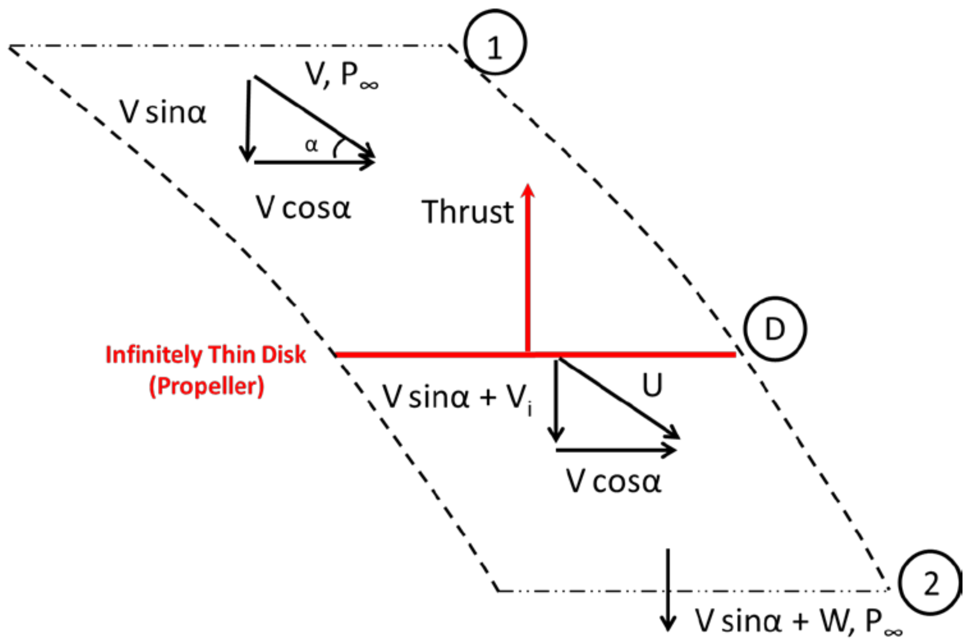

Figure 46. Control Volume for Actuator Disk Theory (Cruise Flight)

Based on work by Hermann Glauert [20], momentum theory can be developed for horizontal flight by recognizing that mass is conserved as the 2-D airflow passes through the actuator disk or propeller. As shown in Equation (25), this mass flow rate ($\dot{m}$) is defined by the air density, the cross-sectional area of the disk, and a resultant velocity (U) that is composed of both horizontal and vertical components of the airflow at the disk.

$$\begin{aligned} &\dot{m} = \rho A_D U \\ &where\, U^2 = \left(V\cos\alpha\right)^2 + \left(V\sin\alpha + v_i\right)^2 = V^2 + 2Vv_i\sin\alpha + v_i^2 \end{aligned} \tag{25}$$

In addition, it is observed that momentum is conserved in the direction normal to the disk, and the thrust developed by the propeller (T) is thus defined as the change in momentum in the normal direction, which is the mass flow multiplied by the increase in the wake speed in the normal direction (w).

$$T = \dot{m}\Delta V = \dot{m}w \tag{26}$$

By definition, power is the rate of work given by the thrust that acts in a direction normal to the actuator disk and the rate of the airflow moving in the same direction normal to the disk. Cruise power can thus be predicted given the thrust required, the freestream velocity, the AOA, and the induced velocity.

$$P = T(v_i + V\sin\alpha) \tag{27}$$

To derive a useful form of Equation (27), a relationship can be found to determine induced velocity in terms of thrust, freestream velocity, and AOA. This derivation begins by applying the conservation of energy across the control volume, where it is determined that the power added to the control volume is equivalent to the increase in kinetic energy of the airflow defined in terms of the freestream velocity, added wake speed, and AOA.

$$\begin{aligned} P &= \frac{1}{2}\dot{m}\Delta V^2 \\ &= \frac{1}{2}\dot{m}[(V\sin\alpha + w)^2 + (V\cos\alpha)^2 - V^2] \\ &= \frac{1}{2}\dot{m}[V^2\sin^2\alpha + 2Vw\sin\alpha + w^2 + V^2\cos^2\alpha - V^2] \\ &= \frac{1}{2}\dot{m}[2Vw\sin\alpha + w^2] \end{aligned} \tag{28}$$

Equating the two expressions for power shown in Equations (27) and (28), and substituting in the expression for thrust as shown in Equation (26), we obtain an expression for the increase in wake speed (w) in terms of the induced velocity (v_i)

$$
\begin{aligned}
& P = T(v_i + V\sin\alpha) = \frac{1}{2}\dot{m}[2Vw\sin\alpha + w^2] \\
& \rightarrow \dot{m}w(v_i + V\sin\alpha) = \frac{1}{2}\dot{m}[2Vw\sin\alpha + w^2] \\
& \rightarrow v_i w + Vw\sin\alpha = Vw\sin\alpha + \frac{1}{2}w^2 \\
& \rightarrow v_i = \frac{1}{2}w
\end{aligned}
\tag{29}
$$

The formulation of thrust in Equation (26) can now be rewritten by substitution of Equations (25) and (29).

$$
\begin{aligned}
& T = \dot{m}w \\
& \rightarrow T = \rho A_D U 2v_i \\
& \rightarrow T = 2\rho A_D v_i \sqrt{V^2 + 2Vv_i\sin\alpha + v_i^2}
\end{aligned}
\tag{30}
$$

By recalling the relationship for induced velocity for hovering flight ($v_h^2 = \dfrac{T}{2\rho A_D}$), we obtain the following relationship for induced velocity.

$$
\begin{aligned}
& T = 2\rho A_D v_i \sqrt{V^2 + 2Vv_i\sin\alpha + v_i^2} \\
& \rightarrow T = 2\rho A_D v_i \sqrt{(V\cos\alpha)^2 + (V\sin\alpha + v_i)^2} \\
& \rightarrow v_h^2 2\rho A_D = 2\rho A_D v_i \sqrt{(V\cos\alpha)^2 + (V\sin\alpha + v_i)^2} \\
& \rightarrow v_i = \frac{v_h^2}{\sqrt{(V\cos\alpha)^2 + (V\sin\alpha + v_i)^2}}
\end{aligned}
\tag{31}
$$

For constant air density, thrust, and actuator disk area, there is a unique value for the induced velocity for hovering power (v_h) as shown in Chapter III. Accordingly, Equation (31) is the determination of the induced velocity based on thrust, freestream velocity, and AOA. MATLAB can be used to solve for the value of the induced velocity, which appears on both sides of the equation. The MATLAB scripts used for this report are included in the Appendix.

For many traditional helicopters, the angle of attack is near constant and small during horizontal flight. For such a case, Equation (31) is plotted in Figure 47 showing that the induced velocity decreases initially with horizontal speed. In accordance with Equation (27), as the induced velocity drops, the rotor power output also drops. This leads to a bucket-shaped power curve for traditional helicopters. In other words, more power is consumed during a stationary hover than during level cruise flight.

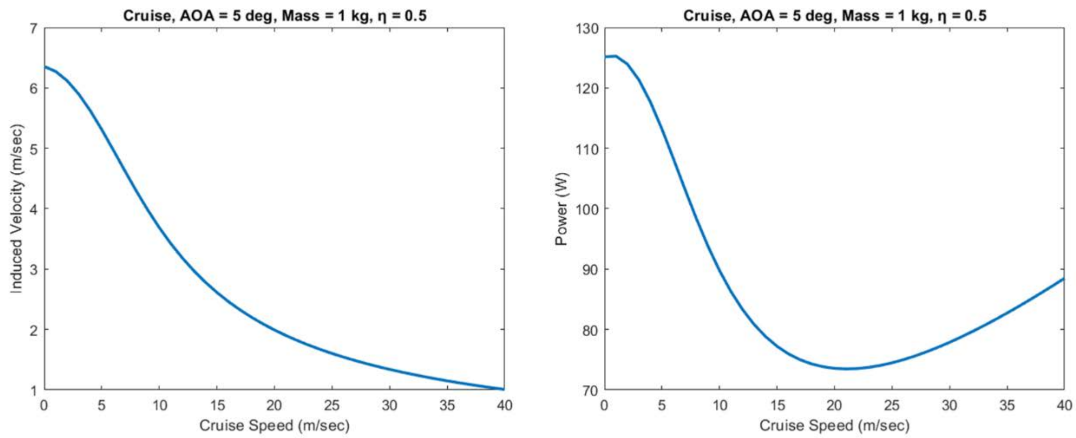

Figure 47. Actuator Disk Theory: Induced Velocity and Power for Cruise Flight at Constant Angle of Attack

Unlike traditional helicopter aircraft, most quadrotors require high angles of attack for horizontal flight and do not fully share the “bucket-shaped” power curve. As small quadrotors rely on simple propellers without a collective mechanism, the only way to generate the horizontal force necessary for horizontal flight is for the entire aircraft to rotate. This results in a proportional relationship between horizontal speeds and the angle of attack. As shown in Figure 48, for a constant horizontal speed, increases in the angle of attack result in increased power. The overall effect for a typical quadrotor is an exponential power curve that increases gently as speed increases. This type of curve is reflected in the experimental power curves obtained during the flight tests conducted for the Aqua-Quad.

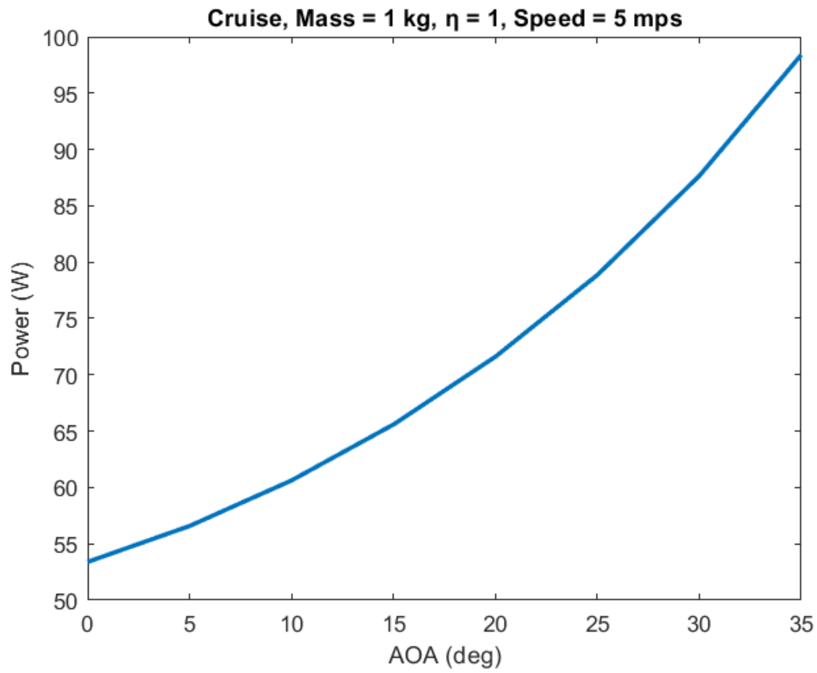

Figure 48. Angle of Attack Impact on Power for Constant Cruise Speed

B. THRUST AND LIFT DURING CRUISE

Using Equations (27) and (31), we can determine an analytical solution for cruise power given thrust, freestream velocity, and pitch angle. This task, however, is complicated by the fact that these three parameters are coupled together. To cruise horizontally, the quadrotor "pitches" forward to rotate its thrust vector in the direction of travel, accelerating until drag balances the axial thrust component. Added complexity arises because as the quadrotor pitches, thrust needs to increase to balance the weight vector to maintain level flight. Thrust also needs to increase to balance the negative "lifting effect" of the Aqua-Quad solar array that arises with cruise speed and pitch angle. The cruise power model thus needs to develop a sub-model that relates thrust and pitch angle to freestream velocity.

Ideally, the analytical power model of the Aqua-Quad in cruise would use accurate lift and drag models to determine the thrust and pitch required at various cruise speeds. Lacking a good theoretical model for blunt body drag, we conducted flight testing to provide a relationship between pitch angle and the freestream velocity, assumed to be the Aqua-Quad cruise speed. While this side-stepped a drag model, a theoretical lift model was still needed to estimate the thrust needed for level flight. The thrust required for cruise flight is illustrated in Figure 49 and can be calculated as follows:

$$Thrust = \frac{(Weight + Lift)}{(\cos\alpha)} \tag{32}$$

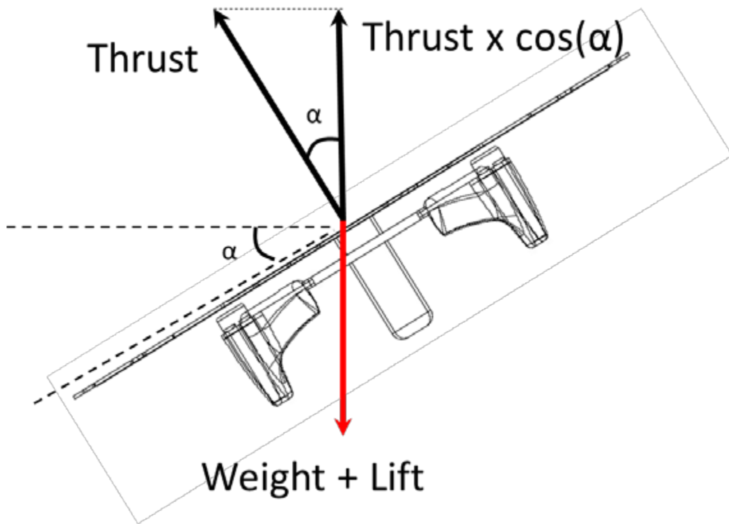

Figure 49. Thrust Required in Cruise

The solar array of the Aqua-Quad generates significant lifting force during cruise flight, albeit in the downward direction, the opposite of the normal convention. Flat Plate Airfoil theory [17] and Newtonian sine squared law [22] were examined to develop an appropriate model for this aerodynamic force. It was postulated that the former would overpredict lift while the latter would underpredict lift. As a result a hybrid lift model was developed by modifying the Newtonian Lift theory as shown in Equation (33). The resulting lift coefficient curves produced by the three lift models are illustrated in Figure 50. A correction for aspect ratio was applied to the Flat Plate theory by modeling the cruciform-shaped solar array as two rectangular airfoils, one with a long span and one with a short span. Flight testing was conducted to evaluate the appropriateness of these models and is discussed in the next section.

$$Aqua - Quad\ Model : C_L = 2\sin\alpha \tag{33}$$

$$Flat\ Plate\ Theory: C_L = \frac{2\pi \sin\alpha}{1+2/AR} \tag{34}$$

$$Newtonian\ Theory: C_L = 2\sin^2\alpha \tag{35}$$

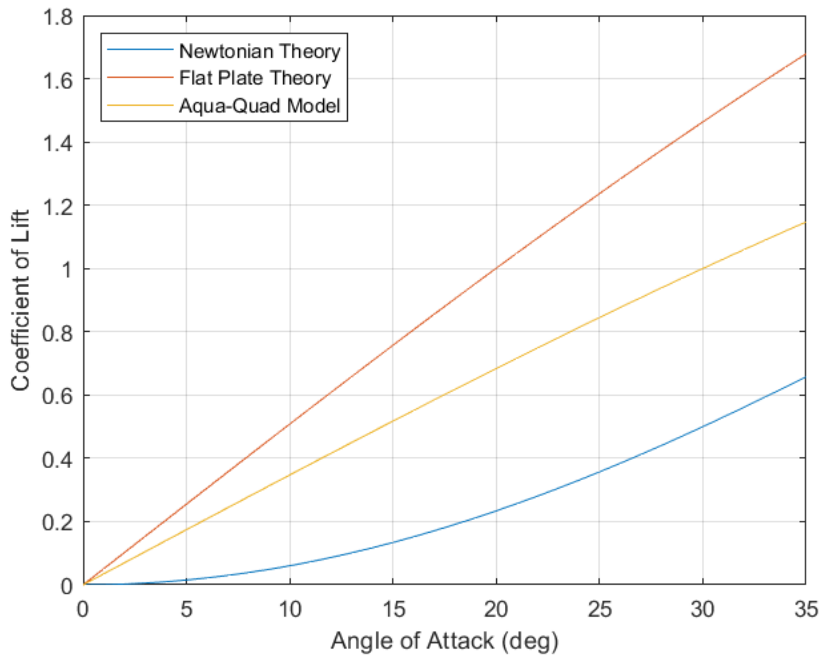

Figure 50. Coefficient of Lift for Different Models

The lift force predicted by Equation (33) is plotted in Figure 51 based on empirical values of cruise speed and pitch angles obtained from a test flight of a 0.8 kg scale Aqua-Quad model. At low speeds and low pitch angles, the lift generated is negligible, especially compared to the 7.8N weight of the drone. At the higher cruise speeds, however, the theoretical lift force would almost equal the drone weight. The high pitch angles associated with high speeds multiply the impact on the required thrust. As power is exponentially related to thrust, the "negative lift" effect is a significant driver of the power required to attain higher cruise speeds.

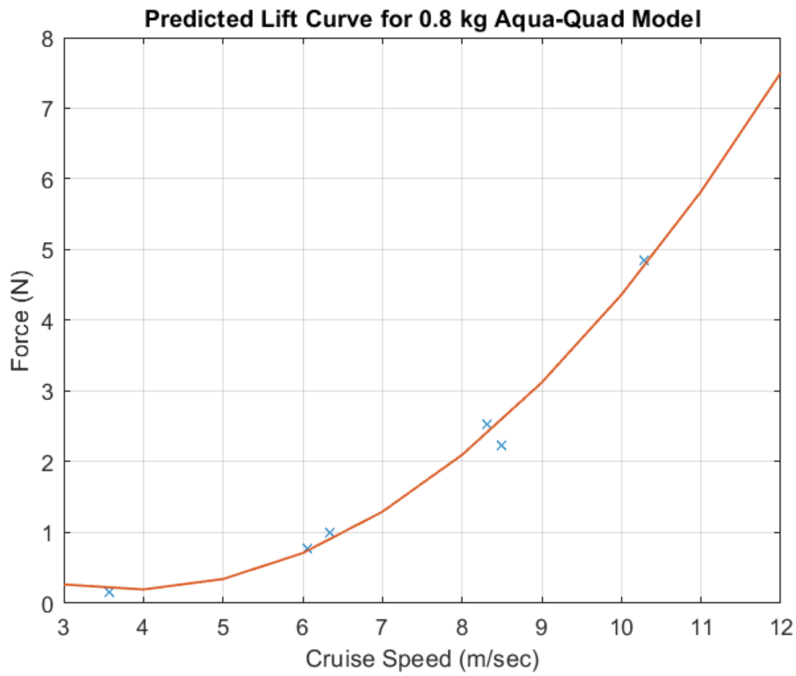

Figure 51. Predicted Lift for Scale Model Aqua-Quad

C. FLIGHT TESTS

Flight tests conducted with the scale model Aqua-Quad provided data on power consumption for a range of cruise speeds. The drones were flown outbound at 35 meters AGL on a 300-meter straight leg and then turned around and flown inbound on the same straight leg back to the launch point, as illustrated by the overview shown in Figure 52. Besides collecting power data to validate the momentum-theory power model, the flight tests collected pitch angle data. The pitch data was correlated with cruise speed and used as an essential input to the cruise power model.

Figure 52. Bird’s-eye View of Cruise Flight Profile at Camp Roberts.

The Aqua-Quad pitch angle is measured by the built-in attitude system and its ground speed is measured using GPS readings. Both parameters are captured in the autopilot telemetry data. The relationship between ground speed and pitch angle can be seen in Figure 53, which plots the average pitch angle recorded during steady cruise at different commanded ground speeds of 5, 7.5, and 10 m/s. The plot includes the error bars based on the standard deviation of the pitch angle during the constant commanded ground speed profiles. Error bars based on the standard deviation of the ground speed and pitch angles during these profiles are also included. The measurement scatter for these readings was relatively minor and the data shows that higher groundspeeds require larger pitch angles.

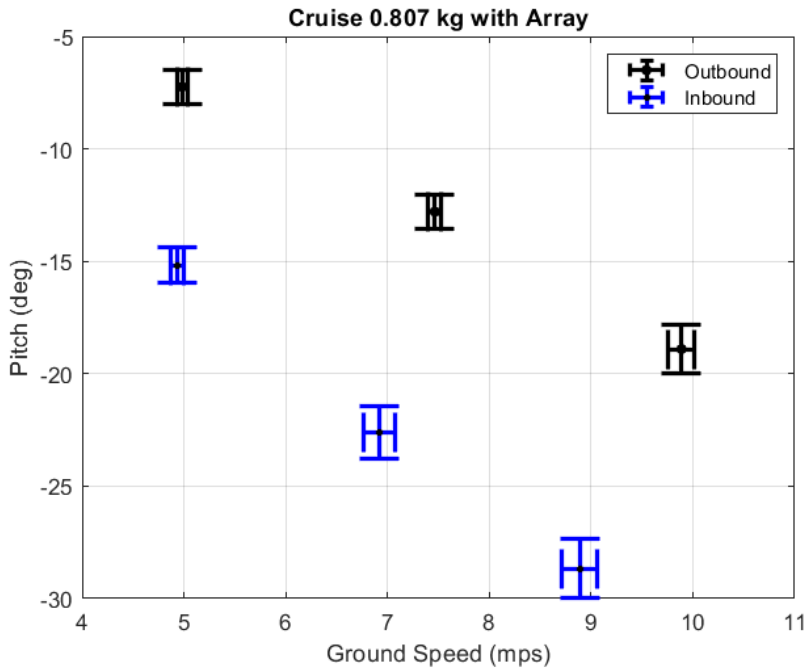

Figure 53. Pitch Angles for Different Commanded Ground Speeds

The drone pitch angle actually varies with the airspeed of the airflow it experiences, termed true airspeed, which differs from the GPS ground speed due to winds. As such, even though the outbound and inbound legs were flown at the same ground speeds, the measured pitch angles differ due to different wind conditions affecting the true airspeeds. Flying into the wind, the drone needed a higher true airspeed to fly at the commanded groundspeed. The higher true airspeed necessitates a higher pitch angle. Using meteorological data of the wind speed during the flight tests, the ground speeds were corrected to true airspeeds as shown in Figure 54. The outbound legs were assessed to experience a tailwind of 1.4 m/s (3 mph) and the reciprocal inbound legs experienced a headwind of 1.4 m/s (3 mph). The speed error bars were also adjusted to account for the wind variability during the test flights. This wind variability was assessed to be the wind gust speed recorded by the weather station, which was 0.9 m/s (2 mph). The correction for true airspeed reveals a linear relationship with the pitch angle.

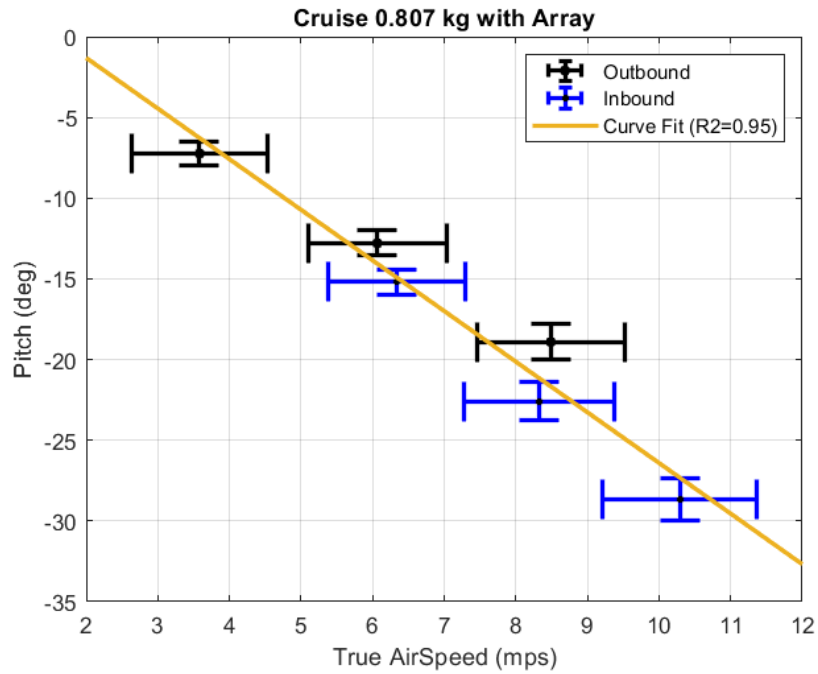

Figure 54. Pitch Angles for Different True Air Speeds

Using the pitch values to approximate the airflow AOA, Equations (27), (31), and (32) can be used to predict the power required for a given platform weight at different cruise speeds. With the assumption of a 0.4 efficiency factor, the predicted power curves for two different platform weights are shown in Figure 55 and Figure 56. Both power curves are compared against the collected experimental power data. The plotted experimental data is the mean power during the steady segments of the constant commanded speed profiles. The standard deviation of the power during these segments are also plotted as error bars, showing greater scatter at high speeds. The overall curve fit of the predicted power model curve to the experimental data reflects the appropriateness of both the momentum theory model and the lift model.

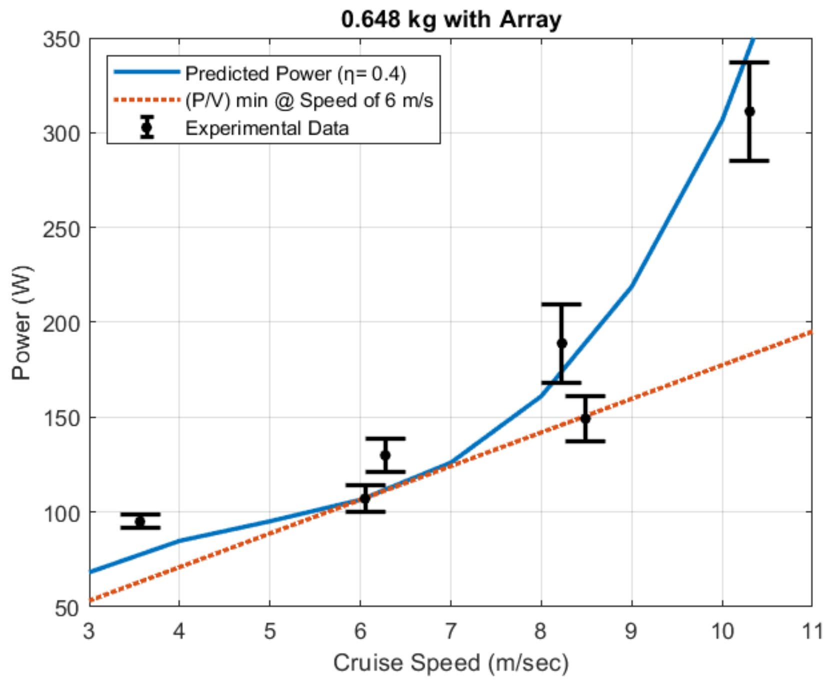

Figure 55. Cruise Power for 0.648 kg Aqua-Quad Model

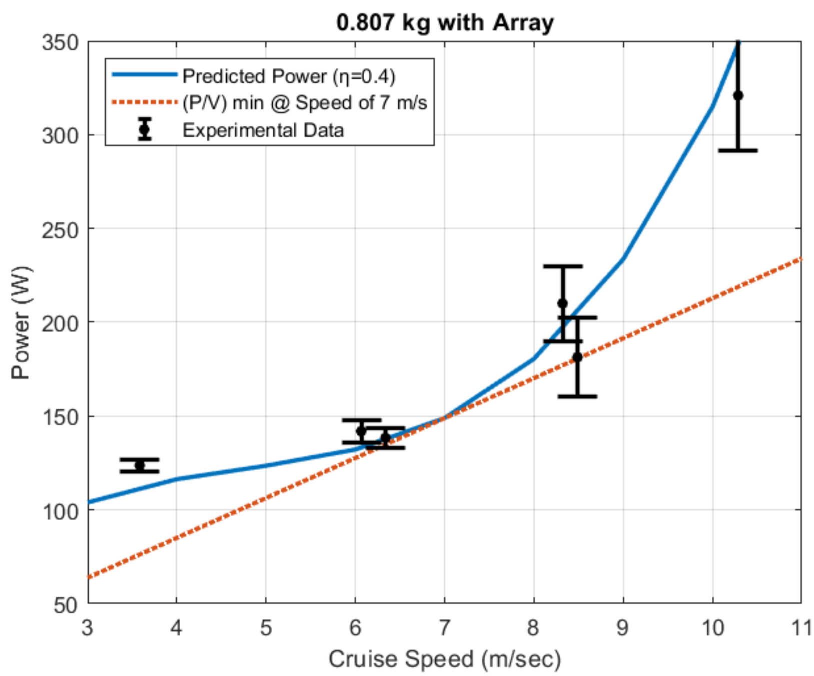

Figure 56. Cruise Power for 0.807 kg Aqua-Quad Model

1. Lift Model Assessment

The appropriateness of the chosen Aqua-Quad lift model was further evaluated by applying different lift models to the momentum theory power model. Figure 57 illustrates the different power curves obtained when using the three lift models discussed in the previous section, namely Flat Plate Airfoil theory, Newtonian theory, and a unique model derived for this paper. In addition, a power curve based on no lift was also plotted. In this case, the only factor driving the required thrust was the weight of the drone. Without a lift model, the power prediction significantly underpredicted the experimental power. On the other hand, the chosen lift model was a closer fit to the experimental data than the Flat Plate Airfoil and Newtonian theories.

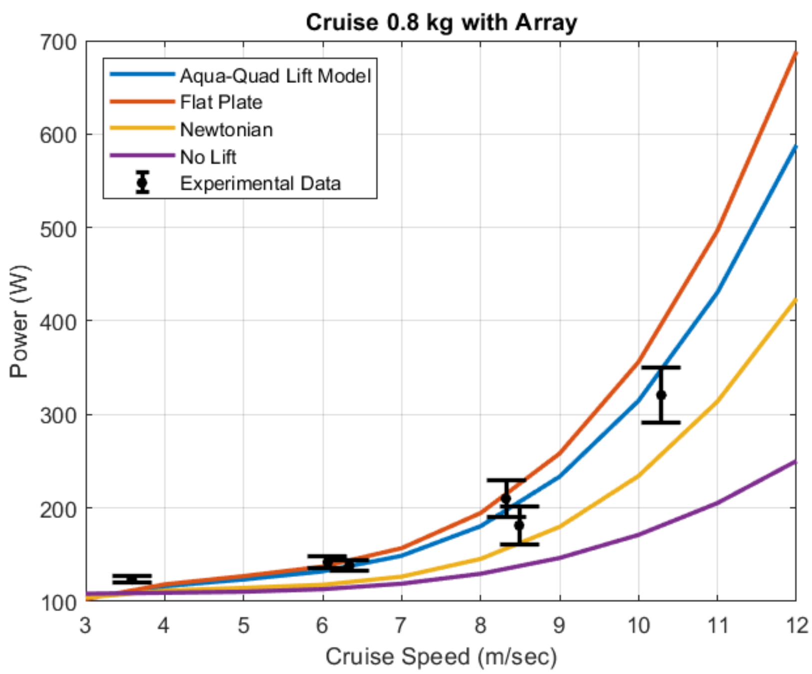

Figure 57. Comparison of Lift Models for Cruise Power Prediction

2. Drag Assessment

Besides validating the theoretical power models, the flight test data was also used to estimate the drag of the Aqua-Quad in cruise flight. Given the drone pitch angles, the known drone weight and estimated lift force, the thrust required for level flight can be calculated with Equation (32). Given the estimate for thrust, the drag force acting on the drone can be determined by the balance of force shown in Figure 58 and the following equation.

$$Drag = Thrust \times \sin(\alpha) \tag{36}$$

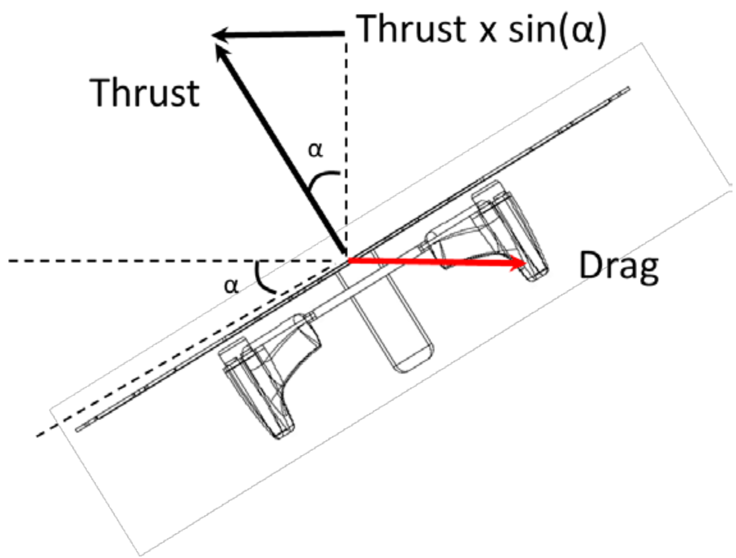

Figure 58. Force Balance during Cruise between Drag and Thrust

The drag estimates at different speeds for the scale model configuration without the solar array are shown in Table 2 and Figure 59. For this configuration without the solar array, it was assumed that there was negligible lift. Consequently, the calculation of thrust was based purely on the weight of the drone and the pitch angle, which was obtained from the flight test telemetry. With this thrust estimate, the drag is derived through simple geometry using Equation (36). Of note, the cruises speeds were derived by correcting the GPS ground speeds recorded with wind estimates from meteorological data. It was observed that drag was more sensitive than lift to variations in the wind correction.

Table 2. Estimated Thrust and Drag from Flight Test Data of 0.6 kg Scale Model Aqua-Quad (Without Solar Array)

True Air Speed (m/s)	3.6	6.07	6.08	8.60	8.61	11.25
Pitch Angle (deg)	7.3	14.0	15.3	21.4	24.0	27.8
Thrust Estimate (N)	5.93	6.07	6.10	6.32	6.44	6.65
Drag Estimate (N)	0.75	1.47	1.61	2.31	2.62	3.1

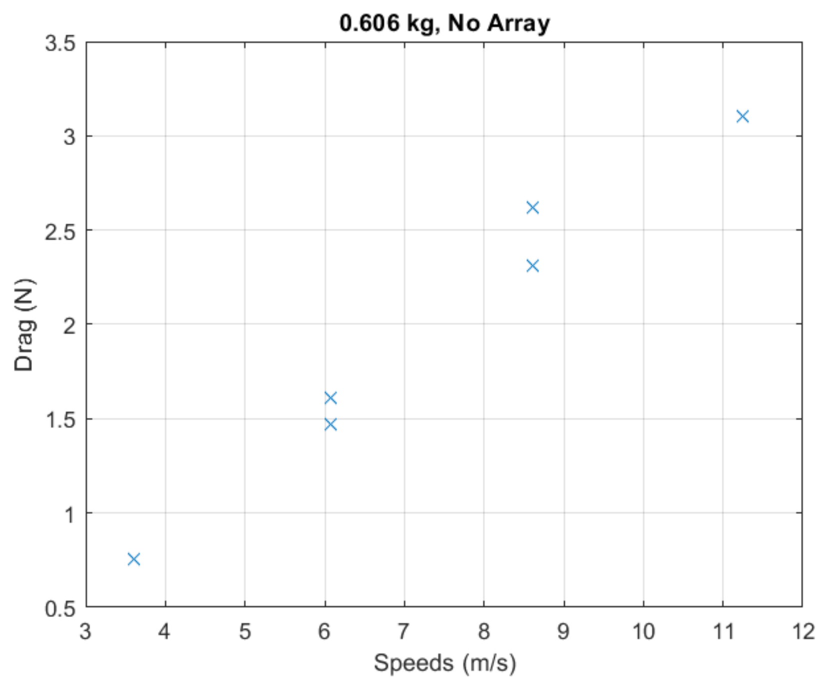

Figure 59. Drag Estimate Based on Experimental Data for 0.6 kg Model (Without Solar Array)

The quadrotor drag in cruise flight is a result of the four propellers and the drone body structures, which include the avionics bay and motor arms. “Rotor drag” from the four propellers is the primary drag source. Illustrated in Figure 60, rotor drag is the force “H” exerted by the rotor opposite the direction of flight.

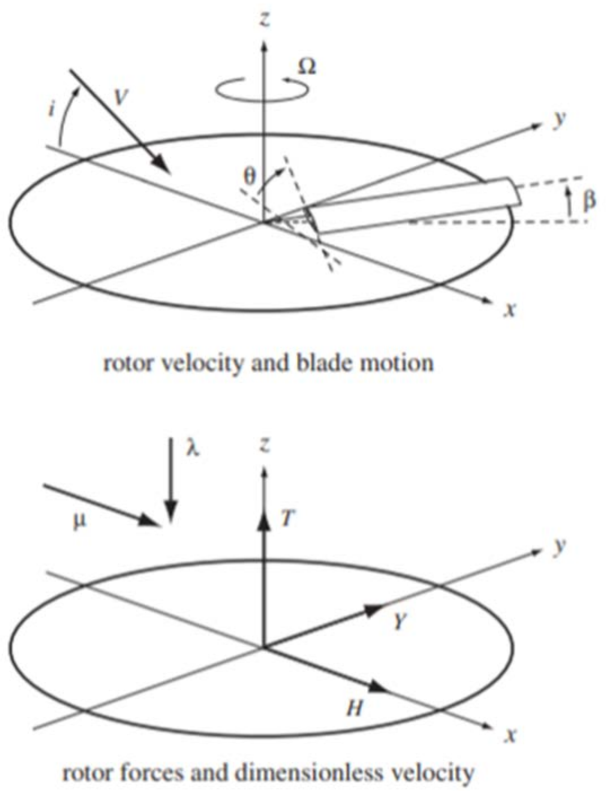

Figure 60. Rotor Forces in Cruise. Source: [19].

Johnson describes the rotor drag force (H) with the following equations [19].

$$\begin{aligned} H &= C_H \rho A(\Omega R)^2 \\ C_H &= C_{Ho} + C_{Hi} \\ C_{Ho} &= \frac{\sigma C_{do}}{4}\mu \\ C_{Hi} &= f(\mu, \sigma) \end{aligned} \tag{37}$$

The rotor drag force (H) is a function of density (ρ), rotor area (A), rotation rate (Ω), rotor length (R), and rotor drag coefficient (C_H). The rotor drag coefficient has a profile drag component (C_{Ho}) and an induced drag component (C_{Hi}). The induced drag component is a factor of blade pitch angles while the profile drag component is related to the average section drag coefficient of the rotor disk (C_{do}). Both components are also functions of rotor solidity (σ) and rotor advance ratio (μ), which are defined as follows in Equation (38).

$$\sigma = \frac{A_{blade}}{A_{rotor}} \qquad (38)$$
$$\mu = \frac{V \cos i}{\Omega R}$$

Based on Johnson's theoretical model [19], rotor drag increases with the freestream velocity (V), which is equivalent to cruise speed. Based on this theoretical understanding of rotor drag, a linear curve fit was developed based on the experimental estimates of drag for the scale model without the solar array. This relationship is shown in Equation (39) and predicts the scale model rotor drag at different airspeeds.

$$Drag\ (N) = 0.31732 \times Speed\ (mps) - 0.36011 \qquad (39)$$

The drag estimates at different speeds for the scale model configuration with the solar array are shown in Table 3 and Figure 61. Based on the "negative lift model," the addition of the solar array significantly increases drag, which now increases more exponentially with speed. Using Equation (39), we can calculate the rotor drag and subtract it from the total drag estimate to crudely determine the drag contribution of the solar array. These estimates are subsequently compared with CFD estimates in this paper.

Table 3. Estimated Lift, Thrust, and Drag from Flight Test Data of 0.8 kg Scale Model Aqua-Quad

True Air Speed (m/s)	3.6	6.1	6.3	8.3	8.5	10.3	Field Data
Pitch Angle (deg)	7.2	12.8	15.2	22.6	18.9	28.7	Field Data
Lift (N)	0.2	0.8	1.0	2.5	2.2	4.9	Lift Model
Thrust (N)	8.1	8.9	9.2	11.2	10.7	14.5	Force Balance
Total Drag (N)	1.0	2.0	2.4	4.3	3.5	7.0	Force Balance
Rotor Drag (N)	0.8	1.6	1.7	2.3	2.3	2.9	Empirical Fit
Solar Array Drag (N)	0.2	0.4	0.8	2.1	1.1	4.1	Total Drag – Rotor Drag

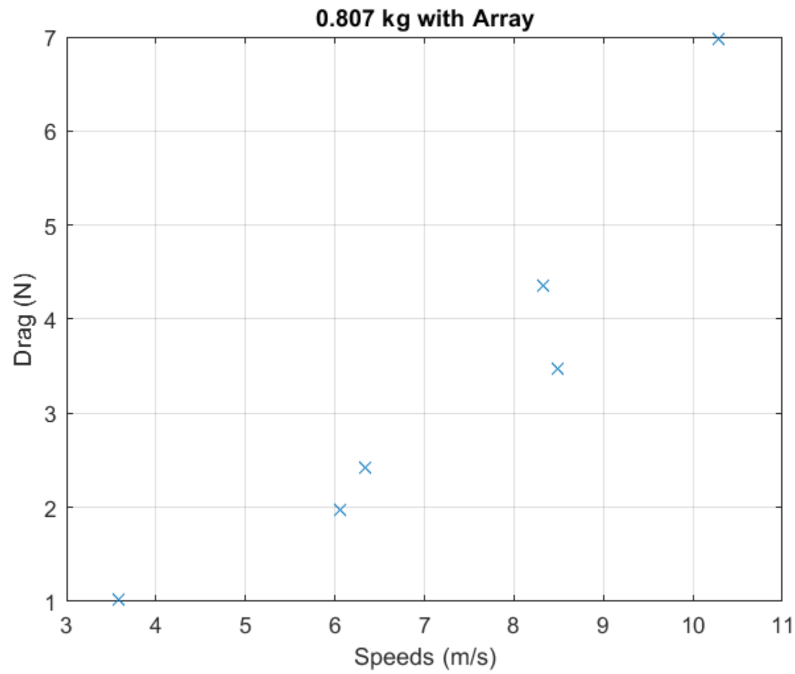

Figure 61. Drag Estimate Based on Experimental Data for 0.8 kg Model (With Solar Array)

D. CFD

CFD was conducted to complement the estimation of lift and drag characteristics from theory and empirical flight test. The CFD was conducted in the same fashion as for the vertical flight CFD. A simplified Aqua-Quad model, comprising just the solar array and frame, and a more detailed model were simulated in turn. While the more detailed model provided higher fidelity, it still did not model propeller effects. Nonetheless, the solar array and other airframe structures are significant contributors to the Aqua-Quad's aerodynamic performance and the CFD analysis was thus valuable. Overall, the cruise lift and drag predictions by CFD were reasonably close to theory and experiment, supporting the aerodynamic assumptions used in the overarching power model.

1. Simplified Aqua-Quad CFD

The simplified Aqua-Quad model only comprises the solar array and blade guards. The solar array acts primarily like a flat plate to generate lift, albeit in the downward direction. CFD was conducted for various freestream flows that mirrored the experimental test flight conditions in terms of cruise speed and AOA. An example of the CFD simulated flow field for one of these conditions is shown in Figure 62. The CFD simulation shows flow separation on the lower side of the solar array's sharp leading edge. While the flow reattaches downstream, these pockets of low pressure create significant pressure drag. As shown in Figure 63, The CFD also shows significant flow separation and regions of low pressure behind the "wings" of the cruciform-shaped solar array.

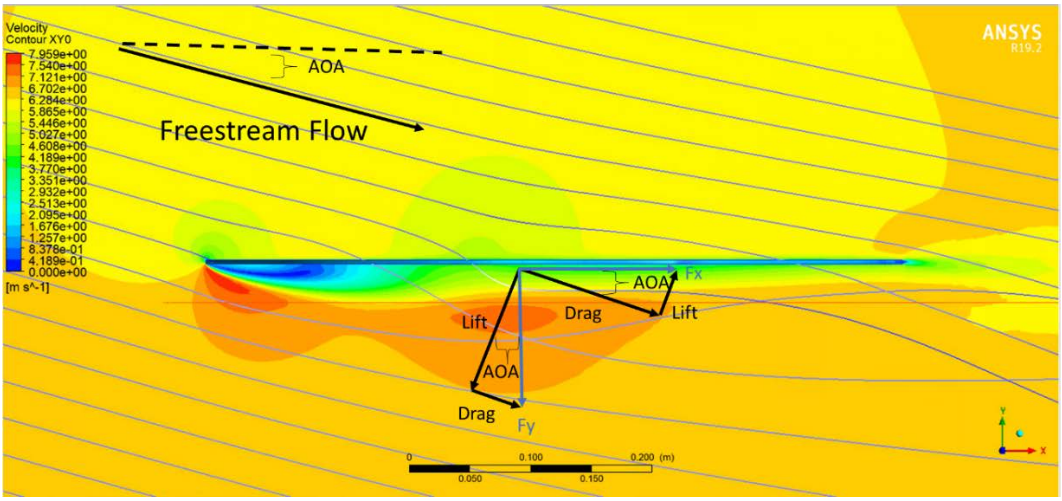

Figure 62. Side Profile of the CFD-simulated Velocity Field of the Simplified Aqua-Quad CFD in Cruise

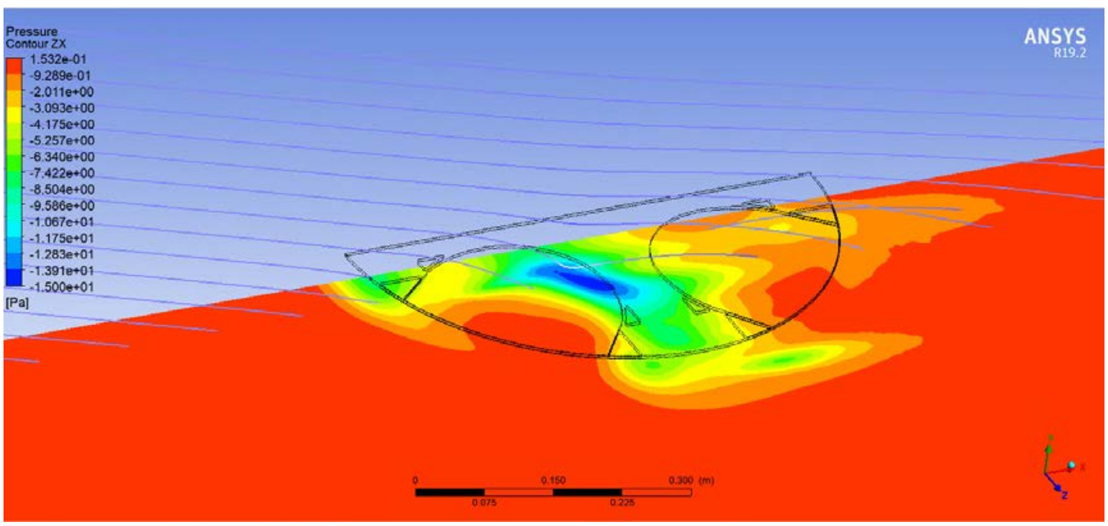

Figure 63. Overhead View of the CFD-simulated Pressure Field of the Simplified Aqua-Quad CFD in Cruise

While pressure forces are dominant for the range of cruise speeds and Reynolds numbers simulated, the viscous drag effects were larger in the horizontal cruise cases compared to the vertical climb case. This was due to the increased tangential flow along the upper and lower solar array surfaces. The CFD simulation was able to roughly model the development of boundary layers along surfaces as shown in Figure 64. The amount of shear associated with these boundary layers increased the viscous contribution to overall drag. On average, the magnitude of the viscous forces was 2% of the pressure forces, an increase from an average of 0.5% in the vertical climb cases.

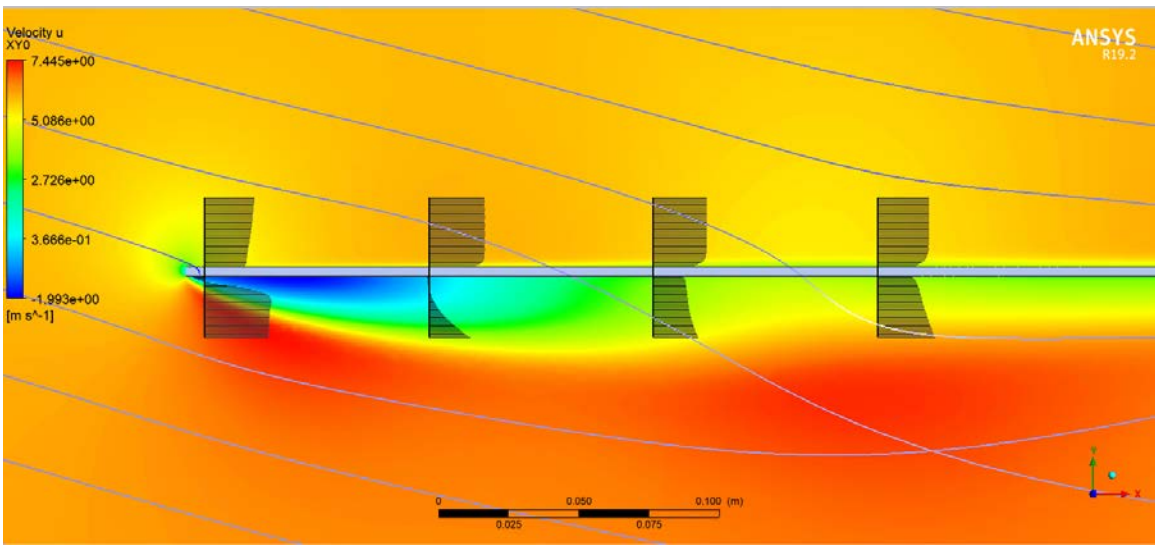

Figure 64. CFD-simulated Flow along the Solar Array in Cruise

Overall, the CFD lift estimates were larger in magnitude than the lift estimates derived from field testing as shown in Table 4. The results also matched better at higher speeds and high AOA. The relative closeness in results, which differ by an average of 23%, supports the validity of the model used to calculate the “negative lift” generated by the solar array in cruise flight. The difference in results can be attributed to the wind speed approximations used to estimate the lift from experiment as well as the lack of a propeller model in the CFD.

Table 4. Comparison of Array Lift from Simplified CFD and Experiment

True Air Speed (m/s)	3.6	6.1	6.3	8.3	8.5	10.3
Pitch Angle (deg)	7.2	12.8	15.2	22.6	18.9	28.7
Experiment (N)	-0.154	-0.777	-1.006	-2.542	-2.231	-4.852
CFD (N)	-0.224	-1.005	-1.241	-2.973	-2.660	-5.292
Difference	45%	29%	23%	17%	19%	9%

The drag estimates of the solar array using CFD and field testing are shown in Table 5. Like the lift results, the drag results matched better at higher speeds and high AOA. This could be due to greater shielding effect of the array at high AOA. As a result, the drag characteristic of the Aqua-Quad simplifies to a flat plate and most of the drag is pressure drag. While the fidelity is limited given the significant modelling assumptions, the results are still indicative of the actual drag profile of the Aqua-Quad and demonstrate that CFD can be a useful tool to refine the design to reduce drag. Moreover, the relative closeness in results, which differ by an average of 24%, supports the appropriateness of the aerodynamic assumptions made in the power model.

Table 5. Comparison of Array Drag from Simplified CFD and Experiment

True Air Speed (m/s)	3.6	6.1	6.3	8.3	8.5	10.3
Pitch Angle (deg)	7.2	12.8	15.2	22.6	18.9	28.7
Experiment (N)	0.249	0.411	0.769	2.073	1.140	4.074
CFD (N)	0.095	0.422	0.552	1.601	1.288	3.425
Difference	62%	-3%	28%	23%	-13%	16%

2. Detailed Aqua-Quad CFD

The same detailed Aqua-Quad CFD model used for estimating drag for vertical flight was used for cruise flight lift and drag estimates. In addition to the solar array, this model incorporated the main avionics hub and supporting structures, such as the pylons and mounts required to hold the motors and propellers. However, coarser meshes were employed for the CFD simulation of all the various cruise conditions, primarily due to computational time constraints. Overall, the CFD lift and drag estimates matched the experimental estimates reasonably well. Compared to the simplified CFD, the detailed CFD results had lower lift and higher drag. In cruise flight conditions, the additional structures in the Aqua-Quad model interrupt the airflow on the underside of the solar array as shown in Figure 65 and Figure 66.

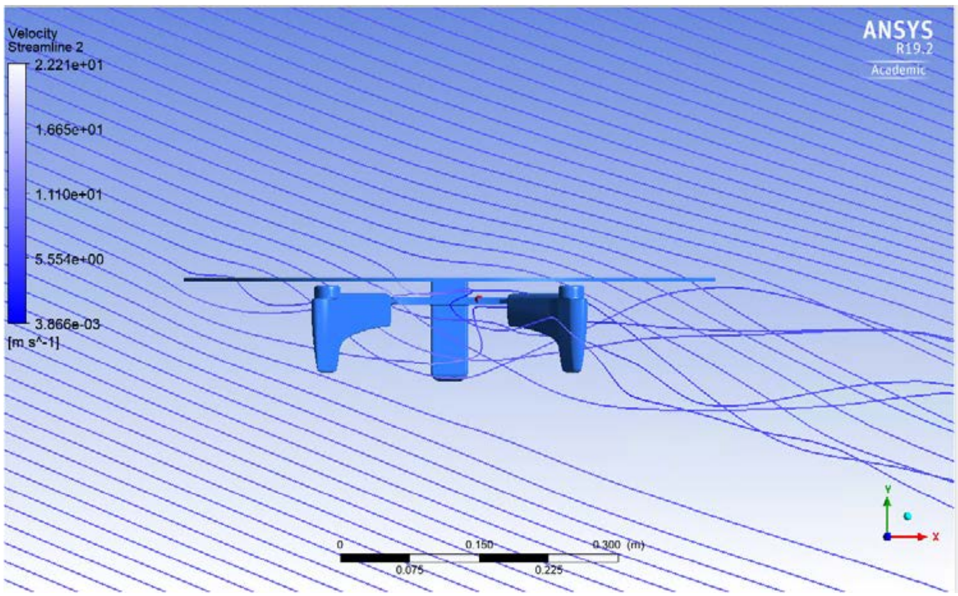

Figure 65. Side View of CFD-simulated Streamlines along the Detailed Aqua-Quad in Cruise

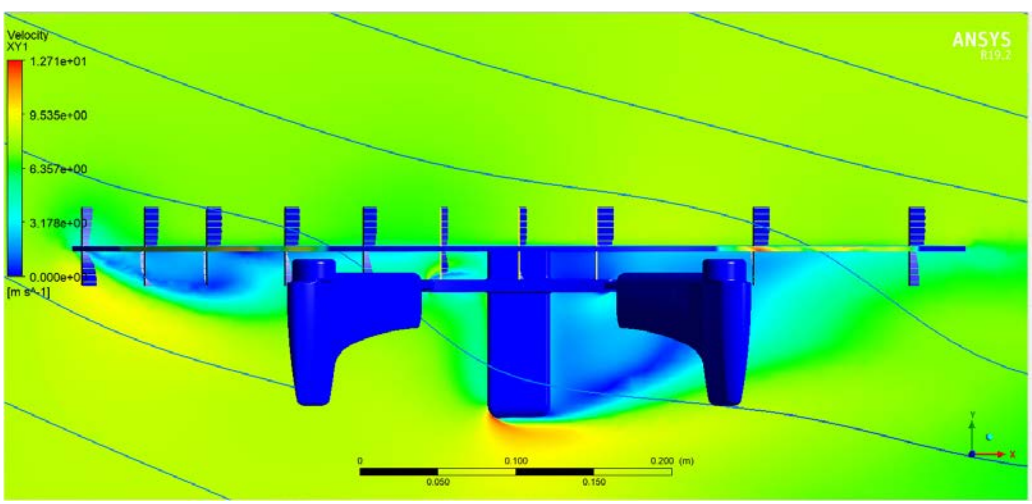

Figure 66. Side View of the CFD-simulated Velocity Field around the Detailed Aqua-Quad in Cruise

As shown in Table 6, the lift estimated from the detailed CFD is relatively close to the experimental estimates, differing by an average of 8%, a closer match than for the simplified CFD. In addition, the detailed CFD lift results are smaller than the simplified CFD estimates. The additional structures included in the detailed model disrupt the airflow on the underside, causing an increase in pressure on the underside, thus offsetting the “negative lift” of the solar array. Overall, the agreement in results supports the accuracy of the lift model used to predict power.

Table 6. Comparison of Lift from Detailed CFD and Experiment

True Air Speed (m/s)	3.6	6.1	6.3	8.3	8.5	10.3
Pitch Angle (deg)	7.2	12.8	15.2	22.6	18.9	28.7
Experiment (N)	-0.154	-0.777	-1.006	-2.542	-2.231	-4.852
CFD (N)	-0.129	-1.742	-0.975	-2.380	-2.146	-4.144
Difference	-16%	-5%	-3%	-6%	-4%	-15%

As shown in Table 7, the detailed CFD drag estimates are reasonably close to the experimental estimates, differing by an average of 20%. In the cases where the difference is greater than 20%, it is suspected that the wind estimates to correct the experimental ground speeds to true airspeeds were particularly inaccurate. The speeds for these cases did not quite match the expected speeds based on the measured pitch angles and the pitch-speed model that was discussed earlier. As the value of drag depends strongly on the sine of the pitch angle, the drag value is more sensitive than the lift value to changes in pitch angle at the relatively small pitch angles associated with cruise (~10-30 degrees). As a result, the experimental errors in cruise speed and pitch angle have a larger effect on the drag estimates than the lift estimates.

Table 7. Comparison of Drag from Detailed CFD and Experiment

True Air Speed (m/s)	3.6	6.1	6.3	8.3	8.5	10.3
Pitch Angle (deg)	7.2	12.8	15.2	22.6	18.9	28.7
Experiment (N)	0.249	0.411	0.769	2.073	1.140	4.074
CFD (N)	0.191	0.668	0.853	2.091	1.820	4.144
Difference	23%	-63%	-11%	-1%	-60%	-2%

Overall, the drag results from the detailed CFD are greater than from the simplified CFD due to the greater wetted area leading to increased skin friction drag. Nevertheless, pressure drag still dominates. Despite many rough assumptions, the relative agreement in results supports the overall aerodynamic modeling that went into the power prediction model. In addition, the CFD modeling set a reference benchmark for future drag analysis on small quadrotors.

E. PREDICTION FOR FULL-SCALE AQUA-QUAD

Assuming similar aerodynamic characteristics, the scale-model pitch-speed behavior should apply to the full-scale model. By applying curve fits to the pitch-speed data gathered during the scale-model test flights, the following empirical relationship was developed.

$$Pitch\ Angle\ (\alpha) = -2.7872 \times Speed + 3.3231 \tag{40}$$

The curve fits to the empirical data and the curve of equation (40) are shown in Figure 67. Equation (40) is used to determine the pitch angles required for the full-scale Aqua-Quad cruise at various airspeeds, which is then used as an input to calculate the power required.

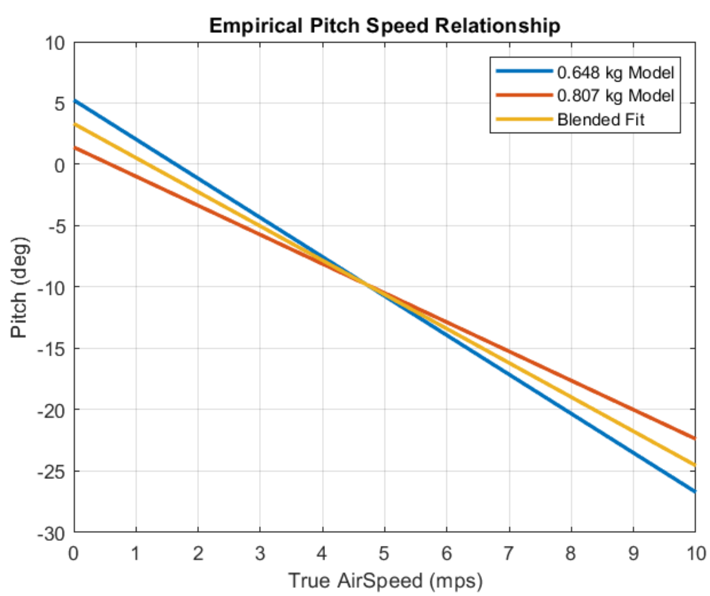

Figure 67. Empirical Relationship of Pitch and Speed

To calculate the cruise power using the models developed, it is also critical to first determine the "negative lift" force encountered by the full-scale model. Assuming that the scale model and full-scale Aqua-Quad share the same lift coefficient, the lift force only scales based on the increased surface size of the full-scale solar array. Given this assumption and the earlier assumption of an identical pitch-speed relationship, the cruise power for the full-scale model can be calculated and is shown in Figure 68. The speed for best range is 7 m/s with a power consumption of 670 W. If the efficiency factor can be improved from 0.4 to 0.5, the power curve will fall, as shown in Figure 69. While the best range speed remains at 7 m/s, the power consumption decreases to 540 W.

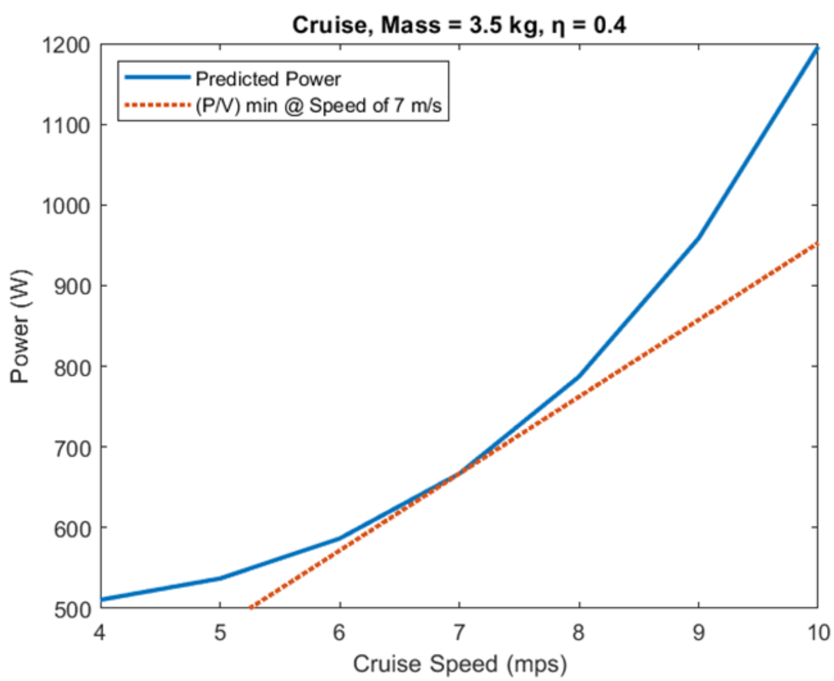

Figure 68. Cruise Power Required for Full-Scale Aqua-Quad (Efficiency Factor of 0.4)

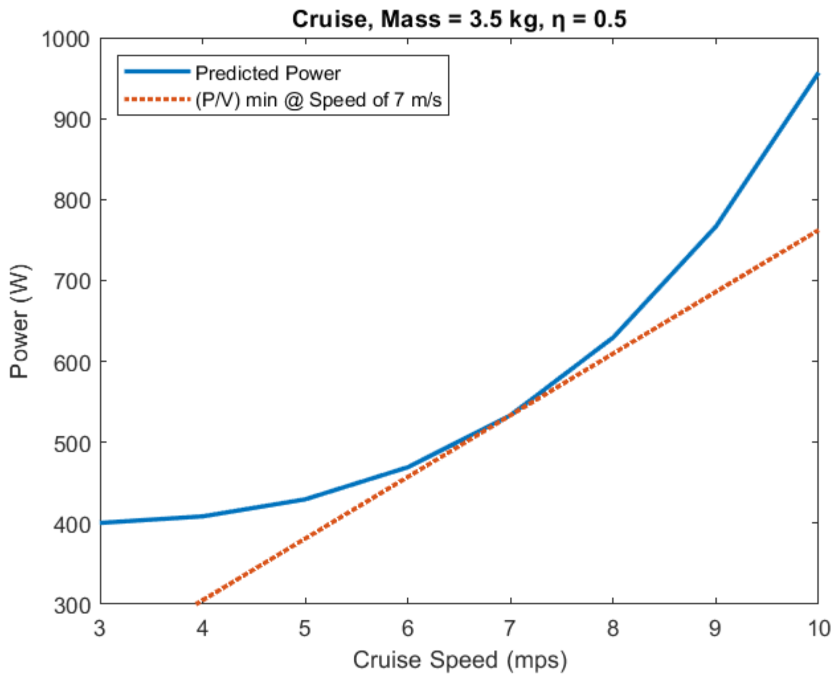

Figure 69. Cruise Power Required for Full-Scale Aqua-Quad (Efficiency Factor of 0.5)

THIS PAGE INTENTIONALLY LEFT BLANK

VII. CONCLUSION AND RECOMMENDATIONS

This section presents the power predictions for the full-scale Aqua-Quad during hovering, climb, descent, and cruise. This section also proposes recommendations and areas for future work.

A. POWER PREDICTIONS FOR FULL-SCALE AQUA-QUAD

The momentum theory power models developed in this thesis were validated with flight tests on a scale model of the Aqua-Quad. CFD was done in parallel to support the validity of the models used for drag and lift. The power models can be applied to the full-scale Aqua-Quad by scaling for weight and size. One parameter that will not scale exactly is the overall system efficiency. Larger propellers have slightly improved propulsive efficiency with lower disk loading. Hovering power experiments indicate a full-scale Aqua-Quad efficiency of 50% as shown in Chapter III. This is likely the maximum limit as the maximum efficiency seen in large helicopters is 50% [1]. As flight testing of the full-scale Aqua-Quad has been limited, an efficiency of 40% or an efficiency factor of 0.4 is conservatively assumed for climb and cruise. For descending flight, a lower efficiency value of 35% was used to account for the increased control losses when descending into the turbulent wake.

The climb power for the full-scale model calculated in Chapter IV is reproduced in Figure 70. The most efficient climb speed of 5 m/s occurs when $\frac{Power}{Speed}$ is at a minimum. This climb speed requires 1060 W of power and a 20-second climb to a nominal cruise altitude of 100 m AGL will consume 6 Wh of battery charge.

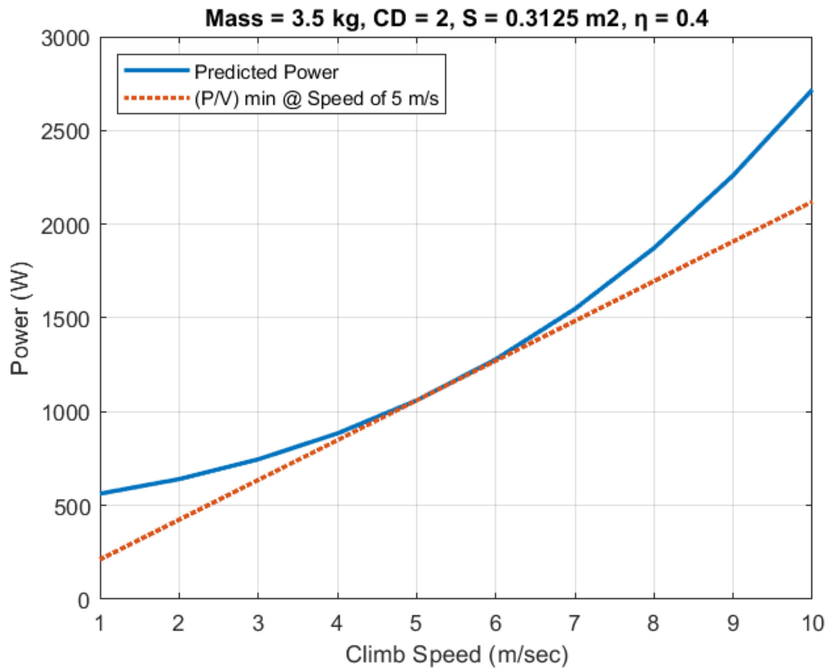

Figure 70. Climb Power Required for Aqua-Quad

The descent power required for the full-scale Aqua-Quad calculated in Chapter V is reproduced in Figure 71. Given stability concerns and the need to transition to touchdown at a gentle rate, a slow descent rate of 2 to 3 m/s can be expected, requiring 510 W of power. Descending from a nominal cruise altitude of 100 m AGL, this descent profile would draw 7 Wh from the battery.

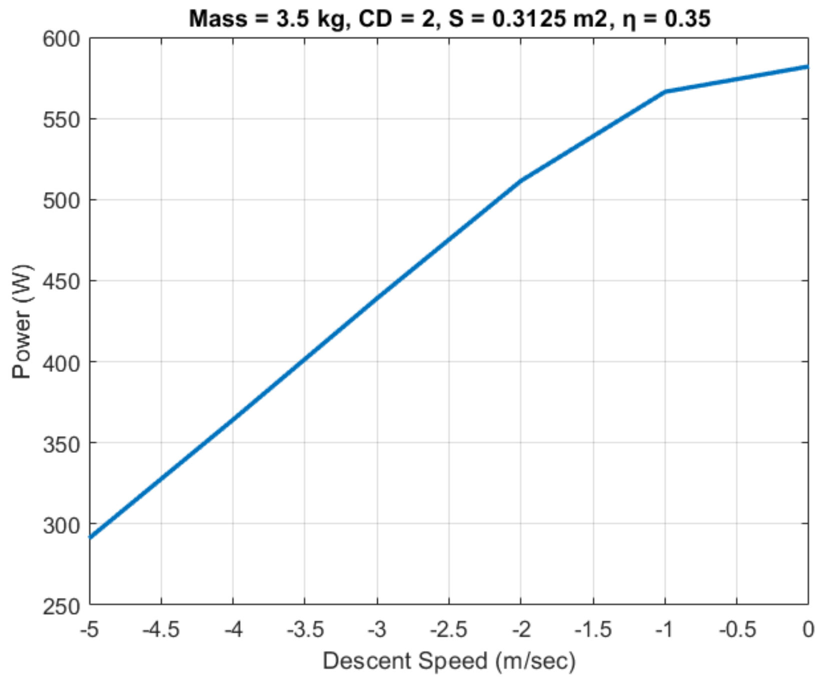

Figure 71. Descent Power Required for Aqua-Quad

The power required for Aqua-Quad cruise flight calculated in Chapter VI is reproduced in Figure 72. It is based on an efficiency of 40% and a design mass of 3.5 kg. The speed for best range is 7 m/s with a power consumption of 670 W.

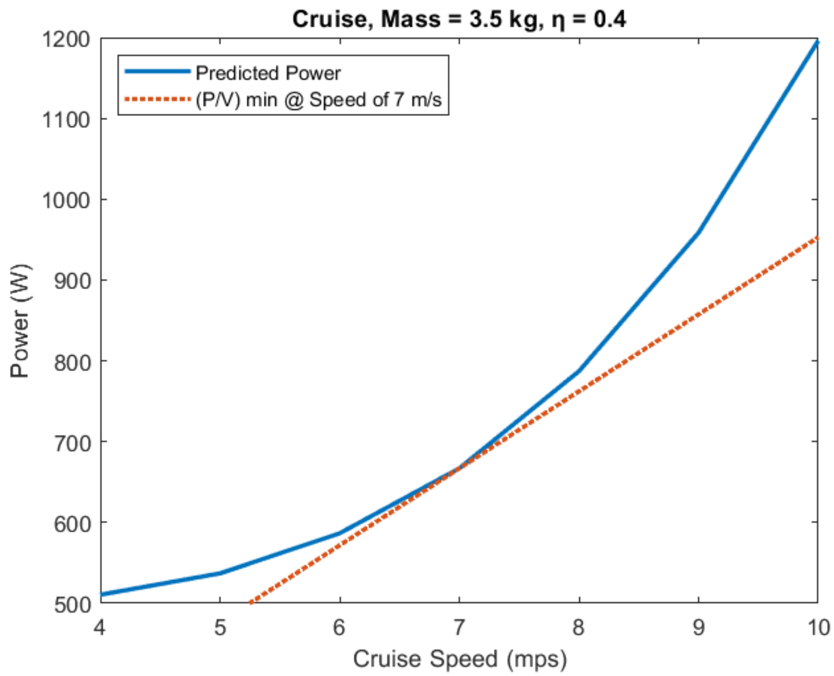

Figure 72. Cruise Power Required for Aqua-Quad

The models developed have determined the in-flight energy consumption of the Aqua-Quad for each primary flight phase of the envisaged operational concept. While the climb phase has the highest power demand of 1060 W, it also has the shortest duration as the nominal cruise altitude is only 100 m AGL. The battery is thus drained the most during the cruise phase. Based on a cruise energy consumption rate of 670 W and equipped with a 178 Wh battery, the drone would be able to fly for a duration of 15 minutes or a distance of 6.2 km, as depicted in the envisioned Aqua-Quad flight profile in Figure 73. If the Aqua-Quad power efficiency could be improved to 50% from 40%, the cruise energy consumption rate would decrease to 540 W and the range would increase to almost 8 km.

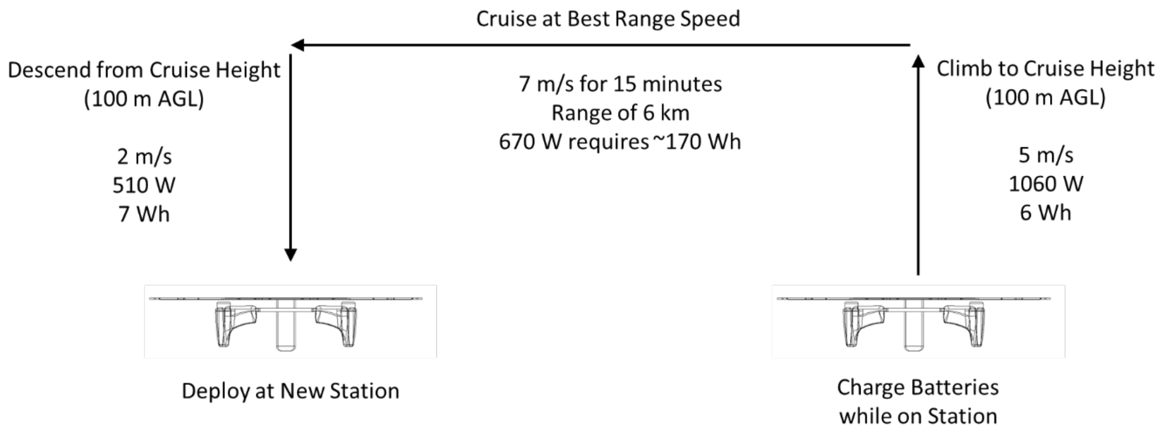

Figure 73. Power Demands during Aqua-Quad Flight Profile

B. NEW DESIGNS AND FUTURE WORK

Given the importance of keeping the platform cost-effective, there is limited scope to improve power efficiency by using higher performance components and materials. Power efficiency could be improved, however, by rearranging the solar array. In the current configuration, the solar array generates negative lift in cruise. If the solar array were realigned so that it was in line with the freestream flow at cruise, the negative angle of attack of the airflow would decrease. This would reduce the negative lift and induced drag. An example of such a design is Amazon's Prime Air Drone, which has flat lifting surfaces that align with airflow for the expected cruise orientation. Nonetheless, the impact of this change in inclination on solar power generation needs to be studied and there will be some tradeoffs to be made. A simpler design optimization could be to examine the difference in drag and lift when cruising with the solar array in an "x" orientation as opposed to a "+" orientation.

This thesis has revealed that the losses due to control efforts can be significant and more research could be conducted to determine how the autopilot could be tuned to reduce excessive control efforts while maintaining acceptable control and stability. Given that the mission profile of the Aqua-Quad does not require tight maneuvering or handling, the proportional–integral–derivative (PID) gains could perhaps be reduced and the demands for stability relaxed. The impact of wind is also significant, and overall system efficiency could be improved with the design of an autopilot and mission planning system that exploits the wind patterns.

For future work, the CFD analysis could be further improved by modeling the effect of the propellers as actuator disks. In vertical or cruise flight, propellers are likely to influence the pressure and velocity patterns of the airflow, both downstream and upstream of the drone body. The propeller effect might reduce the overall pressure drag or shift the pressure distribution. The propeller wake has swirl and will also interact with the blunt body wakes to create turbulent flow that is difficult to model in CFD to match physical behavior. The dynamic nature of the four rotating propellers also likely creates a highly unsteady flow. The use of CFD to fully characterize the aerodynamics of the Aqua-Quad is thus expected to be limited.

APPENDIX A. FLIGHT TEST DETAILS

A half-scale model of the Aqua-Quad, shown in Figure 74, was built and flown to gather data on the power expended for different flight profiles. A mock solar array, that could be detached from the scale model, was built. The model weighs 0.448 kg without a battery and without the mock solar array. Equipped with a four-cell LiPo battery, the prototype weighs 0.604 kg. The scale model uses Bolt 2207L 1660 KV motors paired with 7-in Gemfan propellers. For avionics, standard COTS parts were used for the autopilot, GPS, ECS, and radio control. To gather data on the different platform weights, lead weights were added to the drone. Each strip of lead weight was roughly 0.088 kg.

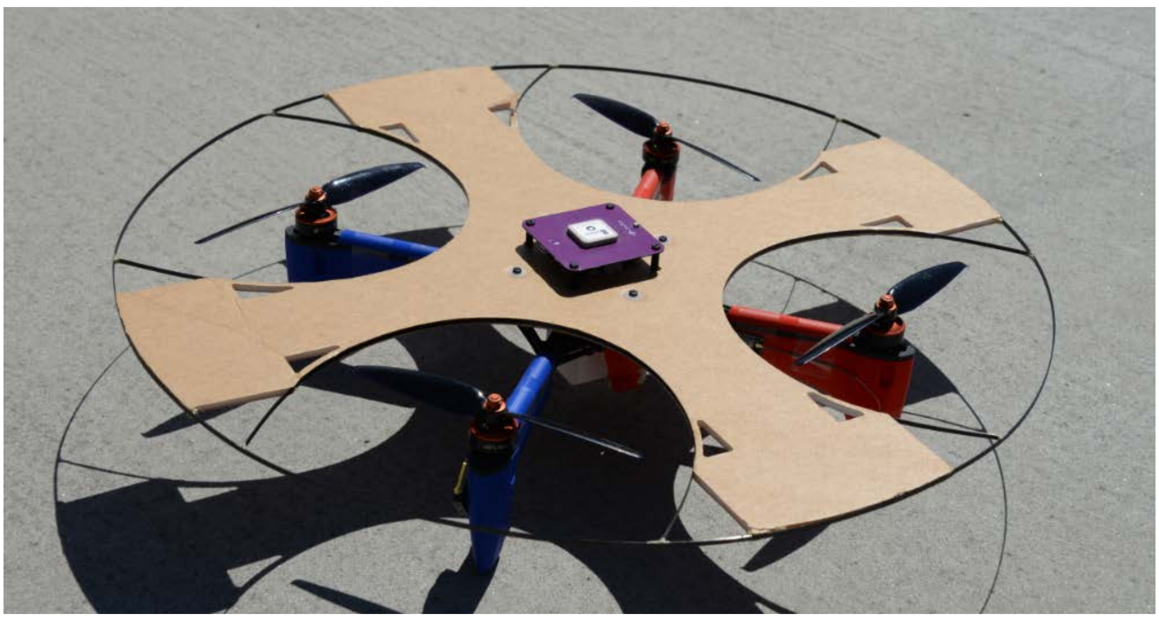

Figure 74. Scale Model of Aqua-Quad

The flights were conducted at two designated test sites at the Impossible City and Camp Roberts in Monterey County, California. Both sites provide a large flight area that was secure for operations. Importantly, the airspace was deconflicted to up to 400 ft AGL from manned aircraft. The larger airspace at Camp Roberts was particularly conducive for gathering large amounts of data for cruise flight, which required long straight legs over long distances. Located at an airstrip, the site also offered good line of sight of the drone even at distance. Lastly, it was useful that there was a weather monitoring station collocated at the airstrip, which provided accurate meteorology data, especially on winds. The locations of the two test sites are shown in Figure 75 and Figure 76, respectively. The elevation at the Impossible City site is around 85 m while the elevation at the Camp Roberts site is around 275 m. This difference in altitude affects air density. For accurate analysis, the air density needs to be calculated based on temperature and pressure readings.

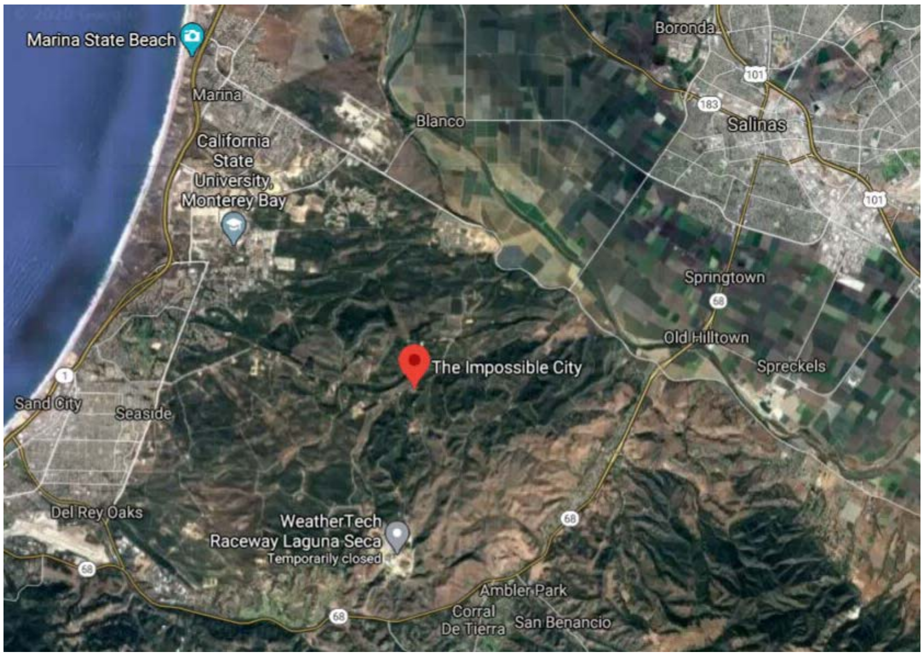

Figure 75. Impossible City Location

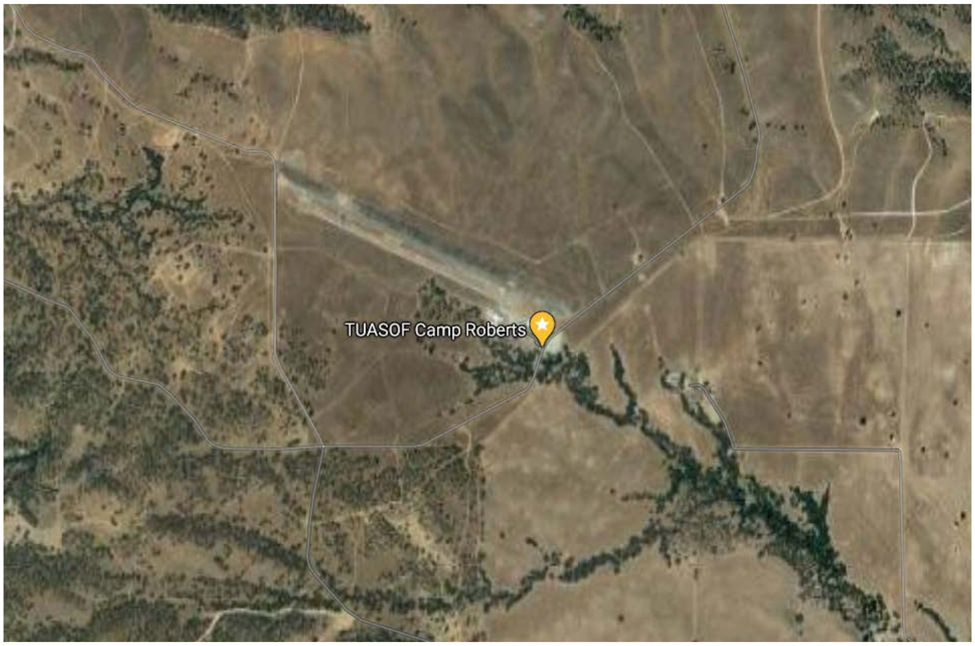

Figure 76. Camp Roberts Location

The drone autopilot telemetry data was saved on an onboard chip. It was downloaded post flight and the files were converted by the ArduPilot Mission Planner software to a Matlab-compatible format. Matlab was the primary software used to process and analyze the flight test data. An example of the parsing is shown in Figure 77.

```
load 00000020.BIN-171389.mat

%% GPS data set
GPStime=GPS(:,2);
GPStime=(GPStime-GPStime(1))/1000000;
alt=GPS(:,10);
speed=GPS(:,11);
lat=GPS(:,8);
long=GPS(:,9);
GPSclimb=GPS(:,13);

longdist=long*1855.3248*60;
longdist=longdist-longdist(1);
latdist=lat*1855.3248*60;
latdist=latdist-latdist(1);
distance=sqrt(longdist.^2+latdist.^2);

%% AHRS data set
AHRtime=AHR2(:,2);
AHRtime=(AHRtime-AHRtime(1))/1000000;
pitch=AHR2(:,4);
roll=AHR2(:,3);
yaw=AHR2(:,5);

%% Battery data set
battime=BAT(:,2);
battime=(battime-battime(1))/1000000;
volt=BAT(:,3);
curr=BAT(:,5);
power=volt.*curr; % calculate power

```

Figure 77. Parsing of Aqua-Quad Telemetry Data in MATLAB

The data was analyzed by first determining the key performance parameter. For instance, climb speed was the key performance parameter for the climb power model. The performance data was then screened to identify the segments of stabilized flight, where the drone was established at the desired cruise or vertical speed, and not dealing with transient accelerations. With these stable segments identified, additional telemetry data were extracted and correlated with the performance parameter. For instance, to determine the power required to maintain a set vertical speed, the voltage and current data fields were extracted from the telemetry at the stable segments. The data was processed by MATLAB to calculate the instantaneous power. An example of the resulting data sets is shown in Figure 78. The power over the relevant time segments was further analyzed to determine the average power required for the associated cruise speed. Given the noise and scatter of field data, this "data cleaning" process was critical.

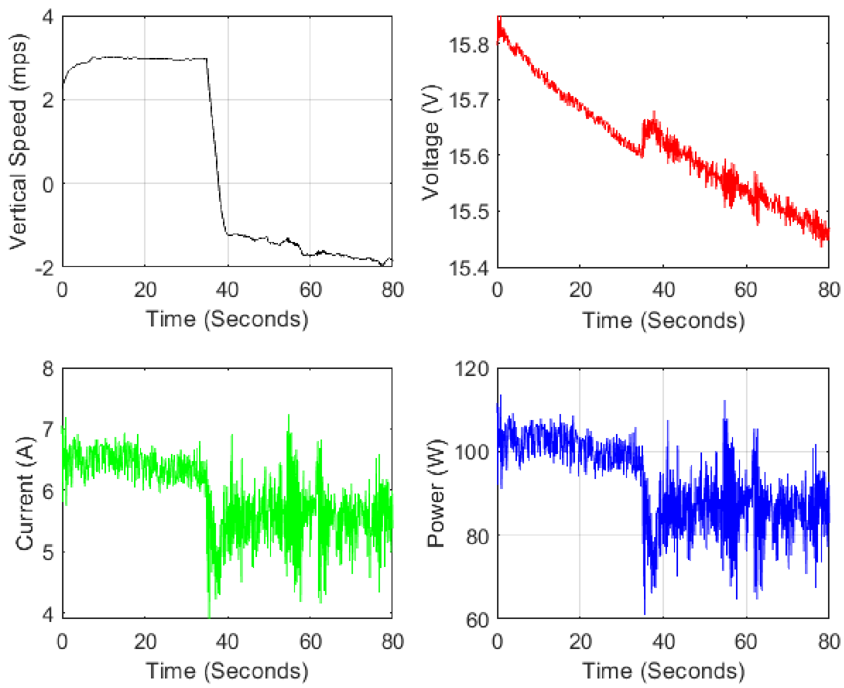

The telemetry data describes a flight profile with climb at 3 m/s, followed by descent at 2 m/s. Throughout the profile, the battery voltage decreases while the current changes as required to deliver the required power output.

Figure 78. Processed Flight Test Data

THIS PAGE INTENTIONALLY LEFT BLANK

APPENDIX B. MATLAB SCRIPTS

```
%% Hovering Power Prediction  Aqua-Quad
close all
clear all
clc


%% Constants
rho = 1.225;    % Air Density SL (kg/m3)
g=9.81;         % gravity m/s^2


%% Dimensions
dia = 0.356 ; % rotor diameter (m)
rotors = 4; % number of rotors
rotorA = rotors*pi*0.25*dia^2; %m^2
arrayA=0.3125; %m^2


%% Other Parameters
vc=0;   % climb speed = 0 for hovering


%% Power Estimation (n=0.4)
n=0.4;  % Efficiency


i=1;
for mass=[2.5:0.1:4];  %kg
weight=mass*g;          %N
thrust=weight;          %N
vh=sqrt(thrust/(2*rho*rotorA));
vi=vh*(-0.5*vc/vh+sqrt(0.25*((vc/vh)^2)+1));
power(i)=thrust.*(vc+vi)/n;
i=i+1;
end


%% Plot
mass=[2.5:0.1:4];
plot(mass,power,'LineWidth',2)
hold on
xlabel('Mass (kg)');
ylabel('Power (W)');
title(['Hovering Power Requirement: S = ', num2str(arrayA), ' m2, η =
',num2str(n)])
```

```
grid on;
legend('Power Prediction','Location','northwest')


%% Climb Power Prediction Aqua-Quad
close all
clear all
clc


%% Constants
rho = 1.225; % Air Density SL (kg/m3)
g=9.81; % gravity m/s^2


%% Dimensions
dia = 0.356 ; % rotor diameter (m)
rotors = 4; % number of rotors
rotorA = rotors*pi*0.25*dia^2; %m^2
arrayA=0.3125; %m^2


%% Aqua-Quad parameters
mass=3.5; %kg
weight=mass*g; % N


n=0.4; % Efficiency
CD=2; % Drag Coefficient


%% Predicted Power
i=1;
for vc=[1:1:10]
drag=CD*arrayA*0.5*rho*vc.^2; % N
thrust=weight+drag; % N
vh=sqrt(thrust/(2*rho*rotorA)); %mps
vi=vh*(-0.5*vc/vh+sqrt(0.25*((vc/vh)^2)+1)); %mps
climbpower(i)=(thrust.*(vc+vi))/n; %W
i=i+1;
end


%% Plot Theoretical
vc=[1:1:10];
plot(vc,climbpower,'LineWidth',2)
xlabel('Climb Speed (m/sec)');
ylabel('Power (W)');
```

```
title([‘Mass = ‘, num2str(mass), ‘ kg, CD = ‘, num2str(CD), ‘, S = ‘,
num2str(arrayA), ‘ m2, η = ‘,num2str(n)])
grid on;
hold on


%% Plot min P/vel
d=climbpower./vc; %P/V
[C,I]=min(d);
Minpowervelocity=vc(I); % velocity at (P/V)min
pmin=climbpower(I);
tangent=C*vc;
plot(vc,tangent,’:’,’LineWidth’,2)
hold on
legend(‘Predicted Power’,[‘(P/V) min @ Speed of ‘,
num2str(Minpowervelocity), ‘ m/s’],’Location’,’northwest’)

%% Descend Power Prediction Aqua-Quad
close all
clear all
clc


%% Constants
rho = 1.225; % Air Density SL (kg/m3)
g=9.81; % gravity m/s^2


%% Dimensions
dia = 0.356 ; % rotor diameter (m)
rotors = 4; % number of rotors
rotorA = rotors*pi*0.25*dia^2; %m^2
arrayA=0.3125; %m^2


%% Aqua-Quad parameters
n=0.4; % Efficiency
CD=0;


mass=0.606; %kg
weight=mass*g;
thrust=weight;
vh=sqrt(thrust/2/rho/rotorA);


i=1;
for vd=[10:0.5:20]
drag=CD*arrayA*0.5*rho*vd.^2;
```

```
thrust=weight-drag;
vh=sqrt(thrust/2/rho/rotorA);
descendpower(i)=(thrust.*(vd/2+sqrt(0.25*(vd^2)-vh^2)))/n;
i=i+1;
end


%% Plot Theoretical
vd=[10:0.5:20];
plot(vd,descendpower,'LineWidth',2)
xlabel('Descend Speed (m/sec)');
ylabel('Power (W)');
title(['Mass = ', num2str(mass), ' kg, CD = ', num2str(CD), ', S = ',
num2str(arrayA), ' m2, η = ',num2str(n)])
grid on;
hold on


%% Descent Power (VRS, V<0) Prediction Aqua-Quad
clear all
clc


% Constants
rho = 1.225; % Air Density SL (kg/m3)
g=9.81; % gravity m/s^2


% Dimensions
dia = 0.356; % rotor diameter (m)
rotors = 4; % number of rotors
rotorA = rotors*pi*0.25*dia^2; %m^2
arrayA=0.3125; %m^2


% Aqua-quad parameters
mass=1; %kg
weight=mass*g;


n=0.40; % Efficiency
CD=0; % Drag Coefficient


%% VRS Power
i=1;
for vs=[0:-1:-12];
drag=CD*arrayA*0.5*rho*vs.^2;
thrust=weight+drag;
```

```
vh=sqrt(thrust/(2*rho*rotorA));


k=1;
k1=-1.125;
k2=-1.372;
k3=-1.718;
k4=-0.655;
vi=vh*(k+k1*(vs/vh)+k2*((vs/vh)^2)+k3*((vs/vh)^3)+k4*((vs/vh)^4));


dpower(i)=(thrust.*(vs+vi))/n;


i=i+1;
end


%% Plot VRS
vs=[0:-1:-12];
plot(vs,dpower,'LineWidth',2)
xlabel('Descent Speed (m/sec)');
ylabel('Power (W)');
title(['Mass = ', num2str(mass), ' kg, CD = ', num2str(CD), ', S = ',
num2str(arrayA), ' m2, η = ',num2str(n)])
grid on;
hold on


%% Cruise Power Prediction Aqua-Quad
close all
clear all
clc


%% Constants
rho = 1.225; % Air Density SL (kg/m3)
g=9.81; % gravity m/s^2


%% Aqua-Quad Dimensions
dia = 0.356 ; % rotor diameter (m)
rotors = 4; % number of rotors
rotorA = rotors*pi*0.25*dia^2; %m^2
arrayA=0.3125; %m^2


%% Aqua-Quad Parameters
n=0.4; % Efficiency
```

```
mass=3.5;%kg
weight=mass*g;


%% Empirical Pitch Speed Parameters
p1 = -2.7872;
p2 = 3.3231;


i=1;
for vel=[0:1:10]
AOA = -(p1*vel + p2);
AOA=AOA/180*pi;
arrayL=vel^2*sin(AOA)*rho*arrayA;
thrust=(weight+arrayL)/(cos(AOA));
vi0=1;
inducedv=fzero('eqn',vi0,[],thrust,rotorA,AOA,vel);
cruisepower(i)=(thrust*(vel*sin(AOA)+inducedv))/n;
i=i+1;
end


%% Plot Theoretical
figure
vel=[0:1:10];
plot(vel,cruisepower,'LineWidth',2)
xlabel('Cruise Speed (m/sec)');
ylabel('Power (W)');
title(['Cruise, Mass = ', num2str(mass),' kg, η = ',num2str(n)])


%% Induced Velocity Forward Flight Prediction Aqua-Quad
function x=eqn(vi,thrust,area,alpharad,V)
rho=1.225; %kg/m3
nom=thrust/(2*rho*area);
denom=sqrt((V*cos(alpharad))^2+(V*sin(alpharad)+vi)^2);
x=(nom/denom)-vi;
end
```

LIST OF REFERENCES

[1] K. Jones, V. Dobrokhodov, & C. Dillard, "Aqua-Quad – solar powered, long endurance, hybrid mobile vehicle for persistent surface and underwater reconnaissance, part I – platform design," in OCEANS 2016 MTS/IEEE Monterey, Monterey, CA, USA, Sep. 2016, pp. 1–10, [Online]. doi: 10.1109/OCEANS.2016.7761030

[2] J. Vincent, "Here's Amazon's new transforming Prime Air delivery drone," The Verge, June 5, 2019. [Online]. Available: https://www.theverge.com/2019/6/5/18654044/amazon-prime-air-delivery-drone-new-design-safety-transforming-flight-video

[3] F. Lardinois, "A first look at Amazon's new delivery drone," *Techcrunch*, June 5, 2019. [Online]. Available: https://techcrunch.com/2019/06/05/a-first-look-at-amazons-new-delivery-drone/

[4] Department of Defense, "Unmanned systems integrated roadmap FY2013–2038," Washington, DC, USA, 2014. [Online]. Available: https://apps.dtic.mil/dtic/tr/fulltext/u2/a592015.pdf

[5] R. Van Noorden, "The rechargeable revolution: A better battery," *Nature News*, vol. 507, no. 7490, p. 26, March 2014. [Online]. doi: 10.1038/507026a

[6] Y. Mulgaonkar, M. Whitzer, B. Morgan, C. M. Kroninger, A. M. Harrington, & V. Kumar, "Power and weight considerations in small, agile quadrotors," June 2014, vol. 9083, p. 90831Q–90831Q–16, [Online]. doi: 10.1117/12.2051112

[7] G. Crabtree, E. Kócs, & L. Trahey, "The energy-storage frontier: Lithium-ion batteries and beyond," *MRS Bull.*, vol. 40, no. 12, pp. 1067–1078, December 2015. [Online]. doi: 10.1557/mrs.2015.259

[8] Naval Research Laboratory, "Photovoltaics," Accessed June 30, 2020. [Online]. Available: https://www.nrl.navy.mil/estd/research-highlights/photovoltaics

[9] National Renewable Energy Laboratory, "Best research-cell efficiency chart," Accessed June 30, 2020. [Online]. Available: https://www.nrel.gov/pv/cell-efficiency.html

[10] Swansea University, "Record efficiency for printed solar cells," *TechXplore*, July 8, 2020. [Online]. Available: https://techxplore.com/news/2020-07-efficiency-solar-cells.html

[11] The Economist, "Sunny uplands," November 21, 2012. [Online]. Available: https://www.economist.com/news/2012/11/21/sunny-uplands

[12] C. H. Dillard, “Energy-efficient underwater surveillance by means of hybrid aquacopters,” Master’s thesis, Monterey, California: Naval Postgraduate School, 2014.

[13] Radio Control Info, “Brushless motor efficiency and constants.” Accessed July 13, 2020. [Online]. Available: https://www.radiocontrolinfo.com/brushless-motor-efficiency/

[14] W. Johnson, *Helicopter Theory*. New York, NY, USA: Dover Publications, 1994. Knovel Aerospace Radar Technology Academic.

[15] H. Hurt, *Aerodynamics for Naval Aviators*. Rev. January 1965. Washington, D.C, USA: Office of the Chief of Naval Operations, Aviation Training Division, 1965.

[16] National Aeronautics and Space Administration, “Shape effects on drag.” Accessed June 20, 2020. [Online]. Available: https://www.grc.nasa.gov/WWW/k-12/airplane/shaped.html

[17] F. M. White, *Fluid Mechanics*, 7th ed. New York, NY, USA: McGraw Hill, 2011.

[18] S. F. Hoerner, *Aerodynamic Drag: Practical Data on Aerodynamic Drag*. Dayton, OH, USA: Otterbein Press, 1951.

[19] W. Johnson, *Rotorcraft Aeromechanics*. Cambridge, UK: Cambridge University Press, 2013. ProQuest.

[20] J. Leishman, *Principles of Helicopter Aerodynamics*. New York, NY, USA: Cambridge University Press, 2000.

[21] K. Dalamagkidis, “Autonomous vertical autorotation for unmanned helicopters,” Ph.D. dissertation, Dept. of Comp. Sci. and Eng., Univ. of South Florida, Tampa, FL, USA, 2009. [Online]. Available: https://scholarcommons.usf.edu/etd/1921

[22] J. D. Anderson, *Fundamentals of Aerodynamics*, 5th ed. New York, NY, USA: McGraw-Hill, 2011.

INITIAL DISTRIBUTION LIST

1. Defense Technical Information Center
   Ft. Belvoir, Virginia

2. Dudley Knox Library
   Naval Postgraduate School
   Monterey, California